Effect of C_{60} interfaces on the spin transport in heavy metal thin films grown on YIG

Satam Alotibi

School of Physics and Astronomy

University of Leeds

Submitted in accordance with the requirements for the degree of
Doctor of Philosophy

August 2021

This thesis is dedicated to my parents,...

Intellectual Property Statement

The candidate confirms that the work submitted is his own, except where work which has formed part of jointly authored publications has been included. The contribution of the candidate and the other authors to this work has been explicitly indicated below. The candidate confirms that appropriate credit has been given within the thesis where reference has been made to the work of others.

This copy has been supplied on the understanding that it is copyright material and that no quotation from the thesis may be published without proper acknowledgement.

The right of Satam Alotib to be identified as Author of this work has been asserted by him in accordance with the Copyright, Designs and Patents Act 1988.

In all cases, Dr. Oscar Cespedes provided guidance for experiments and data analysis. Design and optimisation of C_{60} is done by Dr. M.C. Wheeler and Dr. Oscar Cespedes.

The following publication is used in this work:

Enhanced Spin Orbit Coupling in Heavy Metals via Molecular Coupling.

Satam Alotibi, Bryan J. Hickey, Gilberto Teobaldi, Mannan Ali, Joseph Barker, Emiliano Poli, David D. ORegan, Quentin Ramasse, Gavin Burnell, James Patchett, Chiara Ciccarelli, Mohammed Alyami, Timothy Moorsom, and Oscar Cespedes. ACS Applied Materials Interfaces, vol. 13, no. 4, pp. 5228-5234, 2021.

Acknowledgements

My sincere thanks goes to my supervisor Dr. Oscar Cespedes, for his invaluable insights, recommendations, and meticulous attention to detail. This study would not have been feasible without his extensive understanding and direction into experimental physics. His outstanding scientific abilities, tremendous humanity, and leadership aided me throughout the study procedure. I just do not have the words to express my heartfelt gratitude and respect.

I would want to express my gratitude to Prof. Bryan Hickey, my co-supervisor, for all of his wise words and support. Prof. Chris Marrows, Dr. Joseph Barker, Dr. Thomas Moore, Dr. Satoshi Sasaki, Dr. Gavin Burnell, and Dr. Mannan Ali, as well as the rest of the academic staff, who supported and encouraged me throughout many constructive talks, deserve particular appreciation. Dr. Gavin Burnell has been really helpful in my work, from assisting me in learning Python and Lab-View to providing ongoing assistance with discussion of my work. Dr. Mannan Ali deserves special mention for all of his assistance in the lab throughout the early stages of my PhD.

During the early years of my PhD, I was fortunate to gain from Dr. Matthew Rogers' scientific expertise, Dr. George Stefanou, Dr. Mohammed Alyami, Dr. Shoug Alghamdi, Dr. Tim Moorsom, Dr. Benjamin Steele and Dr. Amy Westerman. I would also like to thank Dr. Kathryn Moran, Dr. Matthew Vaughan, Nader Alosaimi, Jack Adams, Khulaif Alshammari, Alistair Walton and Joshua Gretton for their help and cooperation during my PhD.

I am also grateful to the members of the cryogenic crew, both past and present, for constantly keeping things cold. Everyone in the mechanical workshop has aided me at some point, and they have always done it cheerfully. Thank you also to the electronics workshop, which has been really helpful in my job and in resolving issues. It has been a joy to work with numerous wonderful colleagues and undergraduates in the CM group, who create a fascinating and pleasant environment.

Abstract

This research consideres the effect of molecular overlayers on the spin Hall magnetoresistance (SHMR) and anisotropic magnetoresistance (AMR) of heavy metals (Pt, Ta, and PtMn). The objective is to investigate the effect of molecular overlayers on the effective spin orbit coupling (SOC), i.e. the charge-spin conversion of heavy metals. We have pursued this objective by measuring the SHMR & the AMR in YIG/Metal and YIG/Metal/C_{60} structures. This effect has generated a large interest over the last few years, and they are critical in the study of the spin Hall angle and its applications, e.g. for devices such as spin torque MRAM.

"In this study" when C_{60} is grown on a metal, the electronic structure is altered due to hybridisation and charge transfer. A conducting layer with high SOC is formed at the interface between a heavy metal and molecules. The SHMR for Pt/C_{60} and Ta/C_{60} at room temperature are up to a factor 6 higher than for the pristine metals, with the spin Hall angle increased by 20-60 %. At low fields of 1-30 mT, there is an AMR which increases up to 700 % at room temperature by C_{60}. Given the dielectric properties of C_{60}, this opens the possibility of gating the effective SOC of metals, with applications for spin transfer torque memories and pure spin current dynamic circuits.

Annealing sample plays a crucial part in our transport properties of (Pt, PtMn) and (Pt, PtMn)/C_{60} because of changes to the crystallinity and metallo-molecular coupling at the interface. As a result, the SHMR/MR can increase by a further factor 4 when annealing at a temperature of 300 °C.

Symbol

G Spin Mixing Conductance

λ Spin Diffusion Length

M Magnetisation

D Diffusion Constant

d Thickness

θ_{sh} Spin Hall Angle

ρ Resistivity

σ Conductivity

T Temperature

J_s Spin Current

J_e Charge Current

τ_{sf} Spin Relaxation Time

τ_p Momentum Relaxation Time

Abbreviations

MR	magnetoresistance
AMR	anisotropic magnetoresistance
$SHMR$	spin hall magnetoresistance
NM	Normal Metal
DC	direct current
GGG	gadolinium gallium garnet
YIG	yttrium iron garnet
YAG	Yttrium Aluminium Garnet
Pt	platinum
SHE	spin Hall effect
$ISHE$	inverse spin Hall effect
RF	radio frequency
VTI	variable temperature insert
SOC	spin-orbit coupling
OSC	Organic semiconductors
DC	Direct Current
FM	Ferromagnet
FMR	Ferromagnetic Resonance
XRD	X-ray Diffraction
XRR	X-ray reflectivity
TEM	Transmission Electron Microscopy
SEM	Scanning Electron Microscope

Contents

List of Figures

CHAPTER 1

Introduction

1.1 Spintronics

Spintronics is one of the most active research areas of solid-state physics. It is based on the notion of the combination between the spin and charge of electrons [1]. This incorporates both the spin and charge of electrons in magneto-electronic devices such as spin valves or magnetic tunnel junctions. The main aim of spintronics is to develop a technology to increase speed and reduce power consumption over current electronics and computing hardware [2]. In 1985, spin polarised electrons were observed to be injected into a normal metal when a charge current passes through a magnetic material [3]. The electrons become spin polarised in the magnetic material, then the spin polarised current moves into a normal metal (NM) and relaxes over a characteristic spin diffusion length. As we can control the magnetisation of magnetic materials with an external field, we can control the direction of the spin current. By the spin Hall magnetoresistance (SHMR) [4], it is possible to study spin-related charge transport phenomena. The SHMR can quantify the spin orbital coupling in thin ($\sim$nm) heavy metal layers deposited on a magnetic insulator such as the yttrium iron garnet $Y_3Fe_5O_{12}$ (YIG) [4; 5; 6]. Spin-orbit coupling has attracted attention in the last years due to its connection to spin-orbit torque and its applications in MRAM, energy generation and low-dissipation devices [7; 8].

The spin-orbit coupling (SOC) is perhaps the most crucial mechanism in the design of magnetic structures and metal device physics. This interaction occurs when the electron of the atom moves in the electric field (caused by nucles with crystalline anisotropy) and the spin of the electron combine with the effective magnetic field. It determines the magnetocrystalline anisotropy, is key to the propagation and electrical conversion of spin currents, determines the magnitude of interfacial mechanisms such as the Dzyaloshinskii Moriya interaction and guides new paths of research, such as the generation of Majorana fermions and energy band engineering of topological insulators [9; 10; 11; 12; 13]. The major source of magnetocrystalline anisotropy is the SOC. The first order contribution to magnetocrystalline anisotropy is essentially the orbital motion of electrons,

which interacts with the crystal electric field [14]. The SOC also controls the efficiency of spin - charge conversion in the spin Hall, spin torque and spin Seebeck effects [15; 16; 17]. All of these are key to reducing the power consumption and energy dissipation of computing and electronic devices, an issue that is quickly coming to the forefront of technology. However, currently we can only tune the SOC by static means, such as doping, preventing the design of architectures where spin, charge and magnetic interactions can be reversibly modified to enhance device performance or to acquire new functionalities [18]. However, there are previously reports that point to the possibility of gating the interfacial Rashba SOC [19].

The efficient generation of pure spin currents has huge attention for the applications in emerging spintronic devices. A measure of the conversion efficiency between charge currents and pure spin currents is given by the spin Hall angle (Θ_{SH}) of the material [20; 21; 22]. The ratio of the spin-to-charge current is known as the spin Hall angle. The Θ_{SH} is important in devices such as spin-transfer torque (STT) memories, as it is correlated with the torque exerted on ferromagnets (FM) [23]. A larger SHMR, and therefore increased Θ_{SH}, can result in lower power or smaller switching currents for such devices. By tuning the SOC in conventional magnetic insulator/metal structures with a molecular layer, we can also differentiate spin transport effects based on their physical origins [24; 25].

Organic spintronics is considered as the application of spin polarised electron injection, transport and detection in devices using organic materials [26]. Organic spintronics has made huge progress over the past few years. The low atomic mass of organics leads to weak SOC and therefore long spin lifetimes although the low mobility may reduce the spin diffusion length ($\sim$ 100 nm in C_{60}) [27]. The interfacial properties between ferromagnetic electrodes and organic spintronics have further increased the application, which has caused great interest in the field of organic spintronics over recent years [28; 29; 30]. The addition of organics to the field of spintronics leads to the consideration of how spin-hybridised states can influence spin transport. When a molecule is in contact with a metallic substrate, there is a change in the electronic properties of both materials due to orbital

hybridisation and charge transfer. In the case of C_{60} with transition metals, this leads to the formation of an additional conducting layer at the interface. This interfacial change may lead to changes in the SOC of the metal. Previously, it has been shown that this can lead to the emergence of spin ordering in interfaces with thin layers of a C_{60}/ thin transition metal interface [4]. The interfacial effect is also critical in spin filtering and spin transport effects [2]

The generation and propagation of spin currents can be detected at FM/NM interfaces. One of the methods to generate a spin current is by using ferromagnetic resonance, where the electrons spin in a ferromagnet precess around an applied magnetic field [31; 32; 33]. Thus, the spin current then can travel into an adjacent NM from the magnetization precession, this process is called spin pumping [34]. Another method to generate a spin current is based on spin Hall effect (SHE). Section 2.3 will explain the SHE in more details. In this method, the spin current is observed in materials due to the spin orbit coupling [35; 36]. Also, thermal effects can be contributed in producing the spin currents via temperature gradients. The spin current is especially strong in metals with a high atomic number such as platinum.

1.2 Thesis layout

In Chapter 2, the background physics relevant to this work are discussed to understand the experimental work and the results presented. Firstly, a general introduction into the crystal structure of YIG and platinum is given. We present theories of spin transport and magneto-transport phenomena that describe the SHMR and AMR. Furthermore, some concepts of the organic spintronic with a review of the relevant literature are introduced. A discussion of the spin-dependent interfacial hybridisation at metal/C_{60} interfaces are considered, with the future research path of tuning the properties of the molecular layer via optoelectronic irradiation.

Key experimental techniques used for sample preparation, structural and magnetic characterisation are described in Chapter 3. Starting with the deposition of YIG samples by RF magnetron sputtering and DC magnetron sputtering for

metals. Then growth of C_{60} by in situ UHV thermal molecular sublimation. X-ray reflectivity has been used to characterise the sample structure and determine the thickness of thin films. The magnetic properties are studied using a superconducting quantum interference device (SQUID) vibrating sample magnetometre (SQUID-VSM). Low temperature transport measurements have been used to study the spin transport properties of metals and hybrid metallo-molecular structures over a wide range of temperatures and magnetic fields. The setup is used for electrical characterization of the devices with a definition of the measurement geometry.

Chapter 4 presents a MR investigation of Pt and Pt/C60 over a range of Pt thicknesses (1.5-25 nm) and temperatures (5-290 K). Extracting the spin Hall angle by fitting the SHMR data. Study the impact of YIG/Pt substrate for gadolinium gallium garnet (GGG) and yttrium aluminium garnet (YAG). At low fields of 1-30 mT, there is an anisotropic magnetoresistance, enhanced for all temperatures and Pt thicknesses by C_{60}. In this chapter, we investigate transport properties of Pt and Pt/C_{60} after annealing at 200-300 °C.

Chapter 5 introduces the transport measurements of Ta and Ta/C_{60} over a range of Ta thicknesses and temperatures. For Ta, the resistivity with C_{60} is higher than without. This layer contributes to the transport, but in exchange the rest of the Ta has a lower conductivity due to changes in the electronic structure and increased polycrystalline seen by the electrons. The SHMR measurements in this chapter were performed at a field of 0.5 T (pure SHMR), so the YIG can be saturated out of plane but other field dependent. As it was the case for Pt, a low field AMR exists in Ta, which is increased by C_{60} at all temperatures and sample thicknesses.

In chapter 6, the findings of SHMR and AMR measurements of PtMn wires on YIG before and after annealing demonstrate that molecular overlayers can improve the spin orbit coupling of PtMn. The resistivity for PtMn with C_{60} is lower than for bare PtMn wires due to charge transfer and orbital re-hybridisation, contributing to the conductivity. TEM measurement are used to characterise the

interfaces further and offer information on inter-diffusion before and after annealing. As we describe the influence of annealing on sample interface characteristics, the annealing process plays a significant role in our investigations.

In Chapter 7 all the results from experiments and their interpretation are summarised. Following that, a prognosis for future work is provided based on the findings.

CHAPTER 2

Literature review

2.1   Introduction to the structure and properties of YIG

Yttrium iron garnet (YIG) is composed of yttrium, iron and oxygen. The chemical composition is as follows:

$$[Y_3^{3+}](Fe_2^{3+})[Fe_3^{3+}]O_{12}^{2-}. \tag{2.1}$$

Where Fe occupies both tetragonal and octahedral sites and Y is in the dodecahedral sites as in figure 2.1. The ferrimagnetic properties of YIG arise from the interaction between Fe^{3+} ions occupying tetrahedral and octahedral sites via the oxygen ions surrounding them. The mechanism for this interaction is via superexchange [37]. The superexchange is antiferromagnetic coupling via the oxygen atoms with 2 magnetic lattices of different moment and opposite magnetisation direction. YIG is an insulator material with a large band gap (2.85 eV), high melting point (1555 °C), high thermal and chemical stability, low thermal expansion and high thermal conductivity [38]. Low ferromagnetic resonance damping (3×10^{-5}) is one of the attractive properties of YIG, allowing spin transport over long distances [39]. Also, YIG has been a very important material to industry for decades due to its microwave properties [40].

Sample growth is an important factor in the production of high quality YIG. The two most common methods to prepare YIG are pulsed laser deposition (PLD) and radio frequency (RF) magnetron sputtering. Since RF magnetron sputtering is the cheapest method of YIG preparation [41; 42], and it allows for thinner films in-situ deposition, this method has been used in this project, sample growth experimental details are explained in section 3.2.

Hybrid structures of YIG and strong spin-orbit coupling metals exhibit a variety of interesting spin current related phenomena such as SHMR [4; 43; 44; 45], the spin Seebeck effect (SSE) [15; 16; 17], spin pumping [31; 32; 33], and recently in photo-induced-spin voltaic effect [46]. Because no electrical conduction occurs in YIG, a magnetoresistance can be measured unequivocally in the thin metal

layer; therefore, a charge current can only flow in the metal layer; this will be explained further in section 2.4.
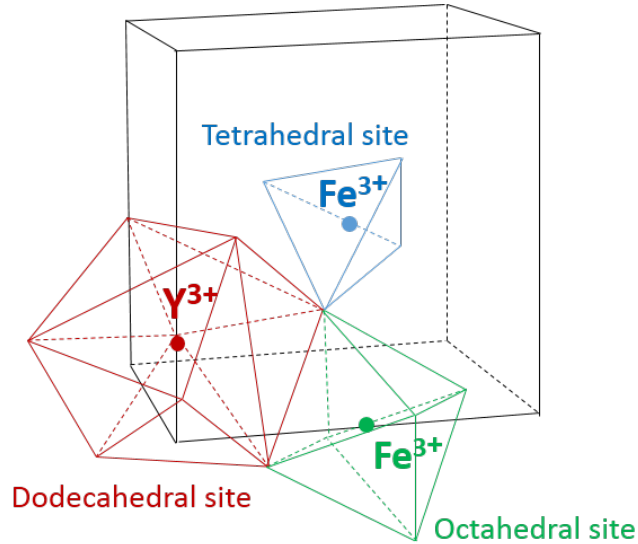
Figure 2.1: The unit cell of YIG has cubic structure. The magnetisation in YIG produces from the superexchange interactions between 16 Fe^{3+} ions on the octahedral and 24 Fe^{3+} ions on tetrahedral sites. Taken from [47]

2.2 C$_{60}$ fullerene

In 1985 Harold Kroto, Robert Curl and Richard Smalley discovered the C$_{60}$ fullerene for which they were awarded the Nobel Prize in 1996 [48; 49]. The resemblance of the molecule to the famous geodesic domes gives it a second name, buckminsterfullerenes or buckyballs from the name of the designer Buckminster Fuller [50]. The C$_{60}$ molecule consists of 60 carbon atoms arranged in 20 hexagons and 12 pentagons as shown in Figure 2.2. Every atom of carbon has six electrons with the configuration $1s^2$, $2s^2$ and $2p^2$, with two electrons in the first shell and four electrons in the 2nd shell [51]. Due to a slight difference in energies between s and p orbitals, hybridisation occurs in the carbon atoms. This forms two types of covalent bonds in the molecule: π bonds and σ bonds [52; 53]. π

bonds form when orbitals overlap side-by-side. σ bonds form when orbitals overlap end-to-end. Figure 2.3 shows how these bonding states form and the different hybridisations of orbitals in carbon.
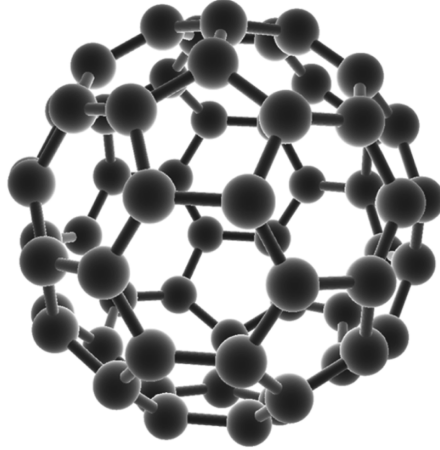
Figure 2.2: The C$_{60}$ molecule consists of 60 carbon atoms arranged in 20 hexagons and 12 pentagons. Taken from [54].

C$_{60}$ is attractive for use in spintronics for the reasons that follow. Firstly, C$_{60}$ acts as an n-type semiconductor, which is useful for thin film devices [55]. Secondly, compared to other organic materials, C$_{60}$ allows readily for spin injection because the Fermi levels of common ferromagnetic materials are well matched with the lowest unoccupied molecular orbital (LUMO) of C$_{60}$ [56; 57]. As a result of this, a significant magnetoresistance has been observed at both low and high temperatures when C$_{60}$ is used as a spacer layer in spin valve devices [27; 58; 59; 60; 61]. Thirdly, organic semiconductors have low atomic mass number (Z), and spin orbit coupling is proportional to Z^4. Therefore, C$_{60}$ has low spin orbit coupling, which enable electrones to be transported with long spin lifetime [27]. The SOC is not only dependent on the atomic number, but also on the curvature of the molecule. That is why, for example, C$_{60}$ is a more efficient spin-voltage converter (inverse spin Hall effect, proportional to the SOC) than some molecules with Pt ions [52]. Also, C$_{60}$ does not have hydrogen and it possesses a weak hyperfine interaction because of the lack of spin in the nuclei of C^{12} [27].
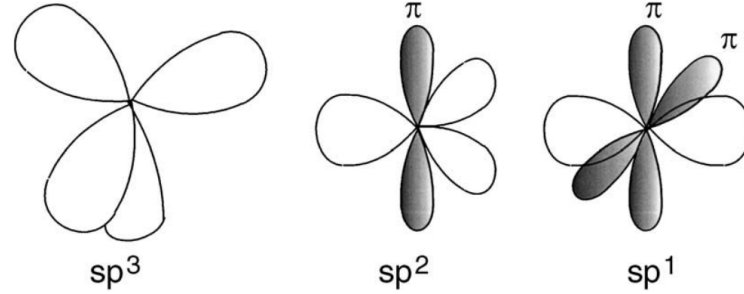
Figure 2.3: The weak π bonds and strong σ bonds are represented by shaded and unshaded regions respectively. Taken from [51].

2.3 Spin Hall effect

The ordinary Hall effect is the accummulation of charge (electrons and/or holes) perpendicular to an applied magnetic and electric field and resulting in a Hall voltage across an electrical conductor. This effect is due to the Lorentz force acting on the charge carriers. Analogous to the ordinary Hall effect, where opposite charges accumulate on opposite sides of the metal, the spin Hall effect results in accumulation of opposite spin on either side [36]. The spin Hall effect (SHE) was first theorised in 1971 by Dyakonov and Perel [62; 63]. This theoretical work had no significant progress until 1999, when Hirsch [36] and Zhang [64] proposed an experimental setup.

The charge current density J_e can be split into the contributions of spin up electrons $J_\uparrow$ and spin down electrons $J_\downarrow$ [65] with the total charge current density is the sum of both

$$J_e = J_\uparrow + J_\downarrow = -\frac{\sigma}{e}(\nabla\mu_\uparrow + \nabla\mu_\downarrow) \tag{2.2}$$

The charge currents are generated by the spin dependent electrochemical potential $\mu_{\uparrow(\downarrow)}$. The elementary charge is $e = |e|$ and σ denotes the charge conductivity. In a normal metal, the conductivity σ is identical for both spin orientations. There is an angular momentum due to the spin of the electron. However, no net

angular momentum is transported with the current when the same quantity of spin up and spin down electrons flow in the same direction. The total angular momentum transported is the difference between spin up and spin down currents.

$$J_s = -\frac{\hbar}{2e}(J_\uparrow - J_\downarrow) \tag{2.3}$$

where J_s is the spin current, $-J_\downarrow$ corresponds to negative angular momentum transport and $-J_\uparrow$ is associated with positive angular momentum flow. Thus, a pure spin current arises when $J_\downarrow = -J_\uparrow$. As consequence of an imbalance in the spin accumulation $\mu_s = \mu_\uparrow - \mu_\downarrow$, the spin current can be written as:

$$J_s = -\frac{\hbar\sigma}{2e^2}\nabla\mu_s \tag{2.4}$$

As in equation 2.5, a spin current is generated by a charge current via the spin Hall effect and a charge current is generated by spin current via inverse spin Hall effect where **s** is the spin polarisation vector and Θ_{SH} is the spin Hall angle:

$$\Theta_{SH} = |\ J_s\ |\ /\ |\ J_c\ | \qquad J_s = \Theta_{SH}(-\frac{\hbar}{2e})\mathbf{J_c} \times \mathbf{s} \tag{2.5}$$

The mechanisms by which the spin accumulation occurs is the same as that which gives rise to the spin Hall effect. These mechanisms can be classified as intrinsic or extrinsic, which are distinguishable based on whether the spin relaxation occurs in between or during scattering [66]. The extrinsic contributions originate from spin-dependent scattering with impurities. Intrinsic contributions are inherent to the band structure of the pure crystal. There exist two varieties of extrinsic contributions subdivided into skew scattering [67] and side-jump scattering [68].
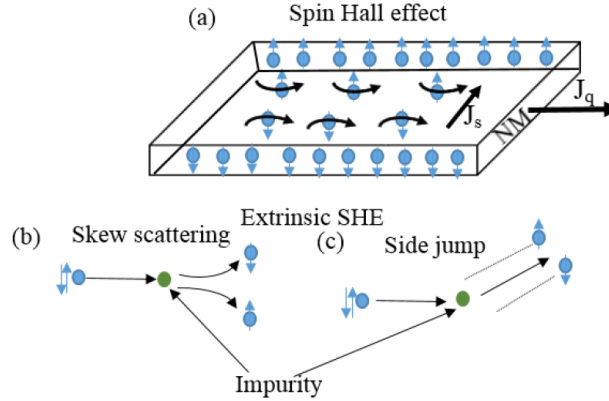
Figure 2.4: The geometry of the spin Hall effect in (a) shows the charge current J_c in the plane scattering with spins in different direction. The extrinsic skew scattering is in (b). (c) Extrinsic side jump scattering from an impurity. Taken from [69].

Skew scattering was first proposed in the 1950s by Smit [70]. This mechanism comes from spin orbit coupling within the disorder scattering potential. That performs in different scattering cross sections as spin up and spin down electrons. (see figure 2.4). In this case, approaching the electron from the impurity induces an effective magnetic field due to the spin-orbit coupling which generates a net force acting away from the scattering depending on spin direction. The magnitude of the skew scattering contribution depends upon the difference in spin-orbit coupling between the impurity and host.

Scattering with side-jump occurs as a result of the difference in the spin-dependent mobility during the scattering process. Thus, the displacement is the same for spin up and spin down electrons, but in opposite directions. A spin current is generated perpendicular to the initially unpolarised charge current . The expression for the side-jump scattering contribution to the spin Hall conductivity is given by [71].

$$\sigma_{sj}^{SH} = -2\frac{e^2}{\hbar}n\lambda_c^2 \qquad (2.6)$$

Where n is the electron density and λ_c^2 is a coupling constant of the conduction band. In the side jump mechanism, the spin-Hall angle is proportional to the impurity concentration, [72] unlike the skew scattering mechanism. The total spin Hall conductivity for the material is given by

$$\sigma_{xy}^H = \sigma_{xy}^{int} + \sigma_{xy}^{SS} + \sigma_{xy}^{SJ} \tag{2.7}$$

where σ_{xy}^{int}, σ_{xy}^{SS} and σ_{xy}^{SJ} are the sum of intrinsic, skew scattering and the side jump contributions respectively.

The measure of spin Hall effect is given by the spin Hall angle, which is shown as the ratio of the measured spin current injected into the NM material and charge current deflected by ISHE in the NM material. The spin Hall angle is strongly correlated to the spin diffusion length (λ), which quantifies the decay of the pure spin current along with its diffusion. Moreover, the spin Hall angle is a material-dependent parameter, and elements with high atomic number such as Pt, W, Pd and Ta, have been regularly used for spin-charge interconversion because they have strong SOC, resulting in large Θ_{SH} [73; 74; 75; 76]. Typical values for Pt spin Hall angle are between 0.02 and 0.13 [6; 76; 77; 78; 79; 80], where the variation between results is largely regarded to be due to the difference in interfacial spin-mixing conductivities [81]. For Ta, the spin Hall angle is negative with typical values in the range between -0.02 and -0.15 [74; 76; 78; 82].

2.4 Spin Hall magnetoresistance

The SHMR is observed when a current is passed through a heavy metal thin film deposited on a ferrimagnetic insulator [4]. Yttrium iron garnet is commonly used as ferrimagnetic insulator and platinum as the normal metal thin layer. When a charge current ($\mathbf{J_e}$) is applied through a Pt wire parallel to the YIG/Pt interface, a spin current ($\mathbf{J_s}$) is genereated due to the spin Hall effect. The spin current will diffuse transverse to the charge current and perpendicular to the YIG/Pt interface. Thus, the spin current polarisation ($\mathbf{s}$), $\mathbf{J_s}$ and $\mathbf{J_e}$ are orthogonal with each other, which results in a spin polarisation parallel to the interface. The

direction of the YIG magnetisation controls the conversion rate of the angular momentum of the spin current reflected, as the spin current can be transferred to the YIG film as spin waves [83]. When the direction of the magnetisation **M** in the YIG layer and the spin polarisation **s** are parallel, the spin current is reflected from the interface and back into the metal. Therefore, the inverse spin Hall effect deflects the electrons and this results in a momentum change of the electrons in the current direction, reducing the resistivity of the NM. However, if the direction of the magnetisation **M** and spin polarisation **s** are perpendicular, the spin current is able to pass into the YIG and continue as spin wave. Figure 2.5 is a pictorial representation of those processes.

The SHMR effect is simply due to the combined action of both the spin Hall effect and inverse spin Hall effect. The SHE controls the spin current which is proportional to the charge current. This results in spin accumulation at opposing surfaces which is perpendicular to the flow of the electric charge as shown in figure 2.5 (*b*). The ISHE is the conversion of an injected spin current into a transverse electric current. Thus, this charge current that generated by ISHE contributes to the total resistance of the electrode which depends on the magnetic field. The mechanisms that govern both the spin Hall effect and its inverse is based on the spin orbit coupling.

The angular dependence of the SHMR is given by equation 2.8:

$$\rho = \rho_0 - \Delta\rho \ sin^2\varphi \qquad (2.8)$$

where φ is the angle between the magnetisation vector of the FM and the spin polarisation of electrons in the NM. The cross product of the spin accumulation and spin mixing conductance at the NM interface derives the spin current density. A sin^2 dependency is predicted since both of these variables are connected to the angle of the applied field. The size of the resistivity difference has been calculated based on theory where the magnitude of the SHMR is given by the following equation [5]:

$$\frac{\Delta\rho}{\rho_0} = \Theta_{sh}^2 \frac{\lambda}{d} \frac{2\lambda G \ tanh^2\frac{d}{2\lambda}}{\sigma + 2\lambda G \ coth\frac{d}{\lambda}} \tag{2.9}$$

Equation 2.9 gives the size of the resistivity difference ($\Delta\rho$) between two magnetisation orientations, and ρ_0 is the resistivity of the film. The spin diffusion length is λ, d is the thickness of the film, σ is the conductivity of the metal, and G is the spin mixing conductance. For NM thicknesses above λ, the ISHE effect has a smaller contribution to the resistivity. For thicknesses below λ, the spin accumulation at the interfaces are mixed due to their proximity. G is dependent on the quality of the interface between the metal and the insulator. The only parameter not determined by the experiment (conductivity, temperature), nor set as a fitting parameter (spin Hall angle, spin diffusion length) is the spin-mixing conductance, which we have used the value derived in Althammers review paper of $4 \times 10^{14}\Omega^{-1}m^{-2}$ [6].

We use this equation 2.9 only as a means to have a qualitative idea of variations in the different parameters contributing to the SHMR, although only those values that are experimentally determined can be used to compare pure metal and metal-molecular layers: resistivity, magnetoresistance (anisotropic and spin Hall), and magnetization. We treat Pt/C_{60} as a single layer, but we do not know how thick the C_{60} layer contributing to the resistivity is. Simulations seems to indicate that only the first molecular layer in contact with the metal is conducting ($\sim$1 nm), but we cannot confirm this experimentally. There are no equivalent models for two conducting layers.

Many recent studies have focused on the SHMR and related MR effects in nonmagnetic layers with strong spin-orbit coupling, such as Pt, W and Ta grown on YIG or other ferri/ferromagnetic substrates [84; 85; 86]. The general conclusion is that the interfacial magnetism in YIG/metal bilayers plays a role in their magnetotransport [45; 87; 88]. The SHMR ratio is proportional to the spin-mixing conductance of the YIG/metal interface and the square of Θ_{sh} [89] . Thus, increasing the number of interfaces may increase the total SHMR ratios. This makes the study of multilayer structures an essential topic of research for work

in SHMR [90]. The effect of multilayer can be proved where the YIG/Pt/C$_{60}$ SHMR effect is higher than YIG/Pt layers, as shown in the results chapters.
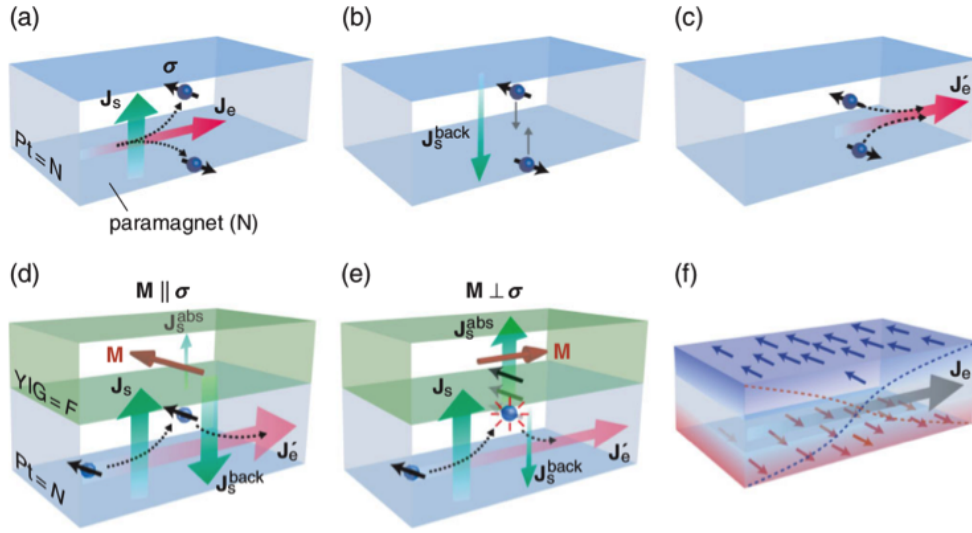
Figure 2.5: The mechanisms at the origin of the SHMR. Taken from [4].(*a*) shows the SHE is generating a spin current $\mathbf{J_s}$ which is perpendicular to the charge current $\mathbf{J_e}$. (*b*) Here, the spin current is reflected from the surfaces of the thin metal film. (*c*) Shows how the ISHE is producing the charge current. (*d*) Shows the magnetisation $\mathbf{M}$ and spin polarisation σ parallel and how the spin current is reflected from the interface and back into the metal. (*e*) Here, the magnetisation $\mathbf{M}$ and spin polarisation σ are perpendicular and the spin current is able to pass into the YIG. (*f*) Shows the spin current producing a spin polarised charge current in the Pt.

Temperature dependence of SHMR

Usually, thin film properties are dependent on the deposition technique employed. For example, MR measurements are very sensitive to sample texture. The temperature dependence of the SHMR reproduces observations in radio frequency-sputtered YIG/sputtered Pt wires [91]. For Pt grown by evaporation on thicker YIG layers grown by liquid phase epitaxy or pulsed laser deposition, the SHMR has a gentler drop at high temperatures [92]. Figure 2.6 (a) shows the SHMR measured for a Pt layer deposited via electron beam evaporation on top of a YIG film. The gentler drop is attributed to a smaller temperature dependence of the spin diffusion length [92], which could be due to a different resistivity of Pt and different magnetic behaviour of YIG films depending on the growth method. Our Pt wires are deposited by sputtering, similar to other groups working on sputtered Pt wires [44; 91; 93]. Figure 2.6 (b) shows a peak in the SHMR at 100-150 K, which has been identified as corresponding to the temperature when the spin diffusion length of Pt equals the Pt thickness. The relevance of spin-flip phonon scattering is likely to play a key role on the shape of the SHMR [94]. We hypothesize that the relevance of spin-flip phonon scattering vs. other scattering mechanisms depends on the growth method used, the number of grain boundaries. The behaviour of the spin diffusion length as a function of temperature may be predicted since the resistivity of a material is based on the momentum scattering time. For a NM, the spin diffusion length has an inverse relationship with temperature [95].
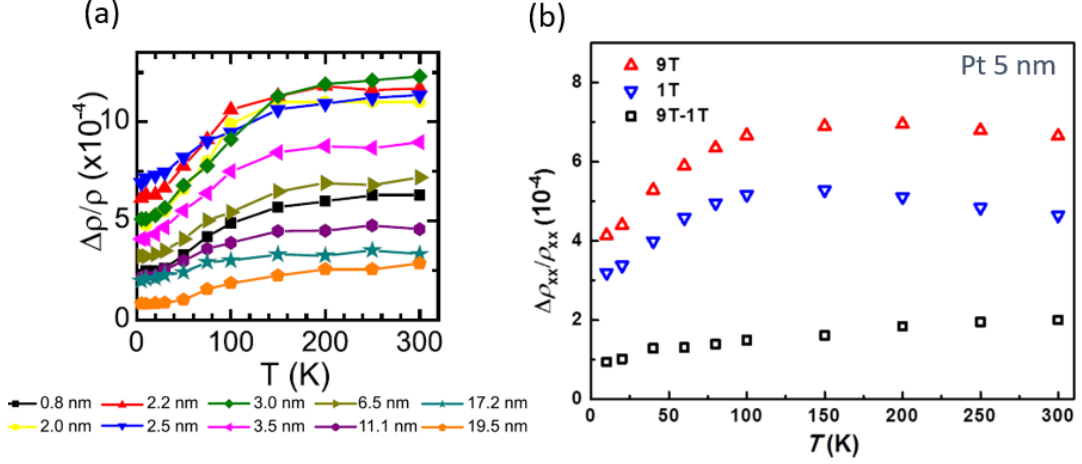
Figure 2.6: The temperature dependence of the SHMR between 5 K and room temperature measured in YIG/Pt. (a) Temperature trend for various Pt thicknesses deposited by electron beam evaporation. Taken from [92]. (b) Temperature trend for Pt 5 nm deposited by sputtering like our Pt wires. Taken from [93].

2.5 Anisotropic magnetoresistance (AMR)

The AMR is useful for investigating spin-dependent electron transport properties and magnetization processes [96; 97]. It is based on the spin orbit coupling and the dependence of the resistivity of the relative alignment of the current and the magnetic moments. The spin orbit coupling causes mixing between the spin up and spin down bands in samples with conductive s-bands and spin split ferromagnetic d-bands that are spin imbalanced at the Fermi energy. Thus, the anisotropic spin-mixing leads to anisotropic scattering [98]. Depending on the magnetisation direction when a large external field is applied to the sample, the electron around the nucleus is slightly deformed. The orbits in the plane of the current leads to small scattering, when the magnetisation is perpendicular to the current direction, resulting a lower resistivity. On the contrary, when the magnetisation is parallel to the current, the electron orbits perpendicular to the current leads to larger scattering, resulting a high resistivity. The angular dependence of the AMR is described by:

$$\rho(\varphi) = \rho_\perp + (\rho_\parallel - \rho_\perp)cos^2\varphi \qquad (2.10)$$

Where $\rho_\parallel$ is defined as the resistivity when the magnetisation and the current are parallel and $\rho_\perp$ when they are perpendicular [97]. The orientation of the magnetisation relative to the current direction provides a method to distinguish between AMR and SHMR [2]. The SHMR and AMR have an angular dependence of the resistivity on direction of magnetisation which can be easily checked by performing out-of-plane magnetisation measurements. The SHMR is measured at the angle between the spin polarisation and the applied H field, while the AMR is measured at the angle between the charge current and the field (more details in section 3.5.4). In this case, the behaviour of the SHMR and AMR is different. However, there was an ongoing debate concerning whether the magnetoresistance in YIG/Pt is in fact a consequence of an interfacial AMR within a proximity polarised Pt layer [99]. This generated a lot of discussion about the true origin of the AMR. The existence of a magnetic proximity effect in Pt/YIG is controversial, with studies both for and against [24; 25]. The magnetic state of heavy metal Pt will be discussed next section.

2.6   Magnetism in platinum

Platinum is paramagnetic, with atoms that have electrons in unfilled 5d shells. The unpaired electrons have magnetic moments that align in the direction of an applied external filed [98]. Pauli paramagnetism occurs when a magnetic field is applied to a metal because the Zeeman energy lifts the degeneracy of the spin up and spin down bands, moving them by $\pm\mu_B\mu_0H$. The number of electrons have moved from spin up to spin down states is $n_\uparrow = g(E_F)\mu_B\mu_0H$, and $g(E_F)$ is the density of states at the Fermi energy. Thus, a magnetisation can given by:

$$M = \mu_B(n_\uparrow - n_\downarrow) = 2\mu_B^2 g(E_F)\mu_0H \qquad (2.11)$$

The Pauli susceptibility (χ_P) is dependent on the density of states at E_F, as seen in Equation 2.12. Thus, material with large $g(E_F)$ can be referred to as Stoner enhanced paramagnets.

$$\chi_P = \frac{M}{H} = 2\mu_{\mathrm{B}}^2 g\left(E_{\mathrm{F}}\right)\mu_0 \tag{2.12}$$

Paramagnetic materials with large densities of states at the Fermi level have a large enough Stoner product to cause a significant enhancement of the magnetic susceptibility, as shown in figure 2.7. However, the enhanced magnetic susceptibility for Pt is unable to cause spontaneous ferromagnetism. It has been reported that Pt can interact with other ferromagnetic materials to enhance its magnetism [69]. In 1954, the magnetisation of Pt was shown to have a temperature dependence with a peak at 90 K [100]. Recently, it has been claimed that Pt shows ferromagnetic state when in contact with a ferrimagnetic material like YIG [24; 101; 102].
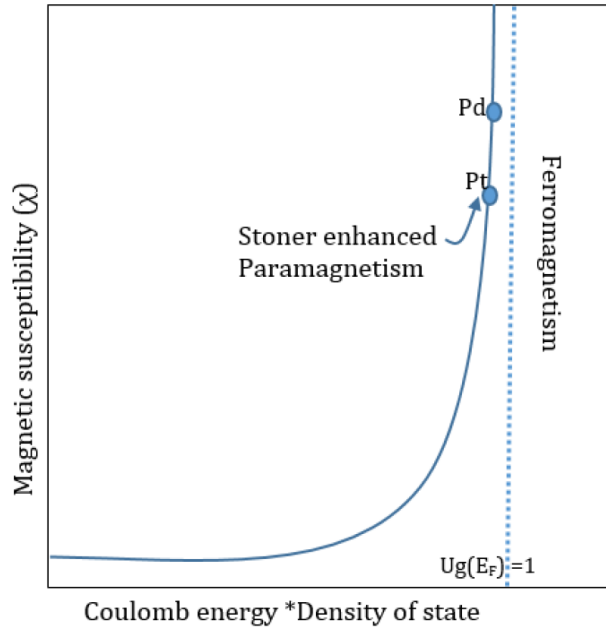
Figure 2.7: Magnetic susceptibility against the density of states (DOS) near the Fermi energy g(E_F). This effect is termed as Stoner enhanced paramagnetism. Taken from [69].

Although Pt is not ferromagnetic, it shows AMR when in contact with a magnetic insulator. This has been explained in [103; 104] as due to a magnetic proximity effect. This study is based on the fact that Pt nearly satisfies the Stoner criterion for ferromagnetism. The magnetic proximity effects or a spontaneous polarisation of paramagnetic occur due to the hybridisation of atomic orbitals at the interface. The boundary effects in thin film are significant, thereby leading to an magnetic interaction between nearest neighbouring atoms at the interface. In a YIG/Pt interface, X-ray magnetic circular dichroism (XMCD) provides an average Pt moment of 0.054 μ_B at 300 K [24]. However, this is very close to the resolution limit of the instrument, and it has been claimed that there is no evidence for this induced magnetization [25; 45]. In this case, the XMCD signal shows no obvious proof for induced magnetic moments, and it is 30 times smaller when compared with the Pt/Fe reference sample. Magnetotransport measurements show strong ferromagnetic characteristics in thin Pt films on a ferrimagnetic insulator [101; 105; 106; 107].

2.7 Rashba effect

The Rashba effect is the result of a combination between symmetry and spin orbit coupling. This effect is responsible for a spin splitting of a sub-band. When the spin orbit coupling is present alongside a breaking of the structural inversion symmetry, the Rashba effect occurs. It acts normal to the surface where the electron and the spin orbit coupling transforms into a magnetic field transverse to the current flow. The Rashba effect is represented by the Hamiltonian [108].

$$H_{Ra} = \frac{\alpha_{Ra}}{\hbar}(\mathbf{z} \times \mathbf{p}) \cdot \sigma \tag{2.13}$$

where α_{Ra} is the Rashba coupling parameter, dependent on the electric field strength, z is the symmetry-breaking axis, $\mathbf{p}$ is the momentum vector, and is σ a vector of Pauli spin matrices. For the free electron, the total Hamiltonian is giving by

$$H_{total} = \frac{P^2}{2m_e} + \frac{\alpha_{Ra}}{\hbar}(\mathbf{z} \times \mathbf{p}) \cdot \sigma \tag{2.14}$$

where m_e is the electron effective mass. From equation 2.14, the dispersion spectra shifted in wavevector **k** direction with energy

$$E(k) = \frac{\hbar^2 k^2}{2m_e} \pm \alpha_k \tag{2.15}$$

where the two possible spin directions ($\pm$) have eigen/states pointing perpendicular to **k**. The result of the Rashba effect is a spin-split conduction band. The spin degeneracy is a consequence of the time and spatial inversion symmetries. Figure 2.8 shows the energy dispersion relation and Fermi surfaces for a non-magnetic and a ferromagnetic system. In non-magnetic systems, the Rashba effect causes spins to align in the plane perpendicular to the electron momentum. In a ferromagnet, the Rashba effect acts against the exchange interaction, causing the spins to cant away from the magnetisation [109].

In the sense of generating a spin-current across an interface, the Rashba effect and the spin Hall effect are similar [81]. The angular variations of the interfacial Rashba-induced magnetoresistance and the SHMR are the same [6; 110; 111]. However, it is possible to distinguish these two mechanisms, since they have different NM film thickness dependences [112]. The SHE happens in the bulk, but the SHMR is due to the transfer of angular momentum at the interface, Furthermore, there is a dependence on the spin diffusion length. For SHMR, the maximum effect takes place when the Pt thickness is about the same as the spin diffusion length, whereas in the Rashba effect, the thinner the better.

Molecules may affect the Rashba effect and spin texture of the metal, leading to changes in the effective SOC of the hybrid wire [113; 114; 115]. Our results are more consistent with a change in the effective SOC and magnetic moment acquired by the transport electrons mediated by the introduction of C_{60}. It rules out mechanisms based on the formation of a perpendicular dipole, which arises due to charge transfer at the Pt/C_{60} interface and its associated potential step, which breaks the symmetry [116].
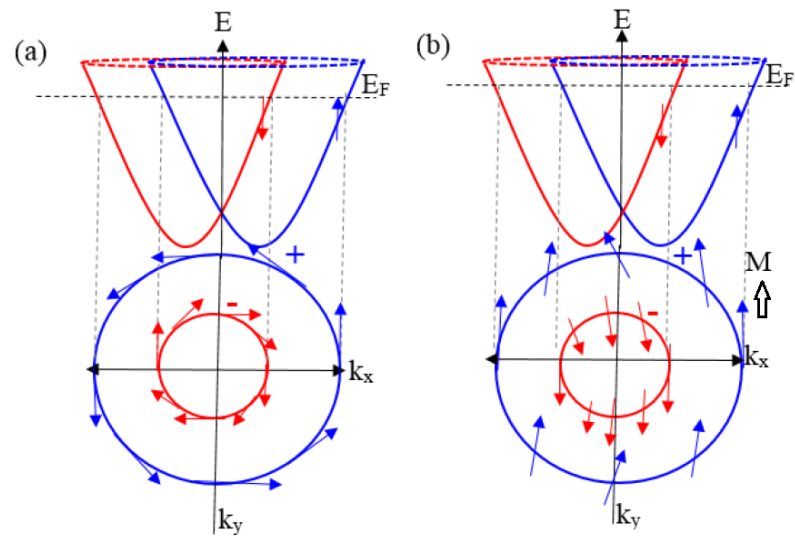
Figure 2.8: 2D representation of the energy dispersion relation (top) and Fermi surface (bottom) for both the spin majority (blue) and minority (red) charge carriers. (a) in a non-magnetic material and (b) in a ferromagnetic material with an applied magnetic field. Adapted from [109]

2.8 Spin physics in metal-molecular interfaces

In spintronic devices, interfaces play a very important part. Because of that, we require characterization techniques that allow us to probe the spin-dependent properties of the interface. It is usually difficult to transfer spins accross hybrid interfaces. It is also challenging to understand the behaviour of an interface consisting of two materials with very different conductivities, such as a hard metallic electrode in contact with a soft organic layer [117; 118]. The efficiency of spin injection into organic semiconductors is dependent on the spin-dependent properties of the interface. The emergent spin polarisation that can occur due to interfacial hybridisation has become a recent focus of research [119]. Several studies have been developed to understand the fundamental phenomena of the hybrid interfaces on magnetic surfaces. Cespedes et al. observed evidence for contact-induced magnetism at the interface between carbon nanotubes and a ferromagnet [120]. In 2010 Barraud et al. investigated the nature of the chemical bonds between the organic molecules and magnetic surfaces at the interface [121]. They hypothesized that the overlap between the ferromagnetic, metallic and molecular orbitals leads to the formation of spin-hybridisation-induced polarised states. This spin-hybridisation acts as an effective magnetic electrode and has a vital role in the magneto-resistive characteristics of the device [122]. In 2013, Steil et al. explored an important hybridisation step between organic molecules and magnetic surfaces by investigating the mechanism of the charge transfer across the interface. They studied the dynamics of the hybrid interface via pump-probe photoemission experiments and explained the role of hybrid states for efficient spin filtering properties [123]. In the theoretical side, calculations have been used by several groups to study the role of the hybridization between organic molecules and ferromagnetic electrodes on the spin injection process [8; 124; 125]. They have found that the variation of the electronic structure of the molecules is associated with the interaction at metal-molecule interfaces.

To better understand metallo-molecular interfaces, it is very important to consider how the density of states (DOS) of the two systems will change as they interact. As shown in figure 2.9, the electronic structure of ferromagnetic metals

is defined by a broad density of states which splits into majority and minority sub-bands corresponding to spin-up and spin down electrons, respectively [117]. For the organic molecule, the density of states are discrete molecular energy levels. Both the highest occupied molecular orbital (HOMO) and/or the LUMO can contribute to the current. The efficiency of the transport and spin injection is greatly determined by the relative alignment of the Fermi energy of the metal to the LUMO of the molecule. When the molecule is brought closer to the metal, the DOS gets altered in two possible ways. First, the molecular orbitals become broader, and electrons can leak in and out of the molecule, which leads to a broadening of the molecular DOS due to the interfacial hybridisation. Second case, the molecular energy level can be shifted, and a particular spin polarised molecular orbital can align with the E$_F$, which can be consequently dominating the charge current accross the interface [117].

2.9   Metal / C$_{60}$ Molecule Interface

Let's consider the interface created by a semiconductor with a conduction band Ec above the Fermi energy and an electron affinity Ea and a metal with work function φ. In both systems, the Fermi energy becomes a universal reference when these materials come into contact. However, because Ea + Ec $\neq \varphi$, aligning the Fermi energies at the surface means that the vacuum levels are not the same [126].

The difference in their Fermi levels provides an effective potential between the two systems. Due to the effect of this electric field, an interfacial dipole emerges at the metal-semiconductor interface. This potential in the semiconductor means that electrons at the interface have a higher energy than electrons at the vacuum level, essentially distorting the band structure so that the conduction band gets nearer to the vacuum level as one gets closer to the interface. When a contact is made between a semiconductor and a metal, the vacuum levels at the contact are similar, and the band structure distortion is largest. In terms of determining interfacial band distortions, the metal work function has significantly less influence than predicted. Because the valence and conduction bands in the semiconductor
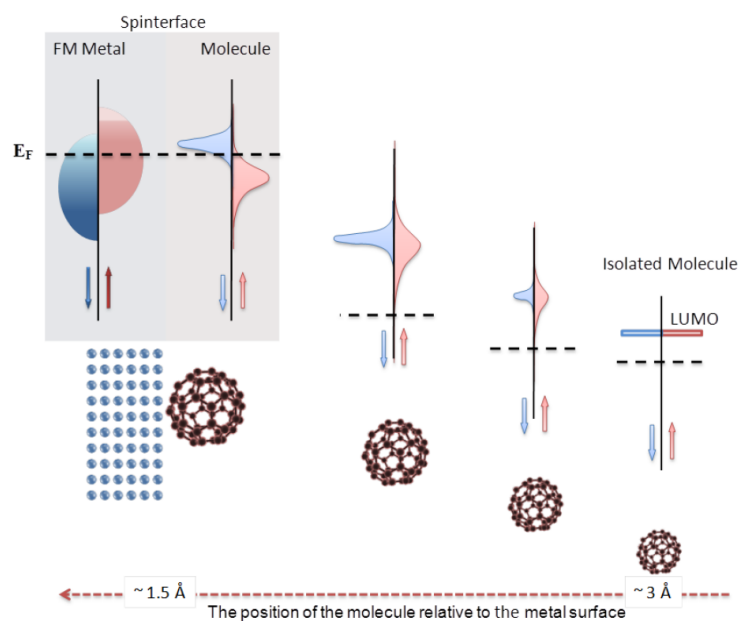
Figure 2.9: A schematic diagram of the molecular hybridisation with a ferromagnetic metal (FM). The DOS of both the molecule and the FM are at the top of the figure. At the bottom, the molecular energy level broadens and spin-dependent splitting occurs due to orbital hybridisation with a ferromagnetic metal surface. Moving from right to left makes the initial discrete molecular orbitals broaden and shift their position to the Fermi level EF of the FM. Taken from [117].

preferentially align to the Fermi level rather than the vacuum level, this weak dependency is known as Fermi-level pinning [127].

The ionisation potential of C$_{60}$ has been calculated to be about 6.9 eV [128; 129]. Given that the band gap between the HOMO and LUMO is roughly 2.3 eV, an E$_a$ of about 4.6 eV is expected. Several investigations of C$_{60}$ adsorbed onto a variety of metals, including Mg ($\varphi = 3.6$ eV), Au ($\varphi = 5.1$ eV), and Ag ($\varphi = 4.3$ eV), reveal charge redistribution from the metal into the molecular LUMO in all cases, demonstrating that vacuum level alignment is not required [56; 130]. Chemical interactions and electron transfer, on the other hand, cause charge redistribution and the creation of an interfacial dipole by distorting the electronic structure of a molecule at the interface. For a wide variety of transition metals, the broadening of interfacial orbitals aligns the LUMO below the Fermi energy in C$_{60}$, allowing charge transfer in which the LUMO at the interface is partially supplied by electrons from the metal, see figure 2.10.
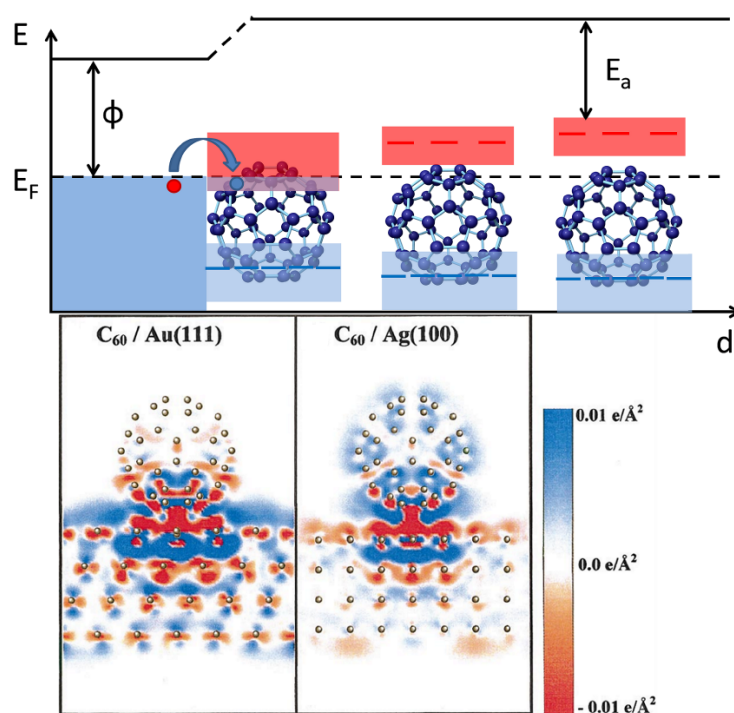
Figure 2.10: The interfacial coupling between a metal and C_{60} is shown. Because of the molecular orbitals hybridization and the redistribution of surface charge near the surface, the gap is narrow and the LUMO band is broaden. Thus, the LUMO moves to be close to the Fermi energy and this process is known as Fermi level pinning. A DFT simulation of a C_{60}/Au and C_{60}/Ag contact is shown in the bottom panel, with the ensuing charge redistribution traced across a small area. Taken from [131].

Charge transfer takes place at the interface where the molecular orbitals cross the Fermi energy through interactions between organic semiconductors and metals. The charge transfers to C$_{60}$ by hopping transport [132; 133]. Hopping transfer is needed overcome an energy barrier, since the charge carriers are localised [134]. Electron tunneling between localised states is assisted by phonons, so the hopping process is dependent on the temperature [135]. Therefore, as the phonon energy is reduced at lower temperatures, the hopping probability will decrease. This mechanism is called variable range hopping, implying different nergy barriers at each hopping. Equation 2.16 shows that the conductivity σ is dependent on the temperature T for a system of d dimensions (i.e. 1, 2 or 3), with b a parameter related to disorder.

$$\sigma = e^{-b/T^{1/(d+1)}} \tag{2.16}$$

The hybridisation at the interface will be a mix of molecular and metallic character and is contingent on the coupling strength between the molecule and the metal [136]. In the case of transition metals, the hybrid states form between the π conjugated and the d orbitals. It has been shown that interesting magnetic effects can be observed due to the interaction between molecules and transition metals [137; 138; 139; 140; 141; 142; 143]. Due to the change in the density of states at the Fermi energy, spontaneous magnetic behavior has been observed in normal metals. They confirm that the appearance of magnetic ordering from non-ferromagnetic materials arises from interfaces between thin films of 3d non-ferromagnetic metals and C$_{60}$ molecules.

CHAPTER 3

Experimental methods

3.1 Introduction

The experimental techniques that used to fabricate and characterise all thesis samples are in this chapter. The samples were grown by using sputtering deposition system and in-situ thermal sublimation. X-ray reflectivity (XRR) was used to investigate the structure of the samples like the thickness. Electron transport measurements (helium flow cryostat) were used to investigate the magnetoresistance from room temperature to 5 K. Magnetometry (superconducting quantum interference device (SQUID) vibrating sample magnetometry (VSM) was used to study magnetic properties.

3.2 Sputter Deposition

The sputter deposition growth process is based on production of the appropriate materials and transport of these materials through a medium to a substrate where they then condense to form a solid [144]. The deposition process here is an example of physical deposition, which means that it does not use a chemical reaction [2]. We used magnetron sputtering as shown in figure 3.1. A flow of pure argon (99.999% purity), which is chosen due to its inert nature, is introduced into the chamber to provide an atmosphere set to a pressure of several mTorr. Ar ions hit the surface of the source atoms, then the surface material is scattered due to the collisions with the Ar ions [145]. In magnetron sputtering , a metallic target of high purity is placed atop an assembly of permanent magnets, in order to confine the plasma by the Lorentz force. Mgnetron sputtering is used to increase the rate of film growth from the sputtering process and to allow a stable plasma to form at lower pressures. This sputtering process can be performed in two ways, direct current (DC) or radio frequency (RF) alternating current. The process used depends on the material that is desired to be deposited on material. DC sputtering is used to deposit metals (Pt, Ta and PtMn), while YIG target is insulating and so requires RF sputtering. C_{60} is grown by another deposition technique, high vacuum thermal sublimation. This is described in the following section 3.3.
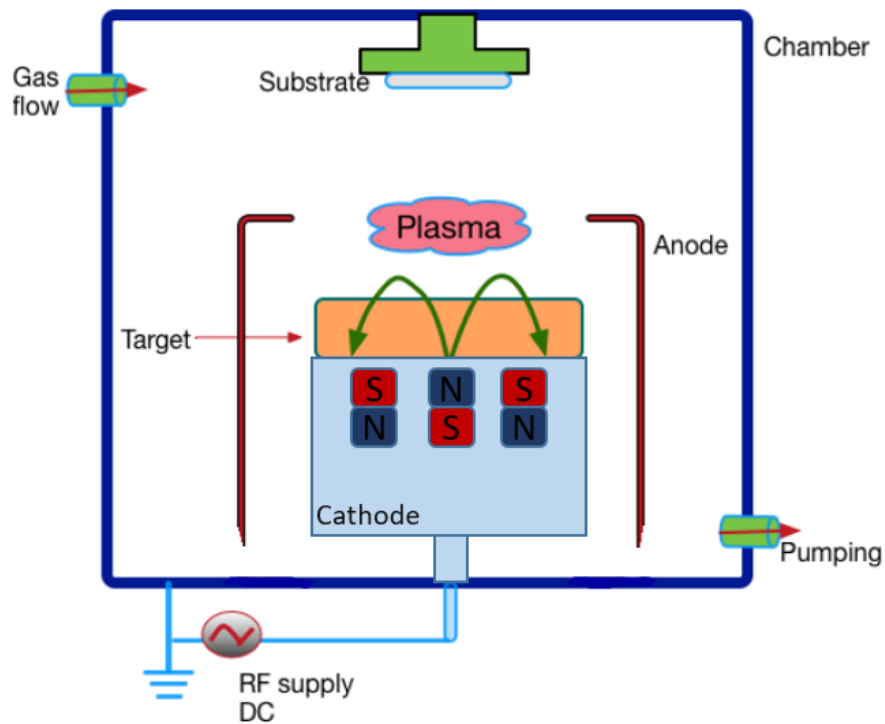
Figure 3.1: Schematic of the magnetron sputtering method. The target is the material to be deposited and it is shown as the cathode. The substrate is shown on a rotating sample wheel, which is electrically grounded. The distance between the target and the substrate is about 8-9 cm. The sputtering gas flows into the chamber and is then ionised to form the plasma. The plasma ejects atoms from the target that then diffuse to be deposited onto the substrate.

The operational process of the sputter system is run under vacuum conditions using a roughing pump to go from room pressure to 20-30 m Torr. By using a cryo-pump, a high vacuum (HV) environment with a base pressure of about 10^{-7} Torr is produced. Water is one of main residual components in the system beside nitrogen and oxygen but it is reduced by passing liquid nitrogen through a shroud inside the chamber. The final base pressure in the main chamber is typically of the order of 10^{-8} Torr. The chamber is filled with an inert growth gas, in this case argon, which generates a growth pressure of about 2.5 mTorr. The composition of the pressure and gas/water content in the chamber can be determined by using a residual gas analysis method of mass spectrometry [146]. Water is particularly harmful to metallo-molecular interfaces, and H_2O base pressures of $\sim 10^{-9}$ to 10^{-10} Torr are needed [147]. It has been seen that the quality of the C_{60} film degrades, which could be due partly to oxygen intercalation (and/or other gases) and perhaps decoupling of the molecules at the interface.

The sputtering system consists of eight magnetrons as well as an RF magnetron and an evaporation source for the deposition of C_{60} by thermal sublimation. To ensure consistent sample growth and to obtain a clean deposition process with good yield of high quality films, the following procedures are followed during this study. Substrates are cleaned in an ultrasonic cleaner first with acetone, then with isopropanol to remove residual acetone. These are then, dried using compressed air before the alcohol entirely evaporates now ready to loading into the deposition system. Just before the growth, all targets are subjected to a pre-sputtering cleaning process for 10 minutes before growing by energetic Ar ions bombardment to remove any surface contaminants and trapped gas [148]. Metal layers are deposited from DC sputter guns operating at currents of 25-50 mA and powers of 14 - 18 W.

A DC sputtering system has a cathode connected to the target material and an anode connected to the target. The cathode is biased at around -400 V and the anode is usually grounded. A DC voltage, typically of a few hundred V, is applied to ionise the Ar gas and accelerate the ions towards the target (anode) and sputters metal atoms into the chamber. Then, these metal atoms diffuse

through the plasma to the substrate above until the desired metal thickness is deposited on the substrate [149]. RF magnetron sputtering works similarly to DC, however a radio frequency AC current is applied. Since the YIG target is electrically insulating, the standard DC sputtering cannot be used as DC current cannot flow between the anode and cathode. In RF sputtering, AC current can be used, with the insulating target acting as a buffer capacitor. The wave property of the current becomes a factor in power transfer with a voltage oscillating at radio frequency, around 13.56 MHz [150]. In the power supply, a resonant circuit is adjusted to match the circuit impedance and prevent power being reflected back to the power supply. The YIG target has different elements, so the YIG film is deposited as a mixture of its constituent elements. The sputter rate and mean free path for each element will be different. Slowing down the growth rate by adding oxygen to the argon atmosphere allows the yttrium and iron to be deposited onto the substrate in the correct stoichiometry for YIG. The persentage of oxygen has been studied in much of the optimising work in the University of Leeds [2; 44; 151]. To yield the most accurate YIG stoichiometry, the proportion of O2 /Ar = 5 % and the RF power maintaines at 50 W at 13.56 MHz.

Gadolinium gallium garnet (GGG) is the standard substrate used in most studies to grow YIG film because of the matching lattice constant [2; 152; 153]. However, GGG has a strong paramagnetic signal [44; 151]. As consequence of the gadolinium diffusing from the GGG into the YIG during annealing, a gadolinium iron gallium layer (GdIG) layer forms [151]. The intermixed GdIG region at the GGG interface is magnetically dead at room temperature, but becomes antiferro-magnetically aligned to the rest of the YIG film below 75-125 K. This impedes the propagation of spin waves and therefore the transfer of angular momentum from the Pt layer in which the SHMR effect is based. Figure 3.2 shows an example of thick and thin YIG grown by RF sputtering and post-annealing at 850 °C in air. The dead layer effects on the magnetic properties of YIG where the temperature dependence of the magnetisation reveal a decrease in the low temperature region.

The use of shadow mask deposition in this study also allow to grow two metal wires (down to 100 μm in lateral size) simultaneously on the same YIG substrate
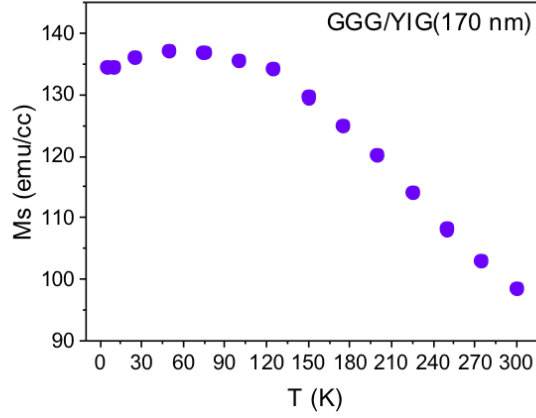
(a)
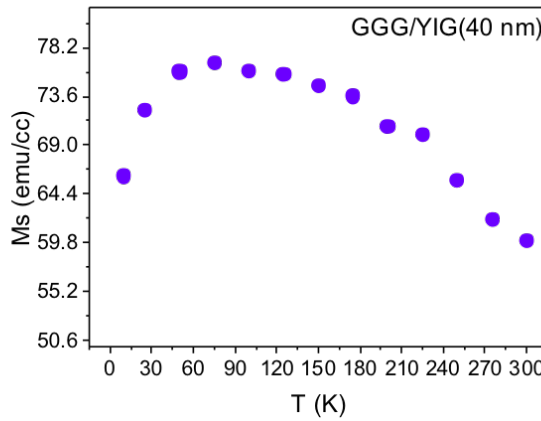
(b)

Figure 3.2: Temperature dependence of the saturation magnetisation for (*a*) YIG(170 nm) and (*b*) YIG(40 nm) grown by RF sputtering on a GGG substrate. Below 90 K there is a decrease in Ms at lower temperatures due to the presence of a GdIG layer antiferromagnetically coupled to YIG below that temperature. The extent of the decrease depends on the thickness of the YIG layer. The thickness of the dead layer has been measured to be some 6 nm, so the change in magnetisation for a 40 nm layer is approximately 17% (the ratio of GdIG to actual YIG, 6/34, is very close to the magnetisation ratio (77-64.4)/77.

without breaking vacuum. To deposit C_{60} (50 nm), we use another mask that is cut in the shape of a rectangle to cover one of the Pt wires without breaking the vacuum. These masks are mounted onto an inner wheel that moves independently of the sample holder, allowing the two wires to be made on the same sample and the C_{60} layer. In this way, we can ensure that both metal wires have the same thickness, film quality, and interaction with the substrate.

3.3   High vacuum thermal evaporation

C_{60} has a high molecular weight and low inter-molecular binding energy. This means that it can be evaporated easily in high vacuum [154]. The molecules are held in powder form inside a crucible which sits in a tungsten filament as shown in Figure 3.3. The tungsten filament is connected to copper electrodes through which a current of around 20 A is applied to apply heat to the crucible. Isolated C_{60} cages are remarkably stable up to very high temperatures and will refrain from coalescing until roughly 1500 K [155]. As the process is under high vacuum, the molecules can reach the substrate where they condense. The evaporation source is encased in a Cu shield, and water cooling prevents irradiation-induced overheating.

The C_{60} crucible is heated prior to sublimation to avoid the deposition of fullerene oxides and chemical impurities and producing pure fullerene films [156]. The base pressure in the system during the molecule sublimation is approximately 10^{-8} Torr [157]. To determine the molecule thickness of the deposited film on the substrate during the sublimation, a quartz crystal rate monitor sits above the crucible. The total growth can be determined through a resonant frequency. The resonant frequency in the crystals is changing as mass loading and deposited on the substrate. Thus, the growth rate can be increased and decreased by changing the current to the tungsten filament. It is important to calibrate the tooling factor by measuring the C_{60} film thickness via X-ray reflectivity and comparing to the value calculated by the monitor. C_{60} can be degraded very quickly under ambient conditions due to photo-assisted oxidation and hydration [158]. Therefore, it is vital that C_{60} is capped with Al to prevent chemical degradation.
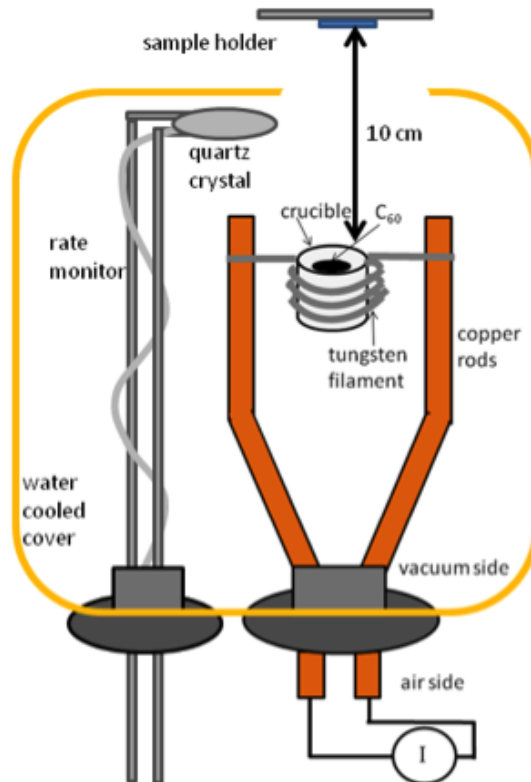
Figure 3.3: Illustration of the thermal sublimation source interior. Taken from [147]. The C_{60} molecules are placed in a crucible which is attached to the copper rods and heated by a tungsten filament. The cooled water is cycled around the copper shield to prevent excessive heating. The quartz crystal monitors the deposited thickness of the molecular film. The sublimation of C_{60} works as a centre track, so the substrate needs to be far enough from the crucible to receive atoms properly and to avoid the heating from the tungsten filament.

3.4 X-ray measurements

We use two kinds of X-ray measurements to study our thin films. X-ray diffraction (XRD) is an essential tool in the determination of crystal structure [159]. It is based on the diffraction phenomenon: when matter is illuminated with a beam of X-ray photons, this may result in a coherent scattering of these photons. The scattering is due to the interaction of photons with the bound electrons. The scattering will be coherent when it occurs without an alteration of the wavelength, and when the wavelength is changed, the scattered waves interfere to give diffracted waves. By using Bragg's law (3.1) the interference pattern can be used to characterize the structure of the material.

$$n\lambda = 2d \ sin\theta \tag{3.1}$$

X-ray reflectivity is a measurement of the scattering light intensity, reflected by a sample surface as a function of the incident angle. When the angle of incidence is smaller than a critical value, there is total reflection of the photons. When the incident angle exceeds the critical angle, all incident X-rays will be reflected, and if they are equal, incident X-rays will propagate along the sample surface. When the Bragg condition is satisfied for an integer number of total internal reflections, multiple reflections can incur in interference fringes. This leads to oscillations in the reflectivity curve, which are known as Kiessig fringes. By using the Kiessig equation (3.2) one can estimate the thickness of the sample and analyse the angular distribution.

$$\lambda = 2t \ \sqrt{sin^2\theta_m + sin^2\theta_c} \tag{3.2}$$

Where λ is the wavelength of the X-rays, m is an integer, θ_m is the angular position of constructive peaks and θ_c the critical angle [160]. XRR is used to find out film thicknesses density, and roughnesses. XRD is a technique used to give information about the structure of a crystalline material at the atomic scale.

3.5 Transport measurements

3.5.1 Cryostat measurements

A cryostat allows the measurement of transport properties at a controlled temperature. The system as shown in figure 3.4 consists of a variable temperature insert (VTI) which controls the temperature from 1.4 K to 300 K. The VTI is placed in a helium (He) reservoir which is surrounded by an outer reservoir of liquid nitrogen. The use of a high vacuum space between the He and N_2 and between the N_2 and the environment reduces heat loss. A needle valve is used to control the flow of helium gas, and the temperature is controlled by a heater as shown in the figure 3.4. A split pair of superconducting magnet coils was used to apply magnetic fields of up to 3 Tesla (T). The liquid helium keeps the magnet below their critical temperature and acts as the source of helium for gas flow. The sample can be rotated in the applied magnetic field, where there is a motor that is connected to the stick on top of the cryostat.

The samples sit close to the bottom of the VTI on a Cu mount, which is able to change depending on the magnetic field orientation(s) required. The sample wire bonds onto a chip carrier, which has pogo pins connectable to the sample mount. By connecting the sample mount with a stainless steel that has a low thermal conductivity, the sample wires feed to a port at the top of the cryostat. All electrical wires are in twisted pairs, where negative and positive lines are twisted together to eliminate noises inductively coupled to external electromagnetic waves.

SHMR has a distinctive angular dependence that can be observed by rotating the sample in a fixed field and measuring the change in resistance. The field applied must saturate the magnetisation of the YIG film. During measurements, the temperature is monitored using a cernox thermometer mounted on the brass sample holder.
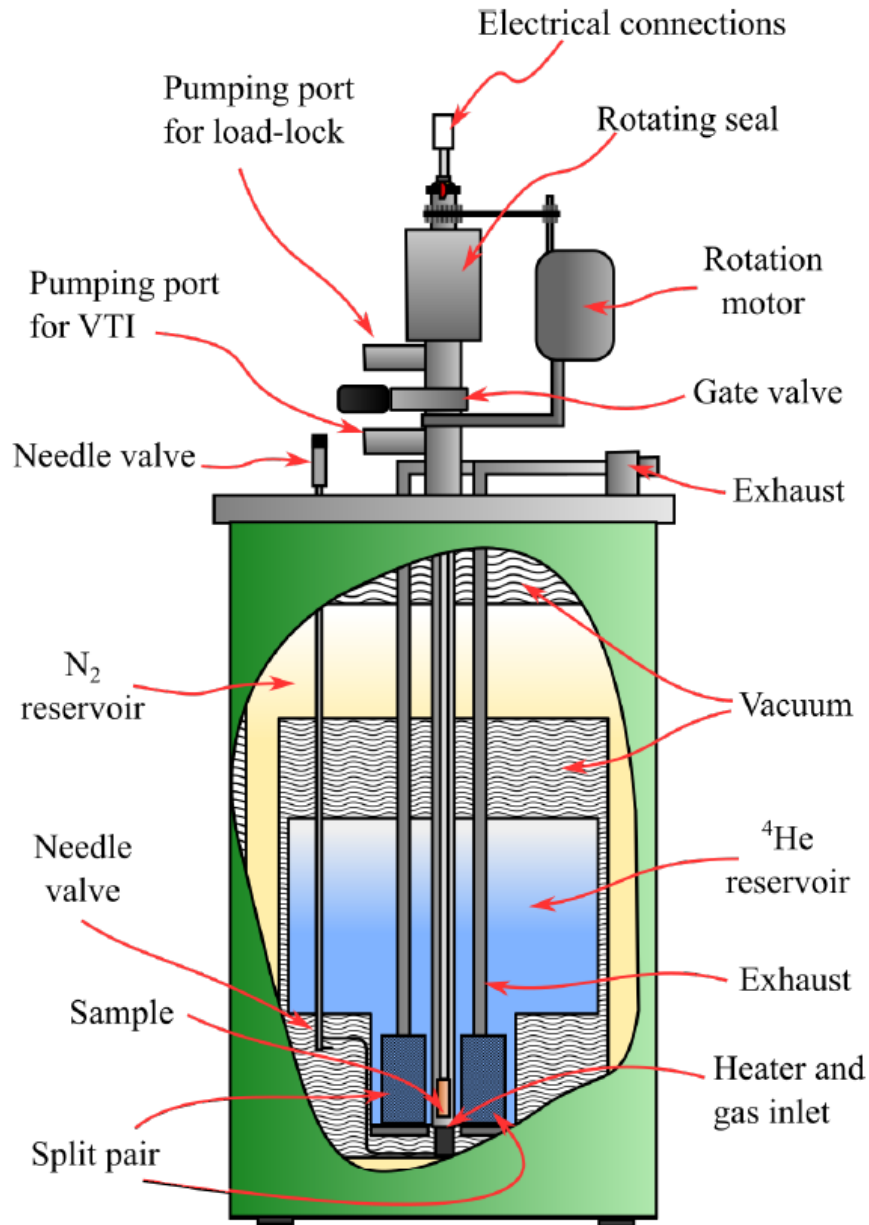
Figure 3.4: Schematic of the Cryogenics Instruments cryostat. Taken from [161]. The VTI is controlling the temperature degrees. The needle valve controls the amount of Helium gas. The magnetic fields are applied by a pair of superconducting coils. The liquid helium reservoir is keeping the temperature stabilized.

3.5.2 Electron transport measurements

In the spin transport measurements, an important parameter to be measured and to confirm that the spin transport channel behaves in an ohmic way, is the transport channel resistance. As shown in Figure 3.5, the two metals (Pt, Ta and PtMn) wires were deposited on top of YIG, one is then covered in C_{60} while the other is not. Determining the resistance of a nanowire requires a four probe method and a constant current supply illustrated in figure 3.5. By measuring voltages in this method, there is no potential drop along the probes and contact resistances are eliminated. The thickness is determined by XRR which cannot be used on wire individually, so calibration samples are used. The same material is grown in sheet form or with two wires via the mask placed on a comparable sample. The four probe method is used to measure wire resistance with a current of 1 mA. This yielded a good signal-to-noise ratio without producing enough Joule heating to affect the wire resistance. The contacts were bonded with aluminium wire onto the metal wire (Pt, Ta, and PtMn) and used a travelling microscope to measure the distance between the inner voltage probe edges. By the same method, the contacts were bonded onto the metal/C_{60} wire. We can rely on the wire bonding (contacts) on the metal wires through C_{60} because the resistance is reasonable. The resistance for metal/C_{60} wire is about kΩ, and if the wire bonding was not reached to the metal, we would have very high resistance (MΩ). Also, the I-V curve measurement will not be ohmic if the contacts were bonded only on C_{60}. Thus, the electrical conductivity is determined from the resistance, the cross sectional area and length between the voltage probes. The resistivity will follow the equation 3.3.

$$\rho = \frac{R * A}{L} \tag{3.3}$$

Where ρ is the resistivity, R is the resistance of the area of interest, A is the cross-sectional area and L is the length between the voltage probes. Electrical measurements were performed using a Keithley 6221 current source coupled to a Keithley 2182A nanovoltmeter in order to minimise the noise level.
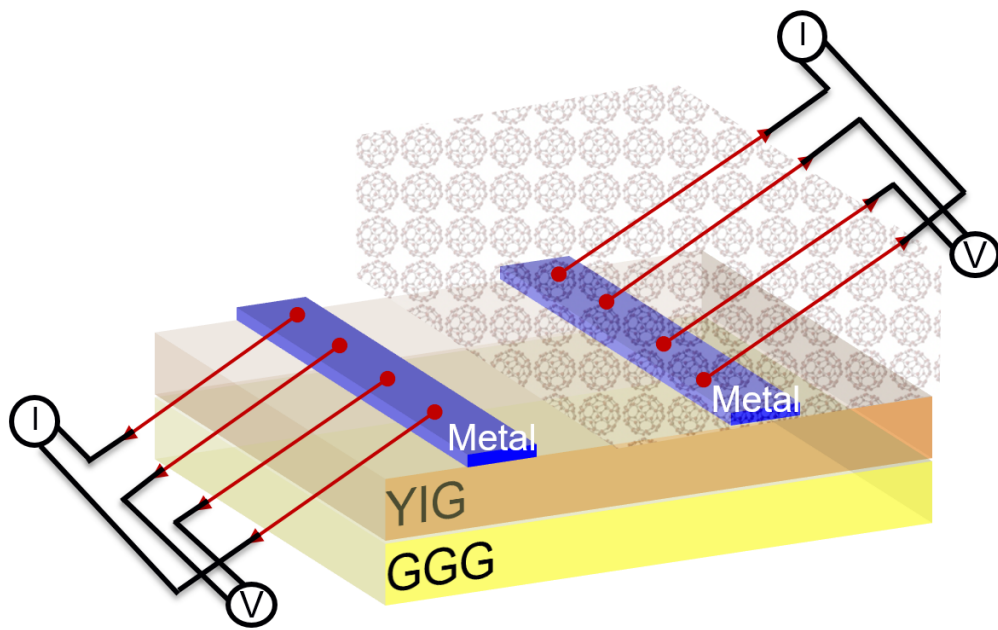
Figure 3.5: A schematic of the sample structure. A YIG film is first deposited on a GGG substrate. Two metal (Pt, Ta, PtMn) wires are deposited on the top of the YIG film and the C_{60} is covering the right metal wire. A current flows through the outer two points in the Pt wire, and the inner two points are used to sense the voltage signal.

3.5.3 Sample annealing process

As previously discussed, YIG films were deposited via RF sputtering in a Ar/O atmoshere on gadolinium gallium garnet substrates. GGG has a lattice constant of 12.383 Å, which matches well with the lattice constant of YIG 12.376 Å [153]. Having a close match between the lattice constants minimises interfacial strain [162]. Annealing was performed post-growth at 850 °C for 2 hours in a tube furnace with the samples annealed in air. This improves the crystalline quality and stoichiometry across the film.

In the case of anealing metals (Pt, PtMn), samples were placed in a tube furnace to be annealed at different temperatures (200-300 °C.) for eight hours at a pressure of 10-5 Torr. To prevent strain on the films, the tube furnace warms up to a specified temperature and then cools down to room temperature at a constant pace of 5 °C per minute.

3.5.4 Magnetoresistance measurements

There are three planes used of the magnetic field (H) with respect to the electrical current and the YIG film -see figure 3.6. For a field which rotates in the plane of the longitudinal to transverse orientation, this is named the α-plane magnetoresistance. To measure only the SHMR without AMR effects, we rotate H from perpendicular to transverse (change in β) as the current and field are always perpendicular. The third orientation is in the γ-plane. Here, only the AMR is measured. In this case, the field rotates between the longitudinal to perpendicular orientations. In the γ-plane, the field is always perpendicular to the spin orientation, which leads to the AMR and because of that no SHMR can be observed.
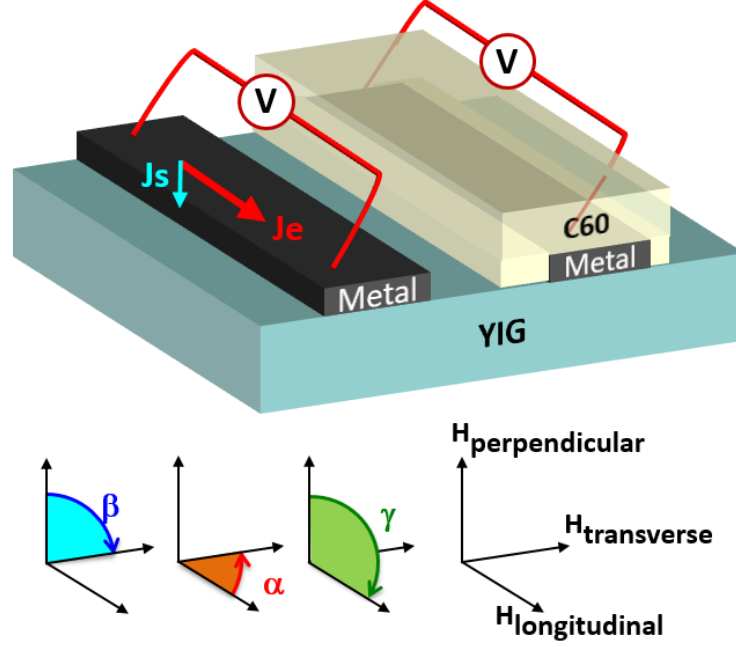
Figure 3.6: The nomenclature for the measurement planes and orientations for the magnetoresistance measurements. The SHMR is measured by rotating the angle in β. The field does rotate with respect to the charge current, which causes the AMR to manifest in γ. The α-plane MR thus results in a combination of the SHMR and AMR.

The relative change in resistivity is used to characterise the conventional MR as in following equation 3.4.

$$\frac{\triangle \rho}{\rho_0} = \frac{\rho_{max} - \rho_0}{\rho_0} \tag{3.4}$$

Where ρ_0 is the resistivity at zero applied field, ρ_{max} is the resistivity at the maximum applied field and $\frac{\triangle \rho}{\rho_0}$ is used to quantify the MR. From the angle-dependent MR, the SHMR and AMR are defined. The way to calculate the error bars for SHMR is from this equation (Error in SHMR/SHMR)$^2 = (\frac{\Delta B}{B})^2 + (\frac{\Delta A}{A})^2$, where A is ρ_0, B is $\rho_{max} - \rho_0$. However, $(\frac{\Delta A}{A})^2$ is very small so, it is neglect.

In figure 3.7 (a), the SHMR is measured by rotating the angle β, with the applied H field (and therefore M) always orthogonal to the electrical current,

but varying from in-plane to out-of-plane, and therefore from parallel (R_{min}) to perpendicular to the spin polarization (R_{max}) [13], [163] [164]. The AMR is measured by rotating the angle γ, with the applied H field in figure 3.7 (b). The resistance maximum takes place when the magnetisation is parallel to the current direction and minimum when the magnetisation is perpendicular to the current flow.
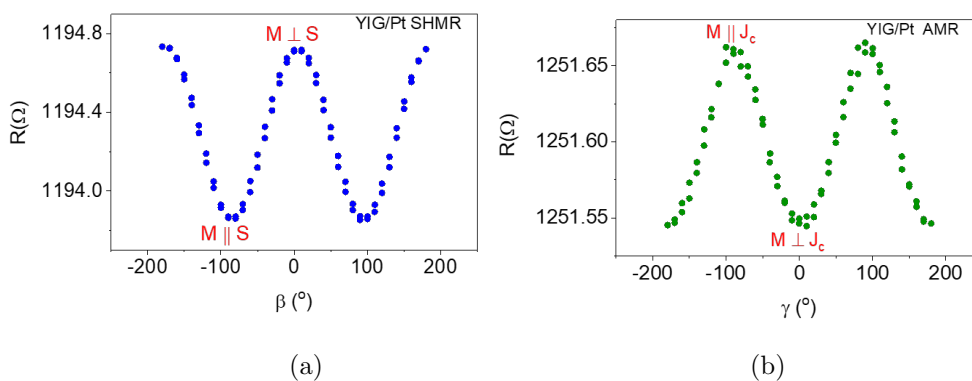
Figure 3.7: The figure shows the SHMR (β plane) and AMR (γ plane) orientation by varying the angle between the film and the magnetic field in (a) and (b). The SHMR magnitude is small when the angle between M and the spin orientation is 90° and large when the angle between them is zero°. The magnitude of AMR is large when the magnetic field longitude with J_e and small when they are perpendicular.

3.6 Superconducting quantum interference device

A SQUID-VSM MPMS3 is used to study the magnetic properties of the samples with a magnetic moment sensitivity of about 10^{-8} emu. It allows the measurement of the total magnetic moment in the sample over a broad range of temperatures from 1.8 K to 400 K and magnetic fields up to 7 tesla. The measurement is achieved by oscillating the sample near a pair of opposite wounded pickup coils. This is done to take advantage of the fact that the signal being measured is small

when compared to the background noise. Based on Faraday's law, the vibrating sample generates an alternating magnetic flux within the coils that induces a voltage signal in the pick up coil [165].

The measurements are performed through a system of superconducting detection which consists of two Josephson junctions set in a loop of superconducting material. The two junctions are parallel in a superconducting loop [166]. Through detection coils, the sample is vibrating and then produces a change in flux in the detection coils as shown in figure 3.8. The detection coils are configured as a second order gradiometer to reduce signals from external field. The second order gradiometer is composed of a central coil with two symmetrical end coils connected in series and in opposition to the central coil.

In the absence of an external magnetic field, the input current splits equally through the Josephson junctions. However, a screening current begins circulating in the superconducting loop and generates a magnetic field when a small external magnetic field is applied. As soon as the current exceeds the critical current of the junction, a voltage appears across the junction. As the magnetic flux is increased, the screening current increases and the junctions become momentarily resistive when the magnetic flux reaches half a quantum. At half quantum of the flux, the screening current changes sign and it goes to zero at one flux quantum. This variation of the current in the detection coils leads to a change in magnetic flux and generates an output voltage V which is related to the magnetic moment of the sample. A SQUID feedback circuit is used to cancel the current in the detection coils except the induced current owing to a flux change due to the oscillating magnetic sample [167], [168]. By measuring the magnetic moment at various field values, hysteresis loops can be obtained for different magnetic materials and various temperatures and fields.
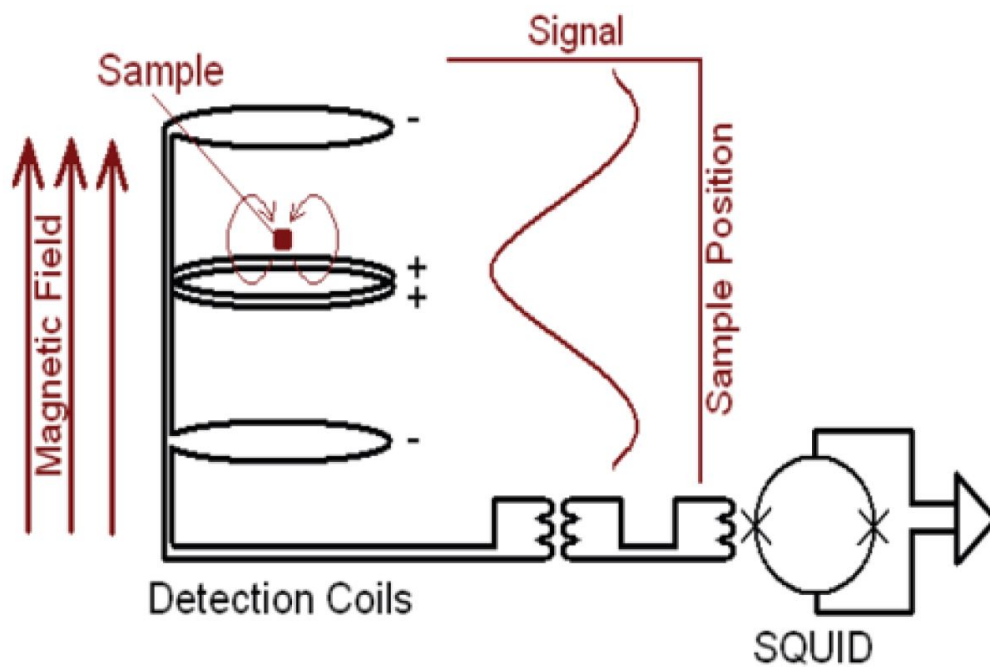
Figure 3.8: The configuration of a magnetometer with detection coils allows high-resolution measurement of the properties of magnetic thin films. A magnetic sampe size is about $4{\times}4$ mm^2 which vibrates at 14 Hz with an oscillation amplitude of 5 mm. Taken from [169].

CHAPTER 4

Spin Hall magnetoresistance in YIG/Pt and YIG/Pt/C$_{60}$

4.1 Introduction

This chapter introduces the investigation of the spin-dependent transport properties of Pt and Pt/C_{60} over a range of Pt thicknesses and temperatures. Due to charge transfer from the metal to the molecules, a conducting layer is formed at the interface between Pt and C_{60}, increasing the conductance of in Pt/C_{60} wires with respect to those of pristine Pt. In this chapter, SHMR measurements have been studied at a field of 0.5 T (pure SHMR), where the YIG is saturated for all orientations but other field-dependent effects remain comparatively small. At lower fields of 1-30 mT, there is an anisotropic magnetoresistance, enhanced for all temperatures and Pt thicknesses by C_{60}. We compare the results obtained using GGG and Yttrium Aluminium Garnet (YAG) substrates. Density Functional Theory (DFT) simulations in figure 4.22 were carried out by Drs. G. Teobaldi and E. Poli at the Scientific Computing Department of the Science and Technology Facilities Council (SCD-STFC). In this chapter, we investigate transport properties of Pt and Pt/C_{60} after annealing at 200-300 °C.

4.2 Spin Hall magnetoresistance in platinum

4.2.1 Resistivity dependence on temperature

Figure 4.1 shows the measured resistivity as a function of temperature for Pt and Pt/C_{60} on the top of YIG/GGG substrate. The sample has two Pt(3 nm) wires that both wires are grown at the same time, with one of them covered by C_{60}(50 nm) and the other a control sample without C_{60}. The general shape of the platinum resistivity describes ρ vs T for metals, and this was consistent with experimental literature [24; 92]. However, when the temperature is below nearly 20 K the temperature dependence of the resistivity changes. An upturn in resistivity is often observed in metals due to Kondo scattering or weak localization [170; 171; 172]. The resistivity for Pt with C_{60} is lower than for bare Pt wires because the interface between the C_{60} and Pt is metallised due to charge transfer and orbital re-hybridisation, contributing to the conductivity. With C_{60} on top, the Pt resistivity is about 40 % lower, and the upturn at low T is absent.

According to DFT calculations for Pt/C_{60}, 0.18-0.24 electrons per C_{60} molecule are transferred, and the only first molecular layer is metallised [18]. Thus, the Pt wire with C_{60} has an effective thickness greater than the Pt wire without C_{60}. From our measurements, the added conductivity is equivalent to some 1 nm of Pt, although we do not know the resistivity of this hybrid layer and its thickness is likely different. Also, this is the reason why weak localization is less apparent in Pt/C_{60} than Pt. Weak localization is stronger in low-dimensional systems. A change of the effective conducting layer thickness of 1 nm can result in very significant changes in the weak localization because we are increasing the layer thickness by as much as 67% (1.5 vs 2.5 nm thick). However, the fact that the hybrid conducting layer extends only for 1 nm is a hypothesis based on DFT simulations of the metallization and charge transfer at the interface. It is possible that the hybrid layer has a higher resistivity and is therefore thicker.

The resistivity drops faster in Pt/C_{60} wires than pure Pt. In thinner (Pt), the effect of the resistivity is dominated by surface scattering, but in the effectively thicker (Pt/C_{60}), the effect of phonon scattering is stronger. At room temperature, the resistivity of a metal is dominated by electron-phonon scattering. Figure 4.2 (a) shows the resistivity of Pt wires as a function of the metal thickness. The surface scattering plays a dominant role in the thin wires which are used for measuring the SHMR. Also, it has been reported that other factors, such as the surface roughness and defects in the platinum structure, will affect the resistivity [173; 174; 175].

(a)

(b)
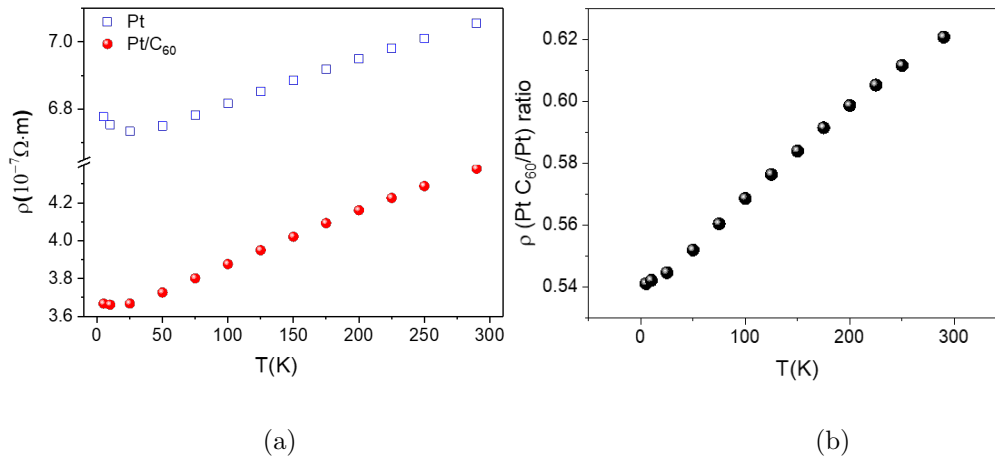
Figure 4.1: (a). Resistivity (ρ) as function of temperature (T) for a plain Pt wire shown in blue colour and red colour for Pt with C_{60}. The resistivity ratio of a Pt wire and a Pt/C_{60} wire are presented in (b).

The resistivity and residual resistivity ratio (RRR) give information about the scattering in the sample. Boundary scattering contributes to reduce the RRR for Pt vs. Pt/C_{60}, but the difference is lost in the noise for the thickest films of 18 and 25 nm. The resistivity at low temperatures is dominated by impurities, defects and grain boundaries. The RRR value of a metal is defined as the resistivity at 290 K, R_{290K}, divided by the minimum resistivity at 5 K, R_{5K}, for the individual wires:

$$RRR = \frac{R_{290K}}{R_{5K}} \tag{4.1}$$

The RRR for Pt and Pt/C_{60} is shown in figure 4.2 for different Pt thicknesses. C_{60} modified the density of state (DOS) and transport properties of the metal. This reduces the electron surface scattering, improving the residual resistance ratio (RRR) as shown in figure 4.2 (b). For thicker films, the additional conducting hybrid interface increases the RRR but the effect is much smaller because 1 additional nm in a 25 nm sample is only 4%, compared to 50% in a 2 nm wire, and the smaller effect may be lost in the noise, uncertainty or other additional

effects. The additional conducting hybrid interface reduces boundary scattering and increases the RRR for films $\leqslant 11$ nm.

(a)

(b)
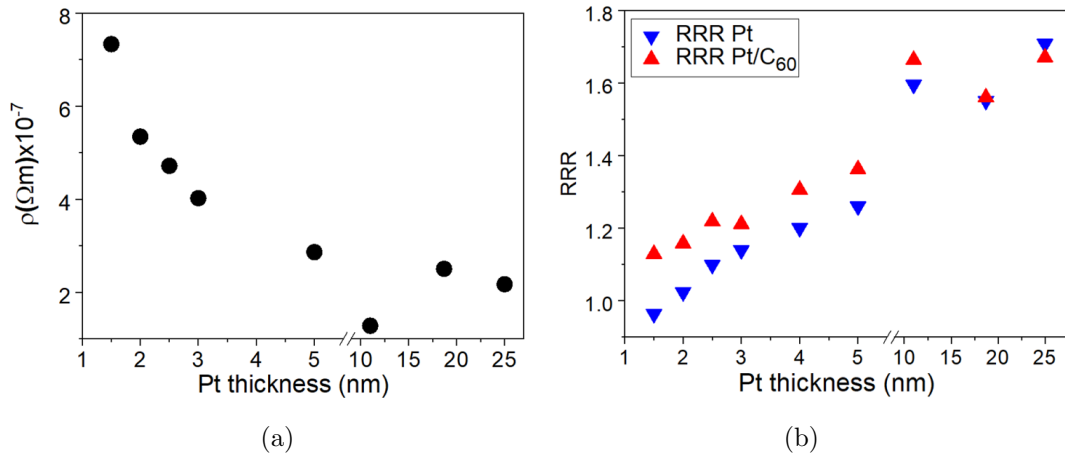
Figure 4.2: (a) Resistivity of Pt wires as a function of the metal thickness is shown. The shape of the platinum resistivity follows what is expected for a NM as function of sample thickness. The RRR of Pt and Pt/C_{60} are presented in (b).

4.2.2 Field dependence

In figure 4.3, field sweeps were used instead to determine the angular dependence. The field sweeps were done perpendicular to the wire along the out of plane YIG hard axis. Thus, it is possible to observe the SHMR contribution, of the order of several 10^{-4}, that saturates at the anisotropy field of the YIG film, some 100-150 mT at room temperature, and no higher than 0.5 T for any film or temperature measured. In this field range, the Pt/C_{60} wire has a larger magnetoresistance than pure Pt. Above 0.15 T, other contributions, such as Kohler magnetoresistance, localisation and/or the Hanle effect, become significant and result in a parabolic or linear MR. The MR increases with the applied field and assumes a B^2 field dependence to fit the date, which is consistent with Kohler MR. [176]. A possible explanation for Kohler MR is after an externally applied magnetic field, conduction electrons are displaced from their trajectories by the Lorentz force [177]. Also, when applied magnetic field is perpendicular to the spin polarization, the Hanle effect increases the resistance of the NM layer. This MR arises from the dephasing of spin accumulation by an external magnetic field [178; 179; 180]. The localisation effect has been reported in Pt thin films for temperatures below 50 K, which might give also an additional contribution to the parabolic field dependency [91; 181; 182]. At lower temperatures, the phonon contribution to the resistivity is greatly reduced, and an electron may scatter backwards, increasing the resistivity. The effect is cancelled by an applied field, reducing the sample resistance in the phenomenon known as weak localization. However, in metals with high spin-orbit coupling, weak anti localization (WAL) can take place [88; 182; 183]. The spin of the electron in this case is altered upon backscattering and reverses the observed magnetoresistance.

Figure 4.3 (b) confirms the existence of WAL in our samples at 5 K. In the case shown in figure 4.3 (a), the C_{60} overlayer enhances the SHMR signal by about a factor 3 due to the higher Pt spin orbit coupling, but reduces other contributions due to the increased effective (conducting) thickness of the Pt/C_{60} bilayer. However, when measuring at larger fields of up to 3 T, the low dimensional magnetoresistance due to localization results in a polynomial dependence of the

resistivity with the magnetic field [91]. This localization MR is much stronger in pure Pt, as the wires have a smaller effective thickness. When measuring SHMR, if high fields are used, it is not possible to compare the SHMR (dominated by SOC) and these weak localization effects (guided by dimensionality). It is clear that C_{60} has enhanced the SHMR, but at higher fields the pure Pt has higher MR (not SHMR) values.
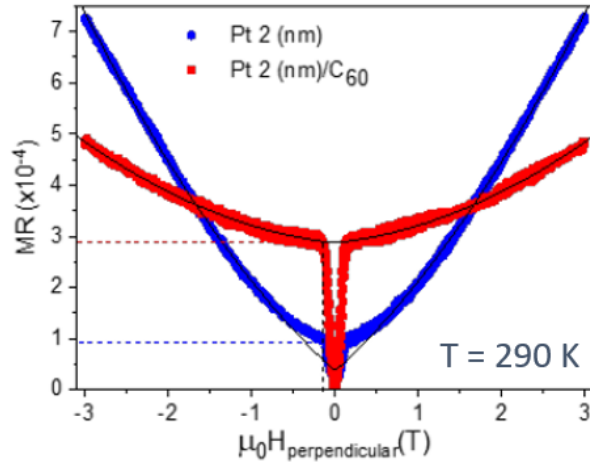
(a)
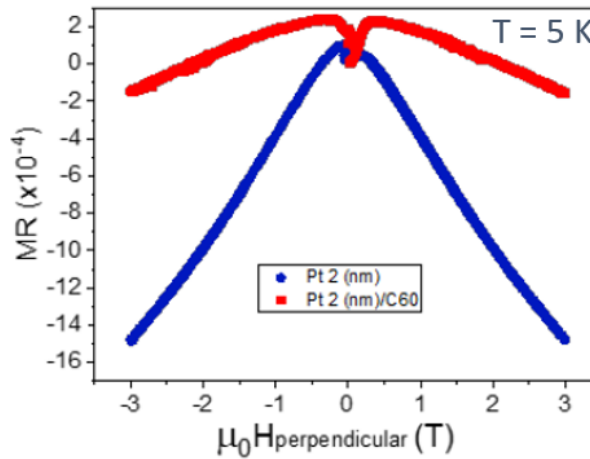
(b)

Figure 4.3: MR in a Pt wire with perpendicular magnetic field at room temperature in (a) and 5 K in (b). For YIG/Pt sample in (a), the C_{60} layer increases the SHMR due to spin accumulation by about a factor 3, but reduces the polynomial MR contributions because of the increased effective thickness of the Pt/C_{60} bilayer. (b). A negative contribution from a different MR that becomes stronger at low temperature.

56

Metals show a magnetoresistance that is dependent on the strength of the applied magnetic field [176]. Here we determined the effect of C_{60} on the effective SOC and the impacts on the SHMR measurements by angular rotations at a range of applied field strengths. According to the SHMR theory, the effect should be independent of the magnitude of the applied field above the saturation field of the YIG [4; 5]. The highest field is required to saturate bulk YIG out of the plane is 0.27 T. However, figure 4.4 shows the field dependence of the signal measured in the β-plane (β-plane in 3.5.4 section). The resistance shows a cosine squared behaviour with respect to the magnetization orientation, as expected for SHMR experiments [4; 5]. This measurement is taken at 290 K with applied magnetic fields from 0.5 to 3 T. The SHMR should be field-independent; the difference between the measurements must be due to other magnetoresistive effects.
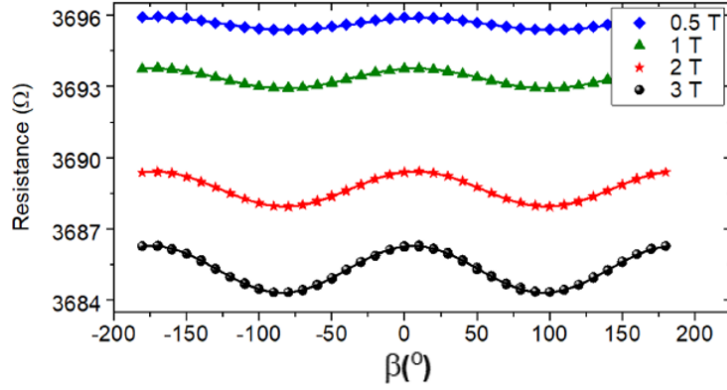
Figure 4.4: Resistance with different applied fields as a function of the magnetic field in the transverse to perpendicular configuration (β angle). The data is fitted to a $\cos^2(\beta)$ function. We take the amplitude at the lowest field of 0.5 T, when the YIG substrate is saturated but the polynomial contributions are small, as the SHMR value.

Figure 4.5(a) shows the change in the measured MR (i.e. the change in resistance as a function of the angle β as shown in the in Fig. 4.4) as a function of the applied magnetic field. Although the SHMR saturates at or below 0.5 T (YIG magnetization completely out-of-plane), other MR contributions, such as ordinary MR [184; 185] and localization, are also dependent on the angle of the applied magnetic field and may inflate the real SHMR values. The total MR measured is roughly linear with the magnetic field. These contributions are stronger for thinner films - see figure 4.5 (b), and therefore for Pt as compared to Pt/C_{60}, the latter of which has an additional hybrid conducting layer. To avoid these other mechanisms from affecting our SHMR analysis, we carry out all our measurements at the minimum field at which we are confident the YIG is saturated for all orientations and temperatures: 0.5 T. Figure 4.5 (c) shows SHMR at saturated value (0.3 T). The SHMR at 0.3 T is 6×10^{-4} and at 0.5 it is 6.2×10^{-4} that means the SHMR has changed by (0.2/6.2) x 100 is about 3 %. This means that measuring at 0.5 T makes a 3 % change in the SHMR (i.e. 3 % on a 10^{-4} magnetoresistance), which is similar to our level of resolution in the resistivity (one part per 1-10 million) and therefore not a significant difference. Furthermore, we cannot measure the out of plane saturation magnetic field for GGG/YIG below 50-100 K due to the massive paramagnetic contribution of the much heavier GGG substrate at low temperature. Therefore, it is possible that the out of plane saturation field is larger than 0.3 T for some of the temperatures/films measured.

The values we report for Θ_{SH} are similar to those reported in the literature for YIG/Pt (Θ_{SH} of the order of 0.05-0.1), although we use a different YIG growth method to most other groups (RF sputtering) as we discussed previously. It is to be noted that Θ_{SH} is derived from a fit of the SHMR, so the value obtained will be higher if the magnetic fields used are larger, or if the spin-mixing conductance value used in the fit is smaller. Most papers use magnetic fields of 1 to 9 T [6; 92; 93], whereas we use 0.5 T, just enough to saturate the YIG out of plane, but not so big that it brings additional magnetoresistive effects, in particular at low temperatures (weak localisation, ordinary MR etc.). If we had carried out

our measurements at fields of e.g. 3 T, as many other groups do, we would (erroneously) report Θ_{SH} values 2.2 times higher, of Θ_{SH}=0.1300±(0.0009) for pristine Pt, and Θ_{SH}=0.090±(0.001) for Pt/C_{60}. This results in an artificially larger spin Hall angle for Pt at higher fields, which must be taken into consideration when comparing our results to the literature.
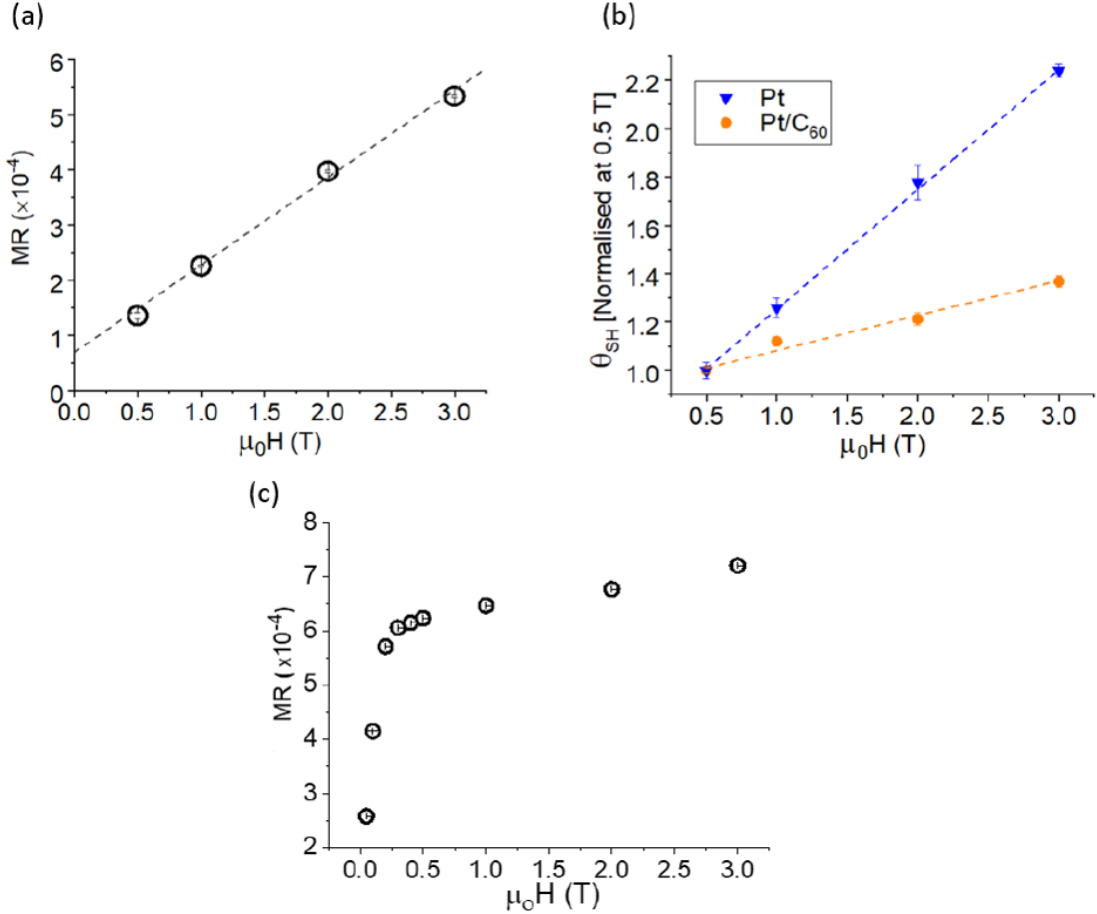
Figure 4.5: *a)* The MR is roughly linear with the applied magnetic field when the field exceeds the out of plane saturation for YIG. Larger SHMR results also in bigger spin Hall angle in (*b*). However, this increase is an artefact of using the same fit for data that includes contributions to the MR other than the spin Hall MR (weak localisation, thin film MR). (c) shows the sharp increase in MR due to the SHMR before the YIG saturates.

4.2.3 Fitting of the SHMR

The SHMR is obtained by fitting the change in resistance as the angle β is varied from perpendicular to transverse. Figure 4.6 shows an example of this fit for a Pt wire and its Pt/C_{60} partner. The SHMR vs temperature data show a change in the spin Hall angle between Pt and Pt/C_{60} - whilst keeping the same spin-mixing conductance. The fit in line appears a good match to the data across the full temperature range. We fitted the SHMR using equation 2.9 to get a qualitative idea of variations in the different parameters contributing to the SHMR, although only those values that are experimentally determined can be used to compare pure metal and metal-molecular layers: resistivity, magnetoresistance (anisotropic and spin Hall), and magnetization. We treat Pt/C_{60} as a single layer, but we do not know how thick the C_{60} layer contributing to the resistivity is. Simulations seems to indicate that only the first molecular layer in contact with the metal is conducting ($\sim$1 nm), but we cannot confirm this experimentally. There are no equivalent models for two conducting layers.

The only parameter not determined by the experiment (conductivity, temperature), nor set as a fitting parameter (spin Hall angle, spin diffusion length) is the spin-mixing conductance, which we have used the value derived in Althammers review paper of $4 \times 10^{14} \Omega^{-1} m^{-2}$ [6]. The initial values that are set as fitting parameters for spin Hall angle and spin diffusion length are 0.05 and 5 nm, respectively. Figure 4.7 shows the dependence of Θ_{SH} on the value with $G_{\uparrow\downarrow}$ although Θ_{SH} is larger for Pt/C_{60} in all cases. The spin Hall angle can be artificially inflated by using smaller values for the spin mixing conductance. Note that the change to the spin-mixing conductance do not change the effect of the molecular layer.

Figure 4.8 shows the spin diffusion length as a function of Pt thickness as derived from fitting equation 2.9 at different temperatures. The data shows that the spin diffusion length is roughly proportional to the thickness, which is consistent with the expectation [186] that $\lambda \propto \frac{1}{\rho} \propto t$. As the platinum wire is thin, the spin diffusion length will depend on thickness. The magnitude of the spin diffusion length is comparable to published values [6; 94; 187] and is smaller than values found in the bulk [188].
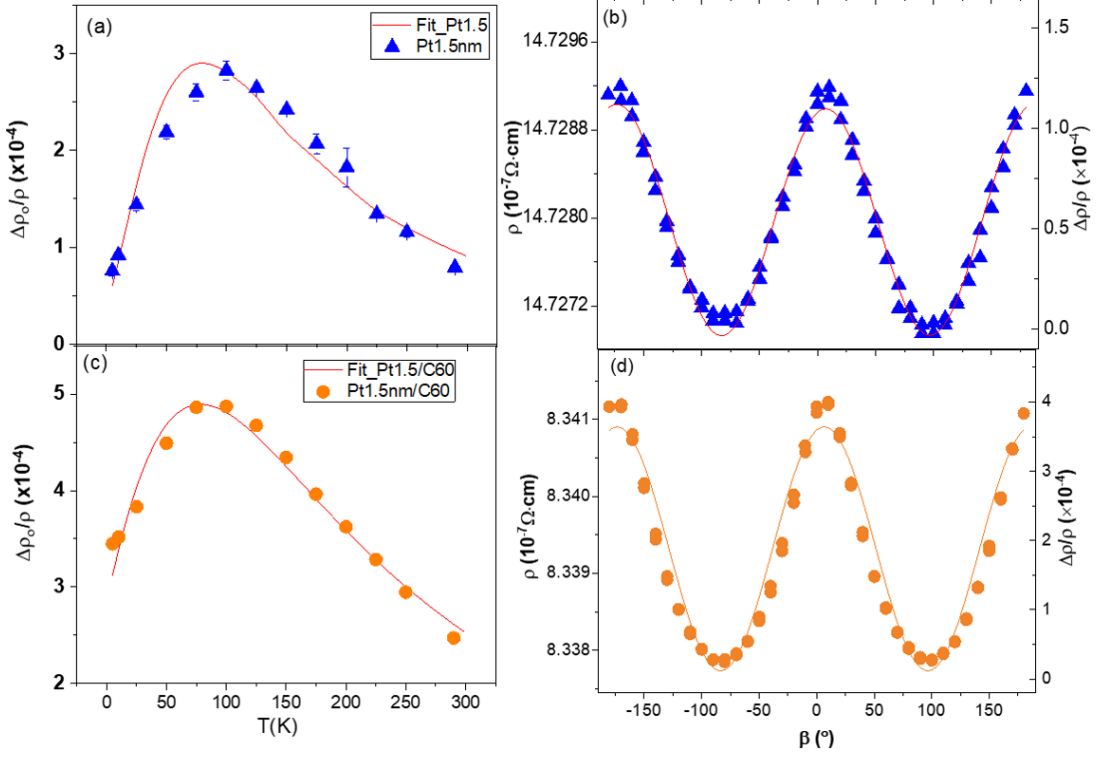
Figure 4.6: (a,c). SHMR for Pt wires 1.5 nm thick with and without C_{60} on GGG/YIG(170nm) measured at different temperatures and fitted to equation 2.9.(b,d). Examples of SHMR fits to $cos(\beta)^2$. Resistivity and magnetoresistance measured at 25 K for Pt wires 1.5 nm thick without (b) and with (d) a 50 nm overlayer, grown on a GGG/YIG(170 nm) substrate. The applied field for these measurements is 0.5 T.

4.2.4 SHMR platinum thickness dependence

Figure 4.9 (a) shows the SHMR measured at 0.5 T. The peak at 75-100 K has been identified as corresponding to the temperature when the spin diffusion length of Pt equals the Pt thickness [78; 91; 93]. However, figure 4.8 demonstrates that the max in the SHMR cannot be due to the spin diffusion length equaling the Pt thickness at that temperature. This peak could be due to the reduction in the magnetization of YIG thin films below 50-150 K, as reported by A. Mitra et al [151]. This magnetization reduction is caused by Gadolinium interdiffu-
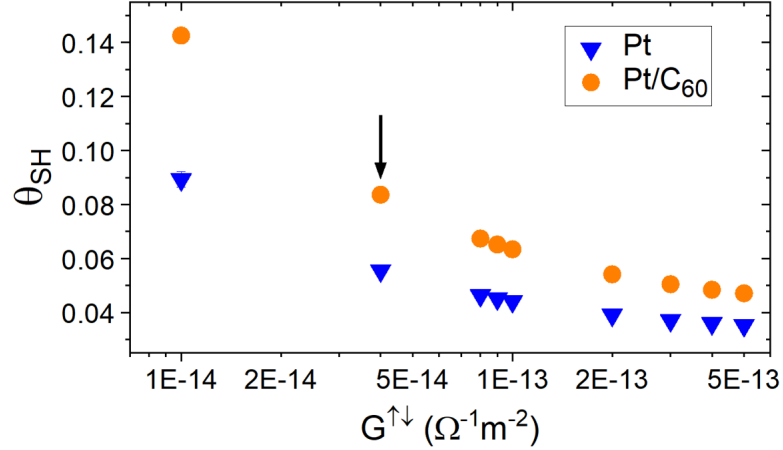
Figure 4.7: Derived spin hall angle from fitting the SHMR vs. T data as a function of the spin mixing conductance ($G_{\uparrow\downarrow}$) value used in the fit. The arrow points to the spin-mixing conductance that we use in the SHMR fit. Note that Θ_{SH} is higher for Pt/C$_{60}$ for all ($G_{\uparrow\downarrow}$) values.

sion during annealing and the emergence of an antiferromagnetic coupling at the GGG/GdIG/YIG interface below those temperatures. Another possibility could be a temperature dependence of the spin diffusion length in terms beyond T^{-1}. However further work would be needed to confirm either hypothesis. For Pt thicker than 2 nm as sowon in Figure 4.9 (a), the SHMR decreases with increasing Pt thickness because when the Pt thickness is bigger than the spin diffusion length, the spin current will have losses from scattering, resulting in a reduction of surface interactions and reducing the magnitude of the inverse spin Hall effect that contributes to the SHMR. The maximum effect of the molecular layer (factor 4 to 7 change) takes place for thin films (1.5 nm) at low temperatures, or thick films (5 nm) at room temperature as shown in figure 4.9 (b). For the thinnest measured films of 1.5 nm, the conducting layer at the interface adds an effective thickness to the Pt.
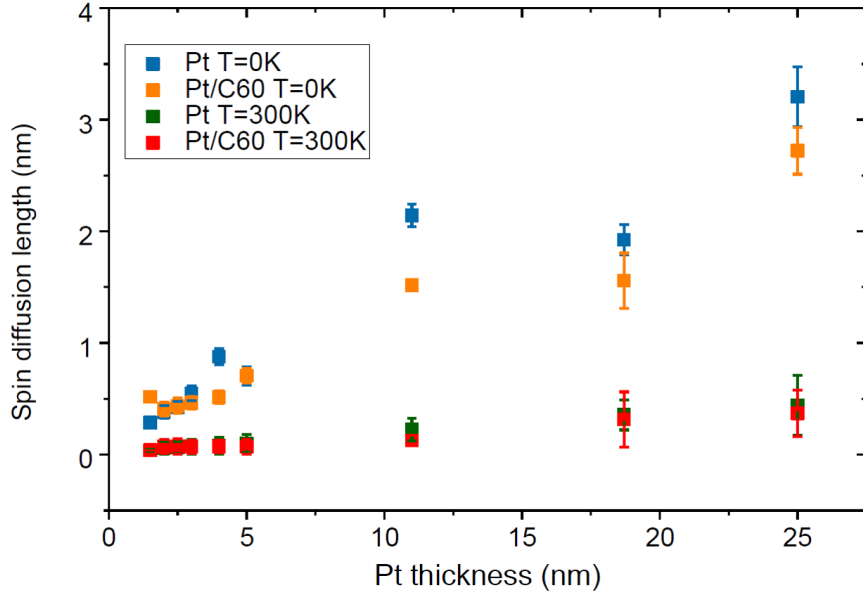
Figure 4.8: Derived spin diffusion length at room temperature and 0 K from fitting the SHMR results for Pt and Pt/C$_{60}$. The spin diffusion length is generally proportional to the thickness, according to the data.

By fitting the SHMR data in figure 4.10, we can extract the spin Hall angle Θ_{SH} which, for wires $\leqslant 5$ nm is significantly higher with the molecular overlayer. This effect disappears for thick wires ($\geqslant 11$ nm), where we hypothesize that the molecular interface does not significantly change the effective SOC.
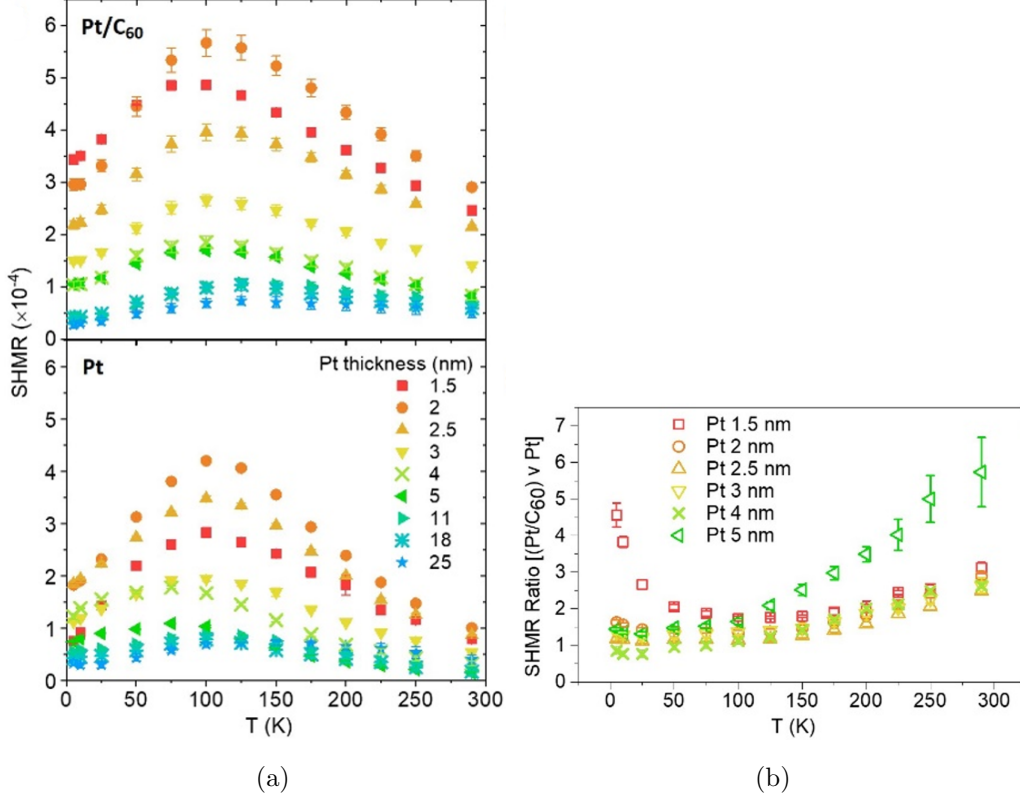
Figure 4.9: (a) SHMR for Pt and equivalent Pt/C_{60} wires of different thicknesses on GGG/YIG(170 nm) films. The SHMR is higher in Pt/C_{60} for almost all temperatures and thicknesses. (b) SHMR Ratios between Pt/C_{60} and Pt wires.

Figure 4.11 (a) shows the position in temperature of the maximum of the SHMR for the measured Pt wire thicknesses. Although this maximum is sometimes attributed to the temperature point at which the spin diffusion length matches the film thickness, these results indicate something different, as the dependence of the peak position with Pt thickness is weak and, for Pt/C_{60}, goes to lower temperatures as the film thickness is reduced. In figure 4.11 (b) the maximum SHMR measured (at different temperatures) as a function of the Pt thickness for both pure metal and Pt covered on molecules. Figure 4.12 shows the degree of sample-to-sample repeatability that can be quantified by measuring a repeat sample.
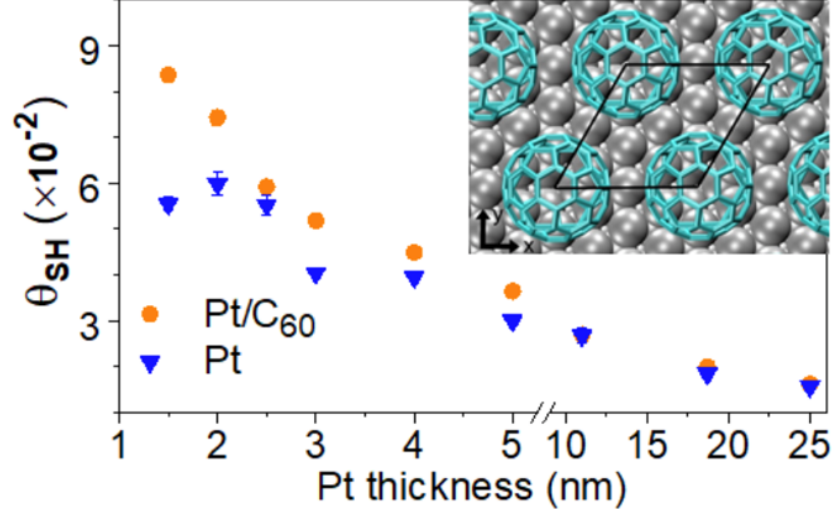
(a)

Figure 4.10: For 5 nm thick wires or less, the Θ_{SH} obtained from the SHMR data fits is significantly higher with the molecular overlayer. Inset: Top view of the optimized C_{60}/Pt(111)-($2\sqrt{3}$x$2\sqrt{3}$)R30 interface DFT model. The C_{60} molecules are adsorbed on top of one Pt-vacancy. The black polygon marks the in-plane periodicity of the system. Pt: silver, C: cyan. Courtesy of Dr. G. Teobaldi.

4.2.5 Low Field AMR in Pt

For Pt grown on YIG, an additional change in resistance is observed at low magnetic fields $< 5 - 20$ mT when the direction of an applied magnetic field is changed with respect to the electrical current, see figure 4.13 (a,b). The origin of this AMR is controversial. It has been attributed to a proximity-induced magnetization of Pt, which is close to the Stoner criterion [24]. The boundary effects in thin film are significant, thereby leading to a magnetic interaction between nearest neighbouring atoms at the interface. In YIG/Pt interface, XMCD provides an average Pt moment of 0.054 μ_B at 300 K [24]. However, it is also claimed that there is no evidence for this induced magnetization [25]. In this case, the XMCD signal shows no obvious proof for induced magnetic moments, and it is 30 times smaller compare with Pt/Fe reference sample. This low field AMR (LF-AMR) is characterized by the presence of peaks, positive or negative depending on the

(a)   (b)
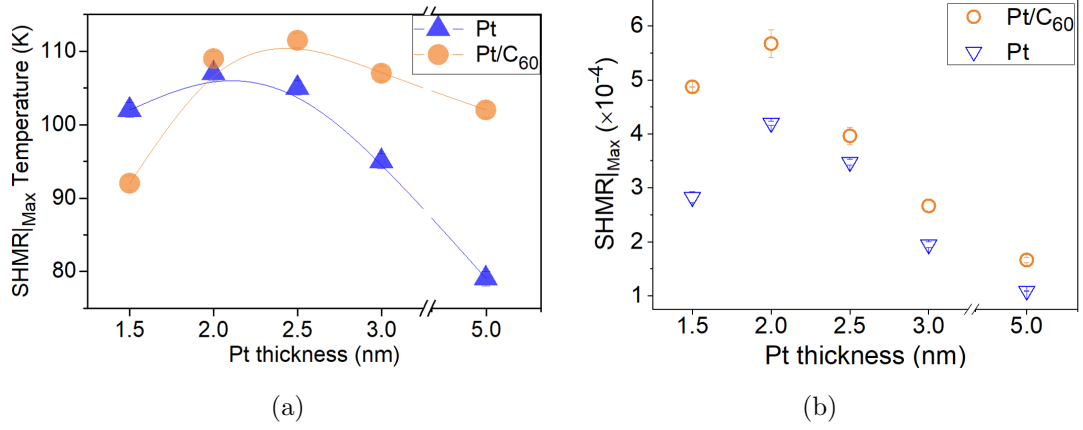
Figure 4.11:   a. The SHMR peaks in correlation with spin diffusion length of Pt. Lines are a guide to the eye. b. Maximum SHMR measured in Pt and Pt/C_{60}, not necessarily at the same temperature.
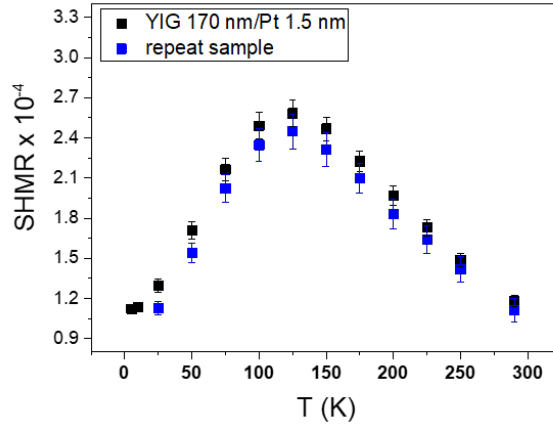
Figure 4.12: SHMR for Pt wires 1.5 nm thick on GGG/YIG(170 nm) measured at different temperatures. The measurement of a repeat sample demonstrates quantitatively the degree of sample-to-sample reproducibility.

field direction, resembling the AMR observed in magnetic films with domain wall scattering [189; 190]. Due to SOC, in most magnetic materials domain walls reduce the resistance for in-plane fields, and increase it for out of plane fields. This

domain wall AMR peaks at the coercive field H_c of the magnet, for the greatest magnetic disorder and domain wall density. In YIG/Pt, the position of out-of-plane LF-AMR peaks coincides with the coercivity of the perpendicular minor YIG loops in figure 4.13 (c), which could point to a YIG surface layer with an out-of-plane easy axis. We find that the LF-AMR has the same shape and peak position with or without a molecular overlayer. This means that the LF-AMR has the same coercivity with or without a molecular overlayer, indicating the same micromagnetic configurations of domain walls. However, the magnitude of the LF-AMR is larger when C_{60} is present, which could be due to an enhanced SOC/anisotropy and/or acquired moment. This molecular effect is stronger for the perpendicular configuration see figure 4.13 (b), which may be due a larger perpendicular magnetic anisotropy induced by C_{60}, as reported for Co [138].
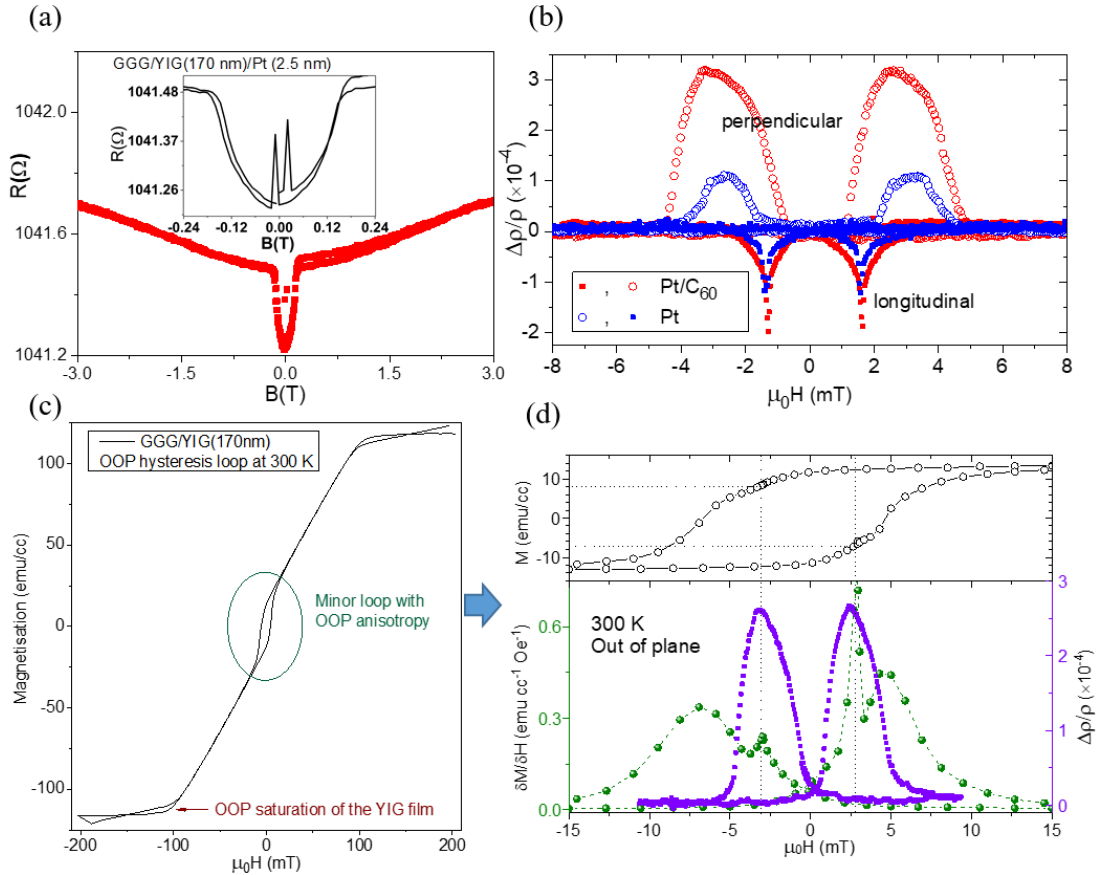
Figure 4.13: (a). LF-AMR peak (see inset) is observed at around a few mT, which corresponds to the magnetization of the surface of the YIG. (b) Room temperature LF-AMR comparison between YIG/Pt and YIG/Pt/C_{60}. The curves are qualitatively the same, but the magnitude of the effect is enhanced by the molecules. (c) Unformatted, out-of-plane hysteresis loop measured at room temperature for a GGG/YIG(170nm) film. (d), top: Corrected and magnified minor loop. (d), bottom: Differential of the magnetization in the minor loop and magnetoresistance.

The position of the OOP LF-AMR peaks coincides with H_c as measured in a minor YIG loop. This supports the notion that the rotation of magnetic domains in YIG is connected to the AMR measured in Pt. The out of plane minor loop represents 10% of the total magnetisation of the YIG film (13 emu/cc), see Figure 4.13 (d). Approximately half of the magnetisation are switched at 3 mT and the rest at 7 mT. We attribute this minor loop to the YIG surface magnetization. Note the linear slope dominating the magnetization, due to the in-plane anisotropy of the majority of the film. The differential of the magnetization of the minor loop is showing two peaks that we attribute to the coercivity of two different regions. The local peak in the differential of the magnetisation at 3 mT, which we assign to the coercive field of the YIG film surface, matches the position of AMR maximum for the OOP configuration. In the case of the field in the longitudinal orientation, the low field AMR and hysteresis loop are presented in figure 4.14 (a). The attribution of the AMR peaks to the coercivity of the top YIG layers is more difficult in this configuration, as the YIG surface has an OOP anisotropy and therefore the magnetization changes linearly with in-plane fields. However, we can see that the position of the peaks matches the point at which the magnetization value is ~ 10 % from saturation, as it was the case for the perpendicular minor loop and the out of plane LF-AMR.
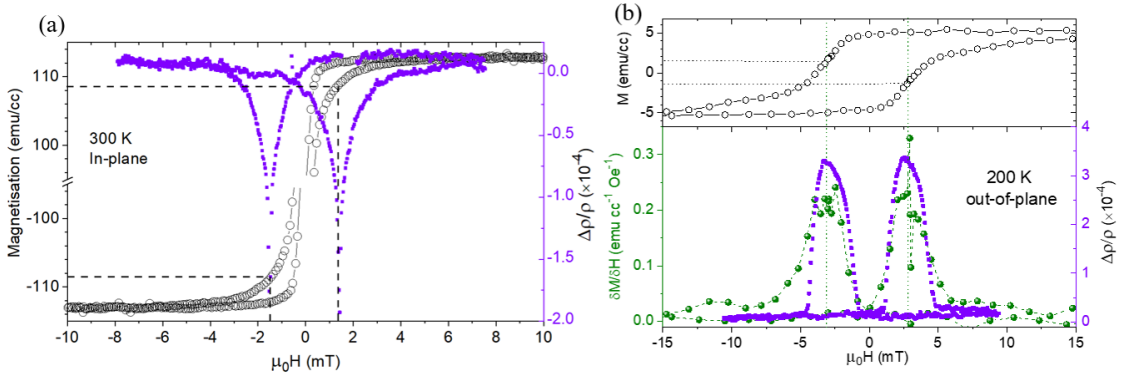
Figure 4.14: (a). Correlation between the in-plane, longitudinal hysteresis loop and the LF-AMR for the Pt/C_{60} sample of figure 4.13. (b). LF-AMR and minor hysteresis loop with the field in the perpendicular orientation at 200 K.

4.3   YIG sample characterisation

The fabrication of YIG films can lead to elemental diffusion and defects that change the magnetic properties of the ferrimagnet and the interpretation of transport measurements [151]. Arpita Mitra, et al. show interdiffusion at the YIG/GGG interface where Gd from the GGG and Y from the YIG diffuse. Also, their results indicate the diffusion of Gd and Ga at the interface forming Gd and Ga-mixed YIG region, which can affect the magnetic properties of YIG near the interface. Figure 4.15 shows atomic-resolution aberration corrected, cross-sectional scanning transmission electron microscopy (STEM) images, and electron energy loss spectroscopy (EELS) chemical maps, courtesy of Prof. Quentin Ramasse at superSTEM. It is possible to observe, in addition to a certain level of surface roughness of the YIG film, an area close to the YIG surface and below the sputtered Pt wire into which some Pt metal may have diffused and formed a low density of nm-sized clusters. This diffusion can affect the magnetization and anisotropy direction at the surface of the YIG layer, originating the minor loops we observe in the perpendicular field direction in some YIG films [18; 151].
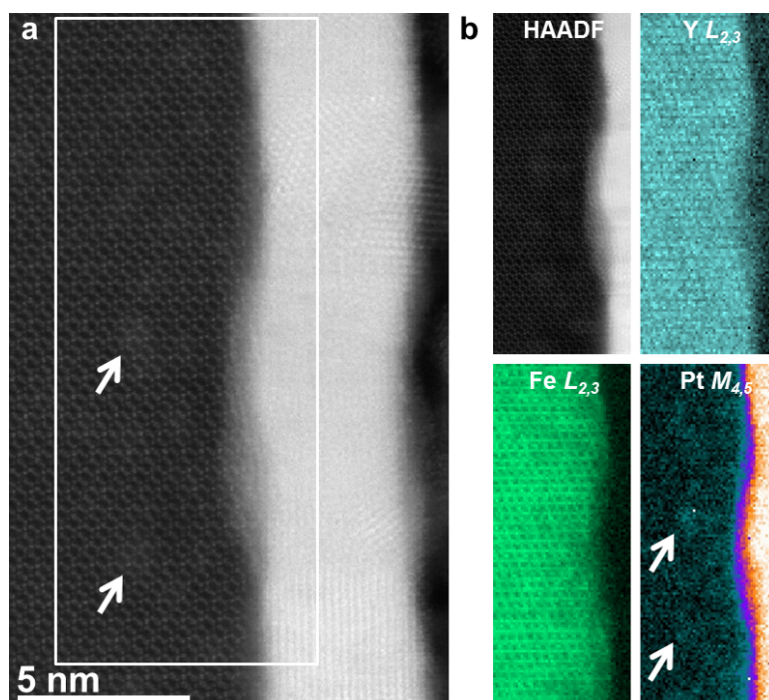
Figure 4.15: (a) Cross-sectional high angle annular dark field (HAADF) image of the YIG/Pt interface obtained using a scanning transmission electron microscope. (b) Elemental chemical analysis of the interface using EELS: the relative intensity maps of the Y, Fe and Pt ionization edges are presented with a simultaneously acquired HAADF image of the region, indicated by a white box in (a). Bright clusters immediately below the YIG surface, indicated by white arrows in the Pt map and the overview HAADF image, contain a higher Pt concentration and may be due to Pt diffusion into the YIG. Taken from [151].

71

The LF-AMR peak position in field (coercivity of the YIG surface) and peak width (saturation field of the YIG surface), increase as the temperature is lowered (Figs. 4.16 a-b). Typically, the AMR of YIG/Pt measured at high fields is reported to vanish above 100-150 K [103]. If measuring at 3 T, where quantum localisation and other effects are strong, we observe this same decay with temperature. However, the LF-AMR can be observed up to room temperature. C_{60} not only increases the LF-AMR value, but it also makes it less temperature dependent, so that the LF-AMR ratio can be up to 700 % higher for Pt/C_{60} at 290 K (Fig. 4.16 c). This supports our suggestion from DFT simulations (in section 4.3.2) of a mechanism based on C_{60} induced re-hybridization enhancing the magnetic moment acquired by transport electrons via SOC. The LF-AMR depends on the Pt thickness, t, as $(t - x)^{-1}$ (Fig. 4.16 d). We identify the value of x, approximately 1 nm, as the magnetised Pt region contributing to the AMR. This relationship is not affected by the C_{60} layer, although the magnitude is uniformly higher with molecules.
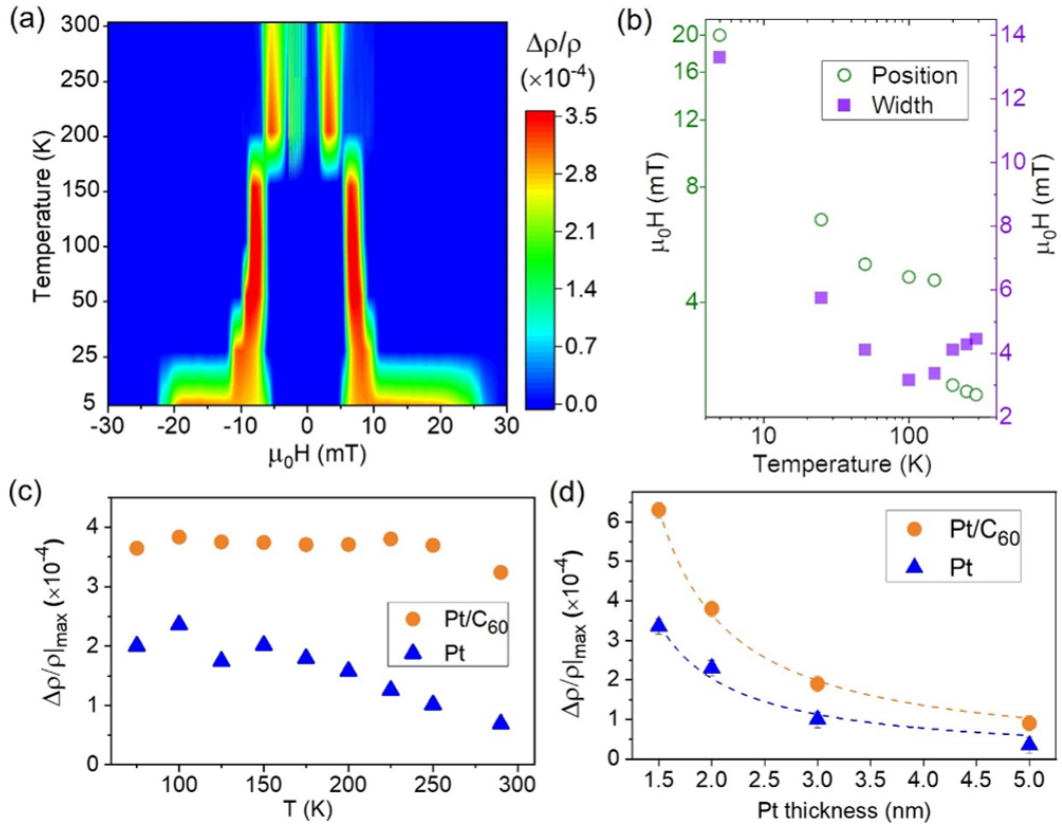
Figure 4.16: (a) Perpendicular LF-AMR for GGG/YIG(170)/Pt(2)/C$_{60}$(50). (b) The perpendicular LF-AMR peak position and width are increased in steps as the temperature is reduced. (c) Temperature dependence of the maximum LF-AMR, calculated as the change in resistance from the peak in the perpendicular orientation to the minima in the longitudinal. There is a faster temperature drop in the MR values for Pt when compared with Pt/C$_{60}$. This may be due to the acquired magnetic moment in Pt/C$_{60}$ leading to a more stable induced magnetisation up to higher temperatures. (d) The LF-AMR for Pt and Pt/C$_{60}$ fits to a $(t - x)^{-1}$ function with respect to the Pt wire thickness.

4.3.1   AMR at low fields: YIG on YAG

We have used SQUID measurements to study the temperature and thickness-dependent magnetic properties of YIG on GGG and YAG substrates. All hysteresis loops for YIG on GGG in this report show the signal after subtracting the large background signal generated by the paramagnetism from Gd_{3+} ions in the GGG substrate. There was no paramagnetic background signal observed on YAG, making this a preferred option for low temperature magnetometry measurements, where background signals become harder to extract. This is the case in particular for OOP measurements, where the YIG magnetic moment is mostly linear with field and difficult to differentiate from the paramagnetic signal of the substrate even at relatively high temperatures. On GGG, M_s is found to be 64 emu/cc, which is 32 % lower than the values previously measured by Mitra et al. in RF sputtered YIG on GGG for an equivalently thick film (40 nm) [151]. The reduction of Ms in our sample is likely to be due to the deposition of the Pt and metal interdiffusion. Also, it has been reported that the magnetization M_s of the YIG films is significantly reduced by a cap Pt layer [191].

On a YAG substrate, the M_s is found to be 41 emu/cc as shown in figure 4.17. This is much smaller (44 %) for the YAG substrate than for samples grown on GGG. This is comparable to be consistent with previous films grown by the same method in our group [2]. A possible reason is that YIG is not lattice-matched to YAG, and the films grown on this substrate have much poorer crystallinity, smaller grain size and are rougher. The coercivity of the YIG/YAG is high which is about 25 times higher than on GGG substrate.

As shown in figure 4.18, the peaks in the LF-AMR follow the surface magnetisation. The same effect can be found in YAG substrates, and even though the coercivity is 1-2 orders of magnitude higher for YAG/YIG. Thus, the LF-AMR YIG on YAG peaks appear at 90 % higher fields than GGG, supporting the correlation between the AMR in Pt and the surface YIG magnetisation. The LF-AMR with perpendicular field for YAG/YIG is shown in figure 4.19. It is not possible to do these measurements in the perpendicular direction for GGG/YIG films at low temperatures due to the paramagnetic susceptibility of the much thicker
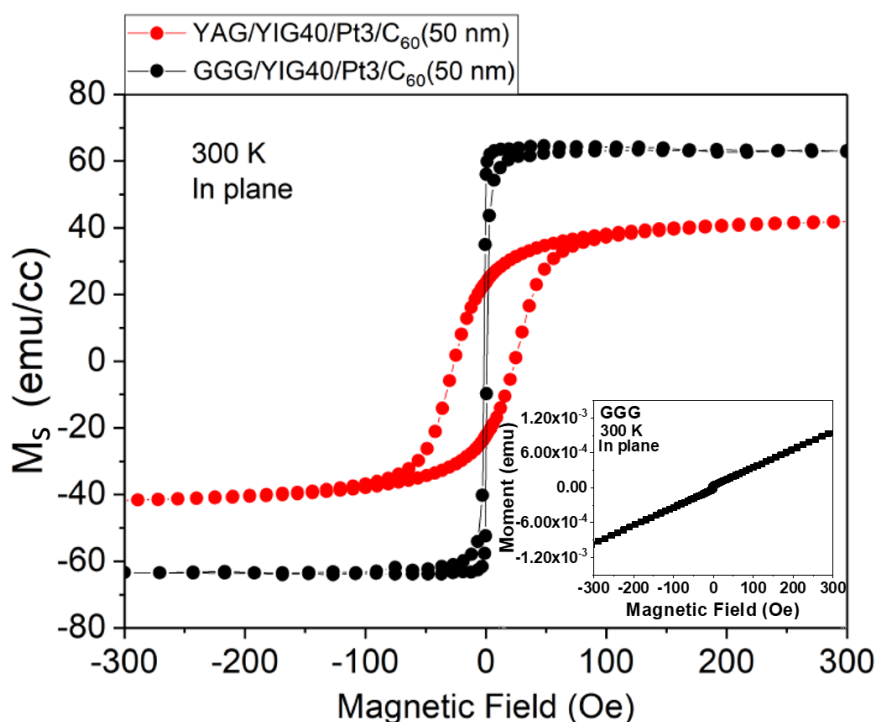
Figure 4.17: Hysteresis loops in the plane for 40 nm thick YIG film deposited on GGG (black curve) and YAG (red curve) at 300 K. Inset shows the magnetic moment as a function of applied magnetic field before the subtraction of the paramagnetic contribution from the GGG substrate.

substrate. The correspondence of the susceptibility and LF-AMR peaks in the perpendicular orientation is maintained for all temperatures. Polynomial contributions to the susceptibility have been removed. The large increase in coercivity results in more spread peaks at higher fields.

4.3.2 The enhancement of SOC with a C_{60} capping layer

We have investigated the enhancement of SOC in Pt correlated with the increase in spin Hall angle as determined from SHMR measurements. It is possible that the larger SHMR observed in metallo-molecular wires could be due to a change
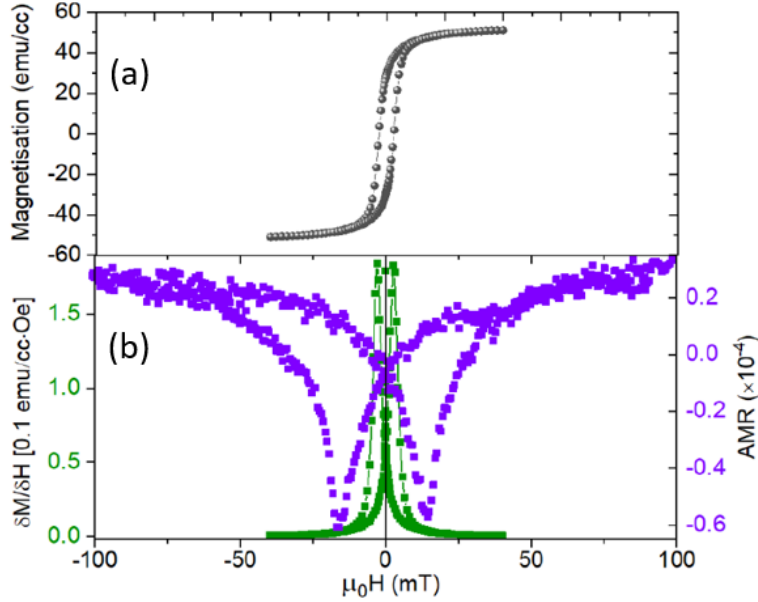
Figure 4.18: (a) YAG/YIG(40nm)/Pt(3nm)/C$_{60}$ magnetization of hysteresis loop measured in an in plane direction at room temperature by SQUID. (b) Correlation between the differential of the magnetization in-plane and longitudinal LF-AMR for the same sample.

in the spin mixing conductance ($G_{\uparrow\downarrow}$) induced by C$_{60}$ [5; 192]. However, $G_{\uparrow\downarrow}$ is related to the spin transparency of the YIG/Pt interface, where the effect of the molecular interface should be negligible [18]. If the C$_{60}$ was inducing changes to the spin mixing conductance, we would expect the effect of C$_{60}$ in the SHMR to be inversely proportional to the Pt thickness, which is not the case. When discussing an interfacial effect, in this instance we referred to the Pt-C$_{60}$ interface and the fact that, as it would be expected that bigger changes are observed in the SHMR and AMR of thinner Pt wires ($<$ 2.5 nm), whereas for thick wires ($>$ 15 nm) the effect of the C$_{60}$ overlayer is small or negligible.

As shown in figure 4.20, the SHMR vs T data cannot be fitted as a change in the spin-mixing conductance whilst keeping the spin Hall angle constant between Pt and Pt/C$_{60}$. These spin mixing conductance values are between 1×10^{13} $\Omega^{-1}m^{-2}$ and 1×10^{15} $\Omega^{-1}m^{-2}$. However, doing the opposite, allowing a
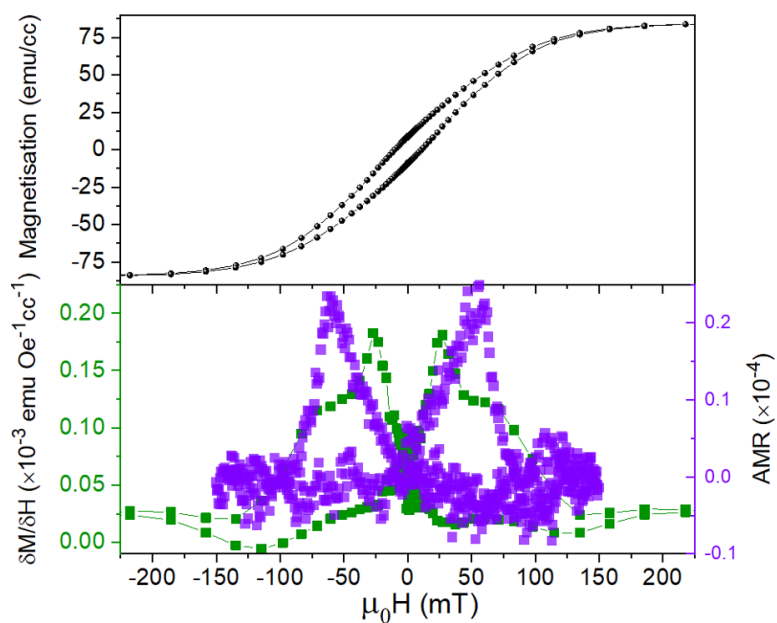
Figure 4.19:   LF-AMR for a YAG/YIG(40nm)/Pt(3nm)/C_{60} sample measured at 10 K with an out of plane, perpendicular field. The figure shows the correlation between the magnetization and LF-AMR.

change in the spin Hall angle between Pt and Pt/C_{60} whilst keeping the same spin-mixing conductance, works well for all datasets.
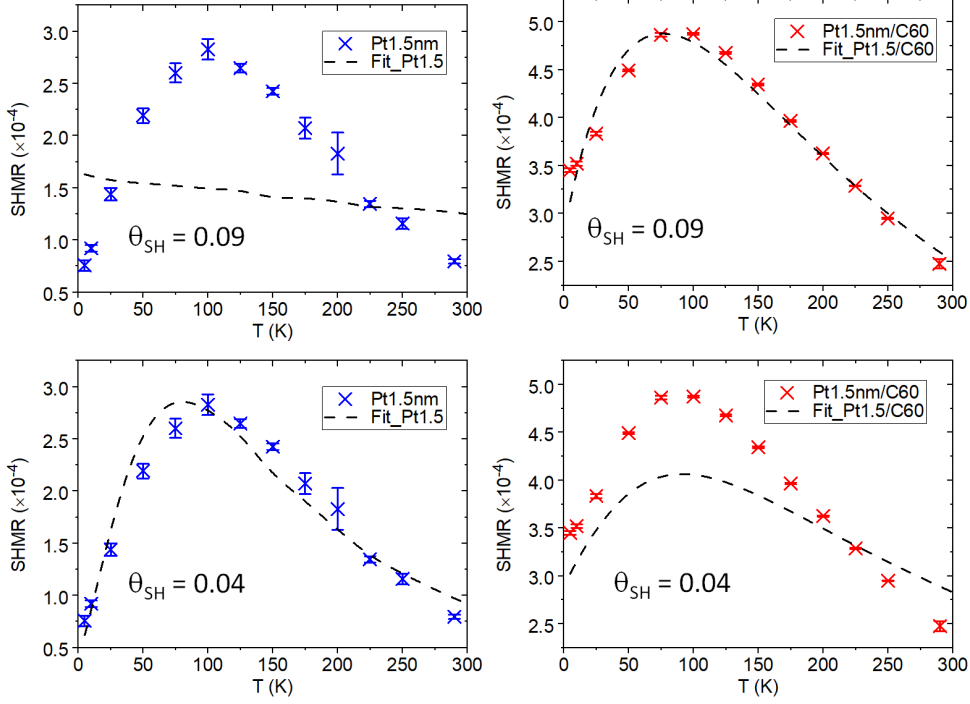
Figure 4.20: Curves where we fix the Θ_{SH} and allow the spin mixing conductance to change by up to two orders of magnitude cannot fit simultaneously the results for both Pt and Pt/C$_{60}$. The value used in this fit is $4 \times 10^{14} \Omega^{-1} m^{-2}$ [6]. We can therefore conclude that the Θ_{SH} has changed.

Furthermore, no increase in ferromagnetic resonant damping proportional to $G_{\uparrow\downarrow}$ of YIG/Pt with C$_{60}$ interfaces was observed (See Fig. 4.21) [18; 193]. We have done the design and the samples fabricate but the measurements have been done in University of Cambridge with by Chiara group. FMR results show that the damping in the ferromagnetic resonance of YIG with Pt is not affected by the presence of the C$_{60}$. This is not consistent with a change in spin-mixing conductance, as the damping should increase in that case. This further confirms that changes to the effective SOC are the most likely explanation to the enhanced SHMR.
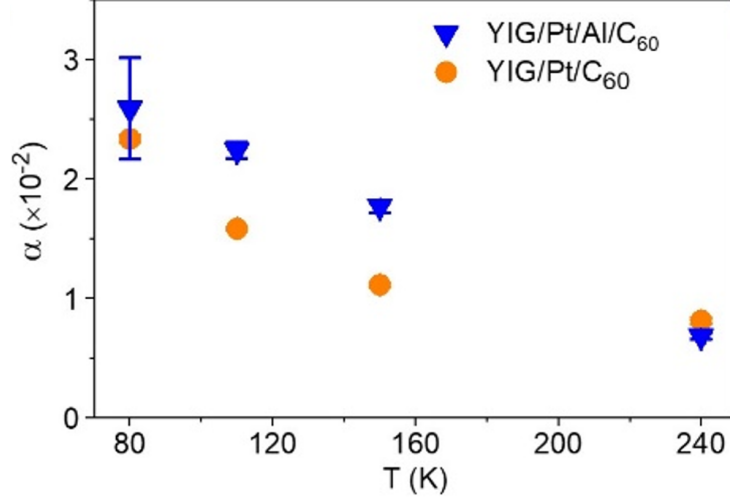
Figure 4.21: FMR damping in YIG(40 nm)/Pt(2.5 nm)/Al(5 nm)/C_{60}(50 nm) and YIG(40 nm)/Pt(2.5 nm)/C_{60}(50 nm) samples. An Al layer is added to decouple the Pt and fullerenes in the control sample, rather than removing the C_{60}. This is to have the same layer (C_{60}(50)) in contact with the microwave waveguide, avoiding impedance coupling changes. Both metallo-molecular bilayers were grown on the same GGG/YIG(40) sample, previously diced. The relatively high damping is due to the small thickness of the YIG layer, used to maximise the effect of the Pt layer. The damping, proportional to the spin mixing conductance, is not increased by the presence of the molecular interface. FMR measurements courtesy of Dr. Chiara Ciccarelli and James Pratchett at Cambridge University.

Changes to the spin-mixing conductance would not result in an enhanced AMR of the Pt wire, whereas an enhancement in the effective SOC would result in the observed increased low field AMR. The AMR is dependent on the anisotropy and therefore on the SOC, not the spin mixing conductance or other mechanisms. In many studies, the AMR has been indicated a SOC at an interface [194]. In our AMR results a large contribution of strong SOC is enhanced by up to 700% with the molecular interface, so by itself the LF-AMR could be enough to support our hypothesis of enhanced SOC. Thus, as a whole (SHMR, AMR, FMR and DFT), our results are more consistent with a change in the effective SOC and magnetic moment acquired by the transport electrons mediated by the introduction of C_{60}.

Non-collinear band structure calculations enable analysis of the atom Projected (energy-dependent) Magnetization Density (PMD) for different Pt and Pt/C_{60} film thicknesses. The PMD is therefore correlated with the magnitude of spin-dependent scattering effects and what we term the effective SOC. In all cases, the simulations carried out by Dr. Teobaldi and colleagues find the PMD for the in-plane (x,y) magnetic moment components (mx,y) to be larger than for the out of plane one (mz). It is also possible to observe an enhancement of the PMD oscillation magnitudes due to the adsorption of C_{60}. The effect becomes smaller as the Pt thickness increases from 1.1 nm to 2.5 nm and 3.9 nm, correlated with the SHMR values in Pt/C_{60} (Fig. 4.22). The differences in PMD between the C_{60}/Pt and Pt systems document the role of the Pt/C_{60} interfacial re-hybridization, and ensuing changes in the electronic structure, for enhancing SOC-related anisotropies and spin transport in Pt-based systems. The DFT simulations show that C_{60} brings a significant increase in the effective SOC and ensuing in-plane magnetization acquired by the electrons flowing in the current, consistent with our experimental results.
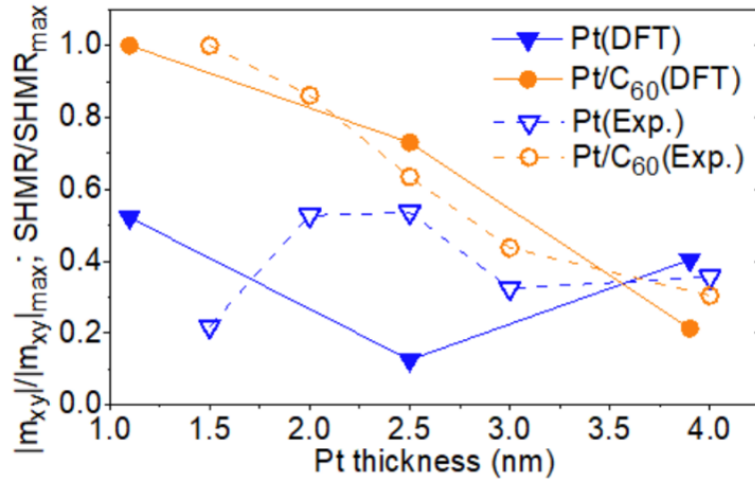
Figure 4.22: DFT simulations of the in-plane magnetic moments and experimental SHMR, normalized to the largest calculated ($|mxy|$) or measured value (SHMR) as a function of the Pt thickness.

4.4 Annealing effects on platinum

4.4.1 Annealing effects on Pt by TEM

YIG(40 nm)/Pt(2nm)/C_{60}(50nm)/Al(2nm) samples annealed at 250 °C were imaged using TEM. This method is utilised to characterise the interfaces further and offer information on inter-diffusion, uniformity and crystallinity after annealing. A cross-sectional TEM image of the annealed Pt wire is shown in figure 4.23. Here, there is a lot of Pt (3-5 nm) diffusion layer into the YIG.
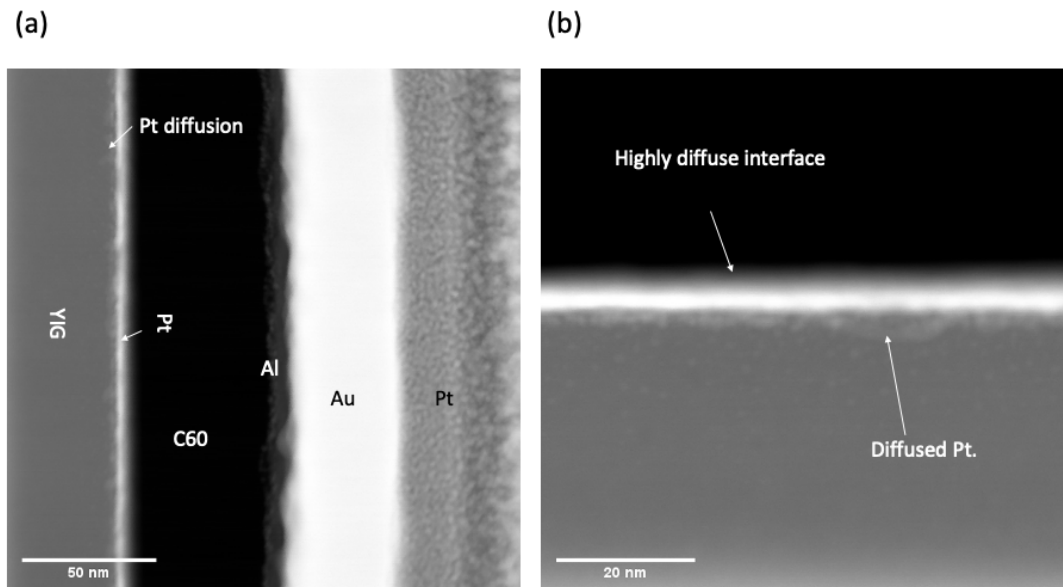
Figure 4.23: (a,b) Cross-sectional transmission electron microscope image of the annealed Pt wire on a YIG substrate. (b) There is a clear diffusion layer of Pt into the YIG.

4.4.2 Annealing effects on Pt resistivity

The resistivity as a function of annealing temperature for Pt and Pt/C_{60} on a YIG/GGG substrate is shown in 4.24 (a). Some of Pt goes into the YIG which increase the resistivity in both Pt and Pt/C_{60} but in Pt/C_{60} the interface is improved so more conductance at Pt/C_{60} interface. The typical form of the annealed platinum resistivity describes ρ vs T for metals, which is consistent with earlier experimental results. As discussed in the beginning of the chapter the resistivity for Pt with C_{60} is lower than for bare Pt wires due to charge transfer and orbital re-hybridisation, contributing to the conductivity. After annealing, the effect of C_{60} on the resistivity of Pt wires is further enhanced. As a result, annealing reduces dimensional effects in Pt/C_{60}, such as weak localization, which has a smaller effect in Pt/C_{60} wire than in Pt wire. Also after annealing, the resistivity of Pt/C_{60} decreases by about 30 % compare to unannealed Pt/C_{60}.

Figure 4.24 (b) shows the RRR for annealing Pt and Pt/C_{60} at different Pt thickness. The grain size will increase as the crystallinity improves (see TEM 4.23), and that will reduce scattering at grain boundaries, a term in the resistivity that does not depend on temperature. Furthermore, C_{60} will also form a better crystal structure after annealing, which will improve the hybridisation (more carbon atoms close to Pt) and improve the conductivity of the hybrid interface. The resistivity of annealed Pt wires as a function of metal thickness is shown in figure 4.24 (c). The annealing shows the same pattern for the Pt resistivity as function of sample thickness which is decreasing.
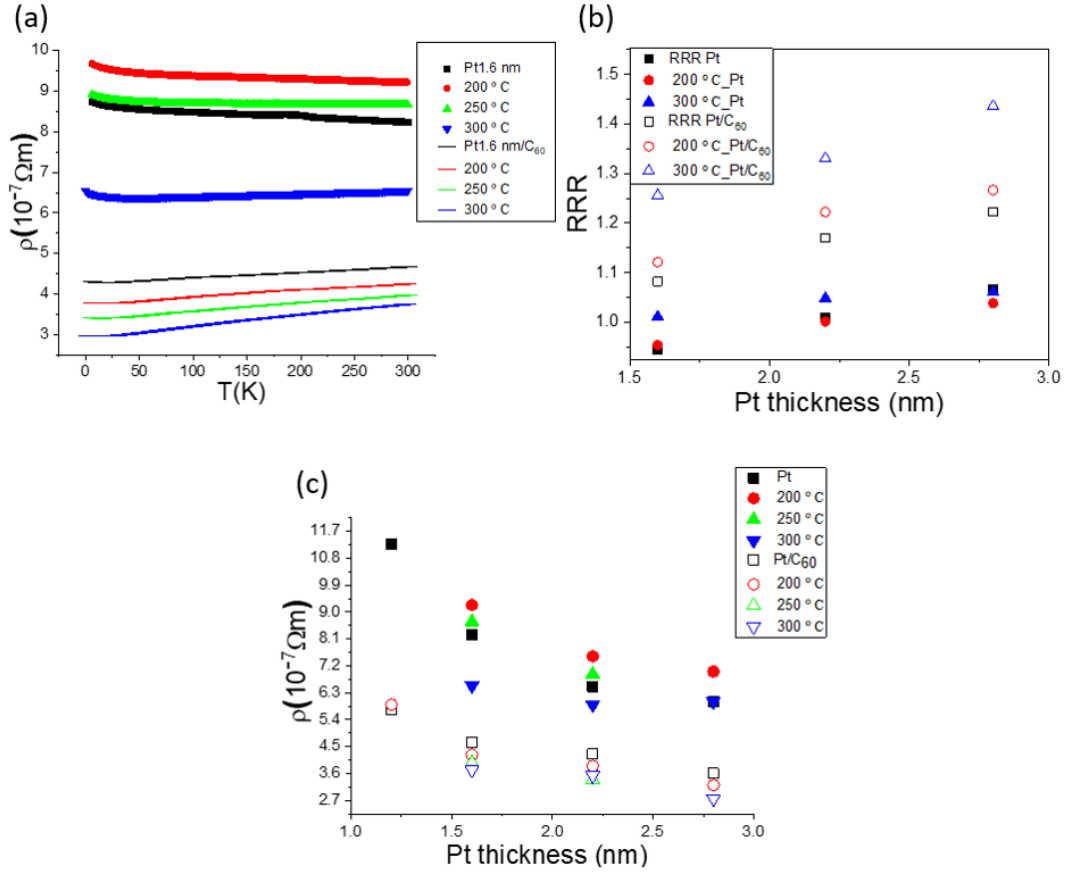
Figure 4.24: (a) The resistivity of Pt is increased after annealing, while with C_{60}, the resistivity is deceased. (b) In comparison to annealing, the additional conducting hybrid interface reduces boundary scattering and raises RRR. (c) As the sample thickness decreases, the annealing Pt resistivity follows the expected pattern for an NM.

4.4.3 Annealing effects on Pt SHMR

Figure 4.25 shows the SHMR (β angle) measured at 0.5 T before and after annealing at different temperatures. Annealing made the Pt wire have higher SHMR than Pt/C_{60}. The temperature at which the spin diffusion length of Pt equals the thickness of Pt, frequently thought to be the SHMR peak temperature, is 75-100 K. However, for annealed Pt the SHMR maximum occurs at a lower temperature

than unannealed Pt. As a result of the annealing, the spin diffusion length dependence on temperature was changed. When we have better crystallinity, the spin diffusion length is found to be longer and the peak moves to lower temperature [92]. This is ascribed to a smaller temperature dependence of the spin diffusion length , which could be due to a different resistivity of Pt. Furthermore, as demonstrated in figure 4.25, the higher annealing temperature, the more the SHMR of plain Pt increases at low temperatures.
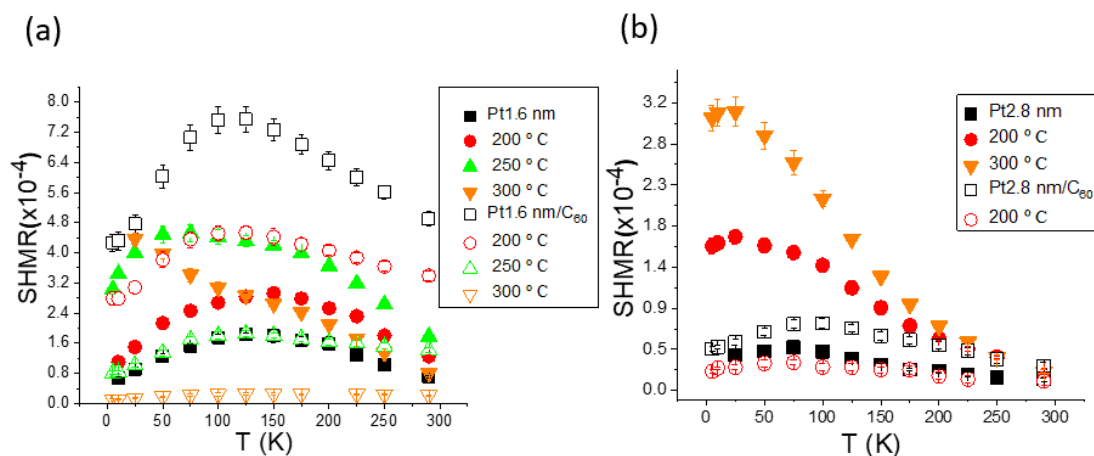
Figure 4.25:   (a) and (b) are SHMR for annealed Pt 1.6 nm and Pt 2.8 nm respectively. The SHMR is reduced in Pt/C_{60} respect to annealing at 200-300 °C. The annealed Pt SHMR peaks at lower temperature (around 25 K) while unannealed Pt SHMR maximum occurs around 75 K.

The SHMR of plain Pt increases after annealing, but since the SHMR is dependent on resistivity, it is possible that this is due to the higher resistance and thinner Pt wire when Pt partly moves away from the wire. For Pt/C_{60}, there is also loose Pt, but the improved conductivity of the interfacial C_{60} layer reduces the resistivity. This layer does not contribute to the SHMR directly because its SOC is very low (it just enhances the SOC in the Pt), which would explain why the SHMR is lower for Pt/C_{60} after annealing: the hybrid layer contributes to the conductivity far more.

4.4.4 Emergence of a uniaxial OOP anisotropy after annealing

When measuring the SHMR out of plane at low temperatures in annealed Pt wires, we note that the MR signal is not symmetric with the applied magnetic field. The data that appears in figure 4.26 (a, b) shows when sample (Pt 2.8 nm) rotates from perpendicular to transverse (β angle). In (a) Low MR at zero degrees in a positive field (+ 0.5 T) shows the same asymmetric field dependence as measurements with the sample at 180 degrees in negative field (- 0.5 T). In (b) the same sample (Pt 2.8 nm) has been measured at a higher field (3 T) where the asymmetry is greatly reduced or disappears, which we assume is because the high field is able to overcome the out of plane uniaxial anisotropy. Figure 4.26 (c, d) represents thinner Pt 1.6 nm, which has an opposite anisotropy to Pt 2.8 nm. At zero degree, the sample is out of plane. At positive field, the resistance of Pt 2.8 nm is higher at zero degree and the resistance is lower at 180 degree. In this case, there is out of plane an uniaxial anisotropy effect in YIG or YIG/Pt. The effect is not dependent on the sign of the current as shown in figure 4.26 (e). Reversing the current does not show opposite voltage. Thus, a Hall voltage effect is excluded. Also, in figure 4.26 (f) the low AMR at 5 K shows a significant shift in the positive magnetic field region.

According to previous findings [44; 151], gadolinium diffusing from the GGG substrate into the YIG during the crystallization annealing process generates a dead layer. The magnetic properties of YIG are affected by the dead layer, in particular at low temperatures. This Gd diffused layer (gadolinium iron gallium layer or GdIG) is magnetically dead above ~100 K and antiferromagnetically coupled to the YIG film below that temperature [151]. Therefore, if the GdIG layer generates an OOP exchange bias at the origin of the uniaxial anisotropy, we would expect that field cooling from above 100 K should invert the anisotropy, and there should not be any anisotropy above ~100 K. However, even from room temperature, field cooling does not invert the anisotropy. As a result, the Néel temperature for this antiferromagnetic layer is expected to be higher than room temperature. Another reason why Gd diffused layer is unlikly is that the

anisotropy is out of plane, whereas Gd diffused layer is most likely in plane [151]. Furthermore, annealing at 200-300 °C is unlikely to cause any change to the Gd diffusion, given that the YIG film had already been annealed at 850 °C and these high temperatures are required both to form a good crystalline YIG film and to observe Gd diffusion from the substrate.

Another possibility is Pt diffusion during annealing in the YIG layer, forming a different AFM coupling. As previously demonstrated in the TEM image shown in figure 4.23, Pt diffuses into the YIG, in particular after annealing (the previous TEMs before annealing also seem to show some Pt inclusions in YIG -as per our paper). There is no reason for the out of plane AMR in YIG/Pt to saturate at low fields unless the interface is behaving differently from bulk YIG. We already showed in the hysteresis loop in figure 4.13 that the magnetic anisotropy for the surface of Pt/YIG might be out of plane, so that could be the original for the uniaxial anisotropy. We suggest that this Pt-YIG mixed top layer might be responsible as well for the out of plane uniaxial anisotropy. We do not observe a uniaxial anisotropy at room temperature, so this is a weakly magnetic layer at room temperature, but it is more strongly coupled at low temperatures. The only way to really check would be with magnetometry, but OOP measurements of GGG/YIG are not possible.
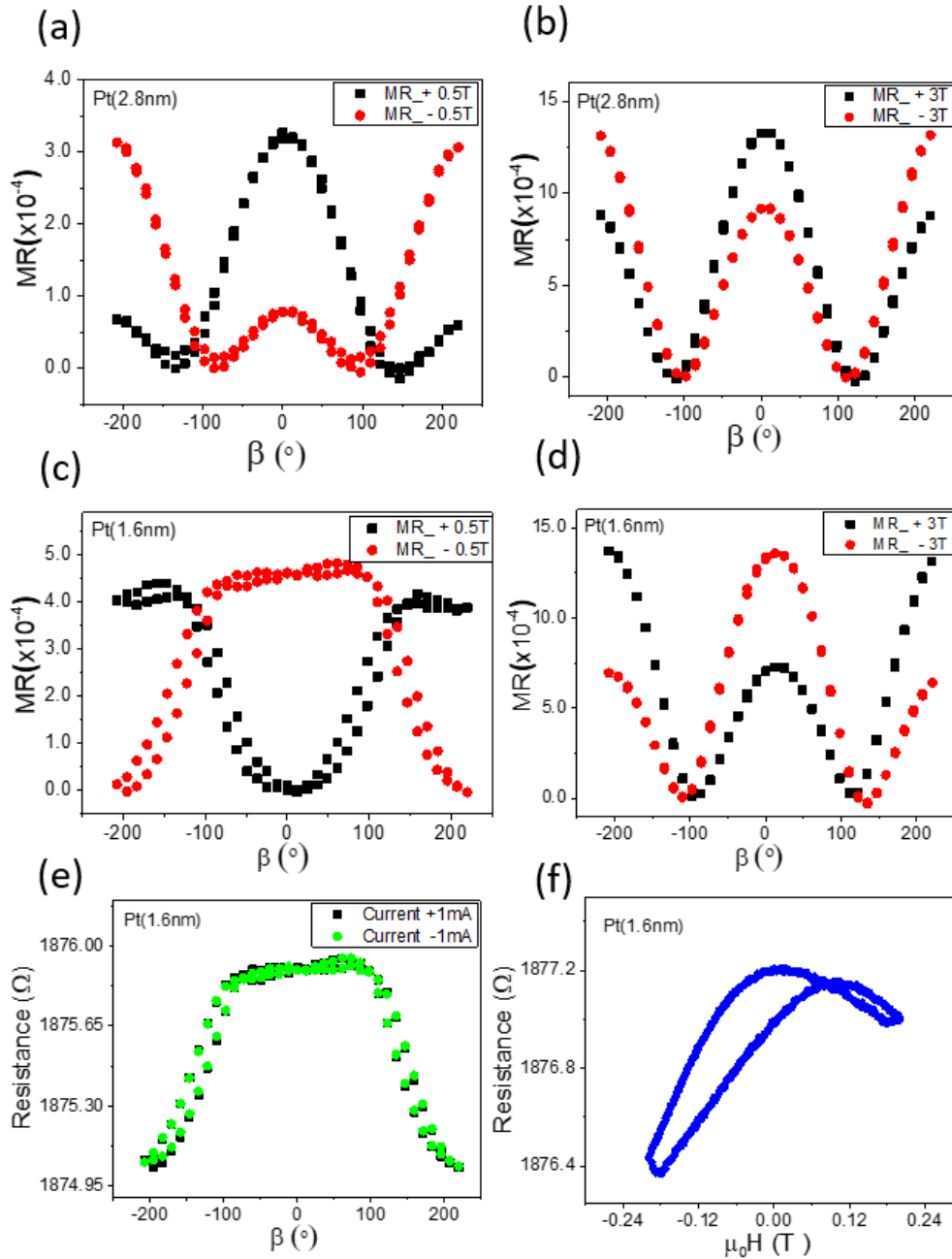
Figure 4.26:   (a) In both the positive (+0.5 T) and negative (-0.5 T) magnetic fields, the Pt 2.8 MR signal is not symmetric with the applied magnetic field in β angle. (b) The same sample (Pt 2.8 nm) has been measured at a higher field (3 T). (c, d) Pt 1.6 nm shows opposite anisotropy to Pt 2.8 nm at low field (0.5 T) and high field (3 T). (e) The measurement at different signs of the current 1 mA and - 1 mA. (f) shows the change in low MR is not symmetric with field.

The resistance differential (resistance at zero - resistance at 180 degrees) in relation to temperature is shown in figure 4.27. The impact of raising the MR at zero degrees is more temperature dependent for thinner Pt as it appears in Pt 1.6 nm but there is no effect in Pt 1.2 nm. The fact that we have no anisotropy in the samples that are thinner, thicker and between those two samples and one sample shows positive anisotropy and the second shows negative anisotropy that looks almost like an oscillation. That is some sort of Ruderman Kittel Kasuya Yosida (RKKY) interaction [195]. The RKKY means that two ferromagnetic lines are parallel when they are very close, but become antiparallel when separated. The a line does depend how close they are and also how far there are.
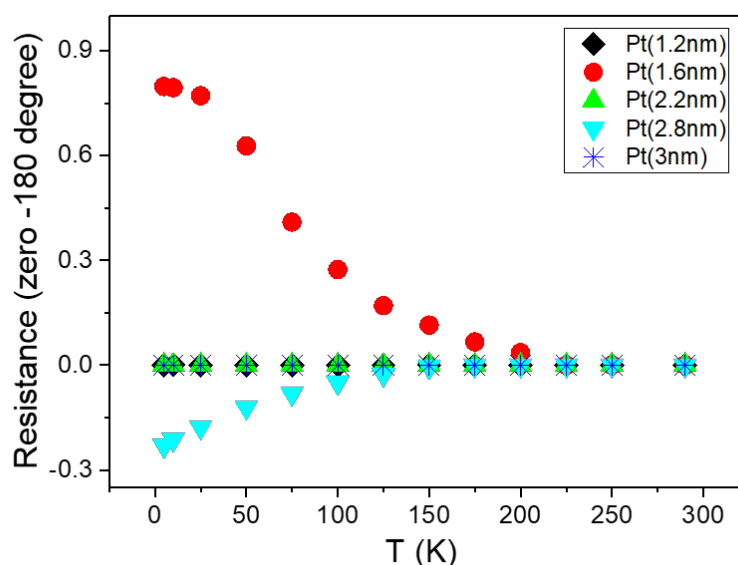
Figure 4.27: The resistance differential between a field at zero or 180 degrees, a qualitative estimation of the out of plane anisotropy, as a function of temperature. The difference shows the opposite sign for 1.6 and 2.8 nm and it is zero for samples with thicknesses of 1.2, 2.2 and 3 nm. For Pt 2.8 nm the resistance difference is nil at about 125 K but for Pt 1.6 nm is not until 200 K.

4.5 Conclusion

In this chapter, the results show that molecular overlayers can enhance the effective spin orbit coupling of heavy metals, as observed in SHMR and AMR measurements of Pt wires on YIG. Additionally, the molecular layers aid in distinguishing the origin of spin scattering mechanisms, such as the coupling with YIG surface magnetisation and a LF-AMR measurable at high temperatures. The enhancement of the effective SOC with molecular interfaces has a wide range of applications, e.g. to reduce the current densities in spin transfer torque memories. The annealing process plays a crucial part in the research on the magnetic properties of YIG/Pt as we discuss its effects on the transport properties of Pt and Pt/C_{60}. The fact that the anisotropy is more evident or appears at higher fields in annealed samples means there is a Pt-YIG magnetically active layer that could be responsible for the out of plane uniaxial anisotropy observed in transport measurements. Further work, e.g. magnetometry in optimised YAG/YIG/Pt layers, would be needed to confirm this hypothesis.

CHAPTER 5

Spin Hall magnetoresistance in YIG/Ta and YIG/Ta/C_{60}

5.1 Introduction

Tantalum can be produced in one of two crystal structures: the stable BCC α-phase or the metastable tetragonal β-phase [196]. The two phases are very different and hence suitable for various applications. The different phases of tantalum demonstrate considerable variations in electrical resistivity. The α-phase has a resistivity of 10-60 $\mu\Omega$cm [197; 198], while the β-phase has a higher resistivity (100-200 $\mu\Omega$cm) [199; 200]. The complete amorphous tantalum film has a resistivity of more than 200 $\mu\Omega$cm [201]. The recent discovery of a large spin Hall effect in β-Ta has reignited interest in this phase, which could be essential for the development of next-generation magnetoresistive memory systems [74]. The resistance of YIG/Ta systems varies from that of YIG/Pt systems depending on magnetic field direction, which can be described using the framework of spin Hall magnetoresistance [78].

This chapter introduces the transport measurements investigation of Ta and Ta/C_{60} over a range of Ta thicknesses and temperatures. A metallic layer forms at the interface between Ta and C_{60}, allowing charge transfer from the metal to the molecules. The SHMR measurements in this chapter were performed at a field of 0.5 T (pure SHMR), where other field-dependent effects are comparatively small once the YIG has been saturated. At low fields of 1-30 mT, there is again an anisotropic magnetoresistance, as it was the case in YIG/Pt, and once more it is enhanced for all temperatures and sample thicknesses by C_{60}.

5.2 Spin Hall magnetoresistance in tantalum

5.2.1 Resistivity dependence on temperature

Tantalum wires were deposited by sputtering using the masking technique as describe in chapter 3. The method follows what we did in Pt deposition where we grow 100 μm wide wires with 3.6 mm long. The Ta resistivity results particularly are in contrast with the platinum resistivity. The resistivity displays the behavior expected in a polycrystalline. Figure 5.1 shows the resistivity as a function of

temperature for YIG/Ta wires. Instead of the resistivity decrease as the temperature is lowered, it is rising. The Ta wires have a resistivity of (1-2 $\mu\Omega m$) and a negative temperature coefficient of (-500$\times 10^{-6} K^{-1}$), consistent with a sputtered $\beta - Ta$ phase [202]. Opposite to Pt, C_{60} increases the resistivity of Ta as shown in figure 5.1.

There are repercussions to consider with a polycrystalline. At polycrystalline, significant deviations to the weak scattering picture are commonly observed, eventually leading to a change of sign of the temperature coefficient of resistivity. The lack of any long-range order lowers the charge carrier mobility while also raising the residual resistivity [203]. Anderson localization, a process for impurity-induced bound electronic state creation at polycrystalline, is one prominent explanation for this phenomenon [204]. Anderson theorised that the reduced mobility of electrons in poor conductors may allow the lattice deformations to self-trap electrons. This explanation is due to the existence of a strong-coupling between the interplay of polycrystalline and lattice deformations in metals at high temperatures [205].
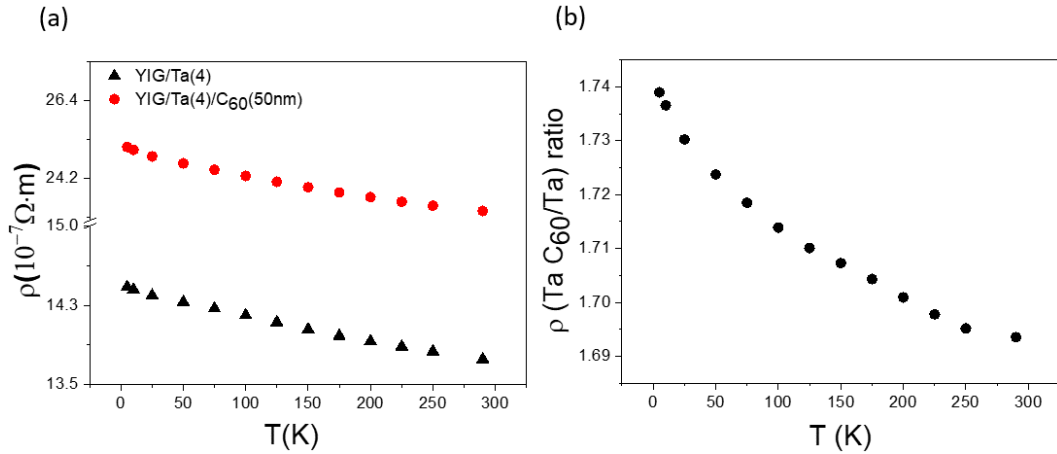
Figure 5.1: (a). Resistivity temperature dependence for a plain 4 nm thick Ta wire is shown in black color and red color for Ta with C_{60}. The resistivity has the opposite temperature coefficient to Pt and conventional crystalline metals. The resistivity ratio of Ta wires without and with C_{60} is presented in (b).

From figure 5.2 (a), it can be seen that the resistivity does not follow the same pattern as conventional metals. The resistivity does not decrease with increasing thickness either. Below 5 nm, especially with C_{60}, the resistivity with respect to Ta thickness makes a sharp drop as the material begins to exhibit NM temperature characteristics. The boundary scattering contributes to increase the RRR factor for Ta vs. Ta/C_{60}, but the RRR ratio for Ta/C_{60} is roughly linear with Ta thickness. A lower RRR ratio is found for Ta/C_{60}, which we attribute to exist less phonon contribution as shown in 5.2 (b).
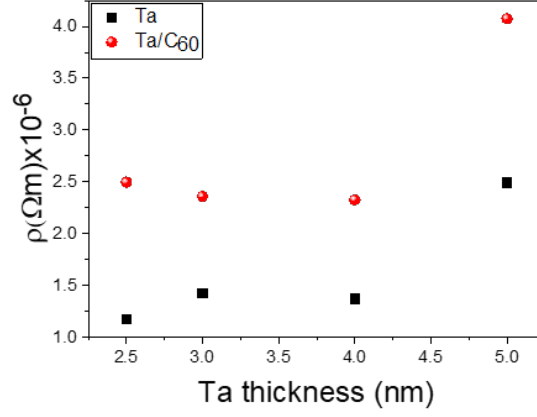
(a)
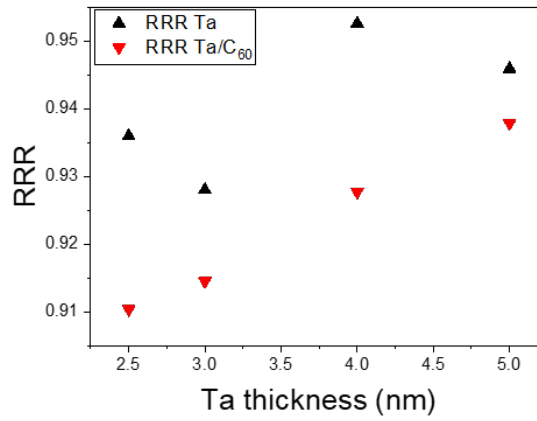
(b)

Figure 5.2: (a) The general shape of the Ta resistivity does not follow what is expected for a NM as a function of sample thickness. The RRR of Ta and Ta/C$_{60}$ wires on YIG/GGG are presented in (b). A lower RRR ratio is found for Ta/C$_{60}$.

5.2.2 Field dependence

We measured the resistivity of YIG/Ta wires in out of plane (perpendicular, or β angle = 0) magnetic fields of up to 3 T. The results are shown in figure 5.3. There is independent of the magnitude of the applied field above the saturation

field of the YIG as the same Pt magnetoresistance field dependence. In YIG/Ta, a C_{60} overlayer increases the resistance rather than reducing it as in Pt, both the SHMR up to 0.15 T and the polynomial MR linear, in the case of Ta at higher fields are enhanced. The Ta-C60 hybridisation may be due to their acting as scattering centres and adding to the polycrystalline or because the electron transfer is changing the DOS of Ta in such a way that the carrier density near the Fermi energy is significantly reduced.
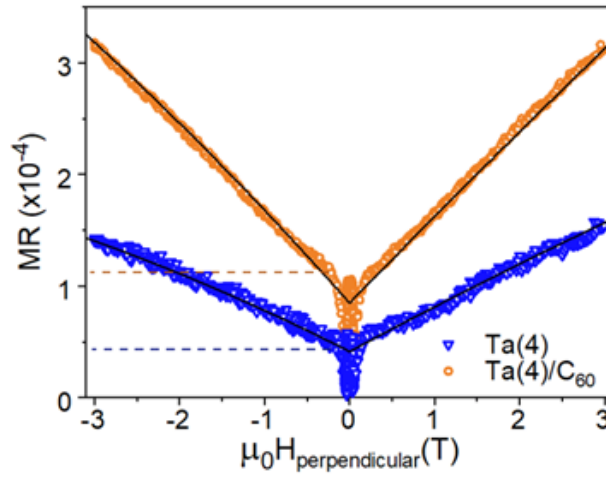
(a)

Figure 5.3: MR in a 4 nm thick Ta wire with a perpendicular magnetic field at 75 K. For YIG/Ta samples, the C_{60} layer increases both the SHMR due to spin accummulation (saturated with the OOP YIG magnetisation at ∼0.2 T), and also increases the high field linear contribution. This is opposite to the case of Pt, and may be related to the enhanced resistivity observed in Ta/C_{60} samples.

5.2.3 Tantalum Fitting of Transport Measurements

As in platinum, the SHMR of Ta wires on YIG/GGG is obtained by fitting the change in resistance with the angle β in a magnetic field of 0.5 T. Figure 5.4 shows an example of this fit for a Ta wire and its Ta/C$_{60}$ partner. The SHMR vs temperature data is fitted to calculate the change in spin Hall angle between Ta and Ta/C$_{60}$ whilst keeping the same spin-mixing conductance.

The same parameters and equations as for platinum are used to fit the Ta data. Figure 5.5 shows an example of this fit applied to a Ta wires of different thickness and their Ta/C$_{60}$ partners. The data fits a simple linear trend until approximately 25 K, when the effect increases for thicker Ta wires. The thickest Ta wires show a sharp rise in the SHMR at low temperatures instead of flattening out as it happens with Ta/C$_{60}$ wires. Theses wires could not be fully fitted with the standard model in equation 2.9 due to the upturns in SHMR at the low temperature. The cause of this upturn in the SHMR for plain Ta wires is probably due to a positive contribution from a different MR that becomes stronger at low T. However, for Ta/C$_{60}$ the fit shows a good match to the data across the full temperature range.
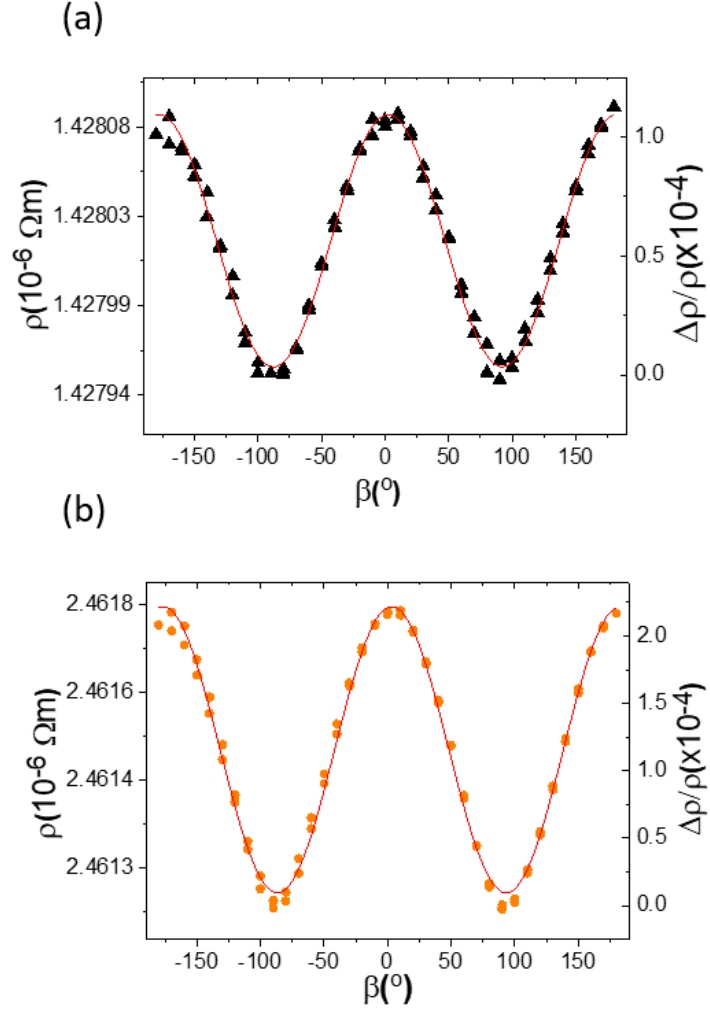
Figure 5.4: Examples of SHMR fits to $cos(\beta)^2$. Resistivity and magnetoresistance measured at 50 K for Ta wires 4 nm thick without (a) and with (b) a 50 nm C_{60} overlayer, grown on a GGG/YIG(170 nm) substrate. The applied field for these measurements is 0.5 T.

5.2.4 Thickness dependence of the SHMR in tantalum

The full temperature SHMR dependence was measured for different Ta thickness as shown in figure 5.6 (a). The measurements are done at 0.5 T in the transverse to perpendicular configuration (β angle). The SHMR in general trend increases as the temperature is lowered to around 50 K. This temperature is when the
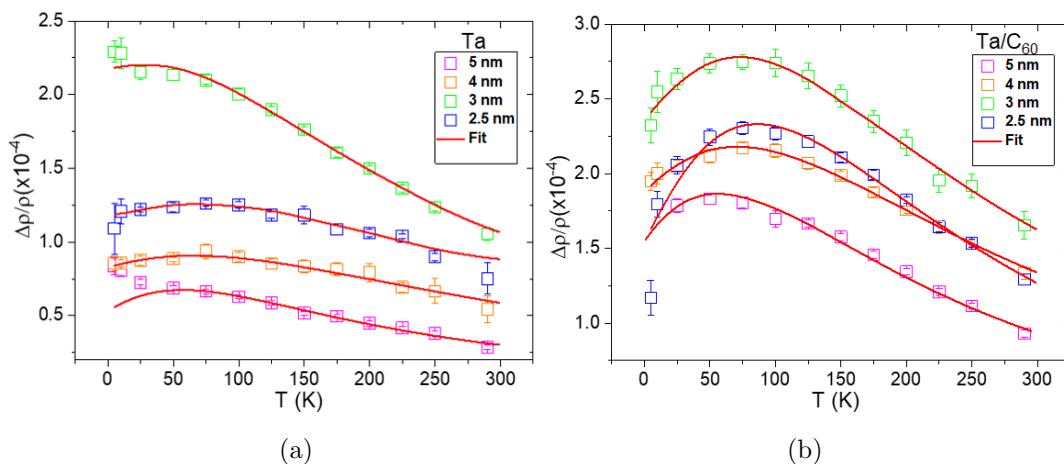
Figure 5.5: The SHMR data fitting for different Ta thicknesses as a function of temperature. (a) The thickest Ta wires could not be fitted due to the upturns in SHMR at the low temperature region. (b) The upturn in the SHMR at low temperatures for Ta/C$_{60}$ is absent.

spin diffusion length of Ta equals the Ta thickness. There is a deviation at low temperatures approaching 10 K which is not consistent. The maximum in the Ta SHMR occurs at a lower temperature than for platinum. Figure 5.6 (b) shows the SHMR ratios between YIG/Ta and YIG/Ta/C$_{60}$ for different wire thicknesses. As it happened in Pt wires, the SHMR is larger with a C$_{60}$ overlayer for all temperatures and thicknesses, but the ratio is almost constant for all temperatures, whereas in Pt the temperature dependence is very different for thick (> 2.5 nm) and thin (< 2.5 nm) wires. Here, the conducting layer at the interface is more likely not dependent on the Ta thickness. Contrary to what happens in Pt, for the thinnest measured films of 1.5 nm, the conducting layer at the interface adds an effective thickness to the Pt.

(a) (b)
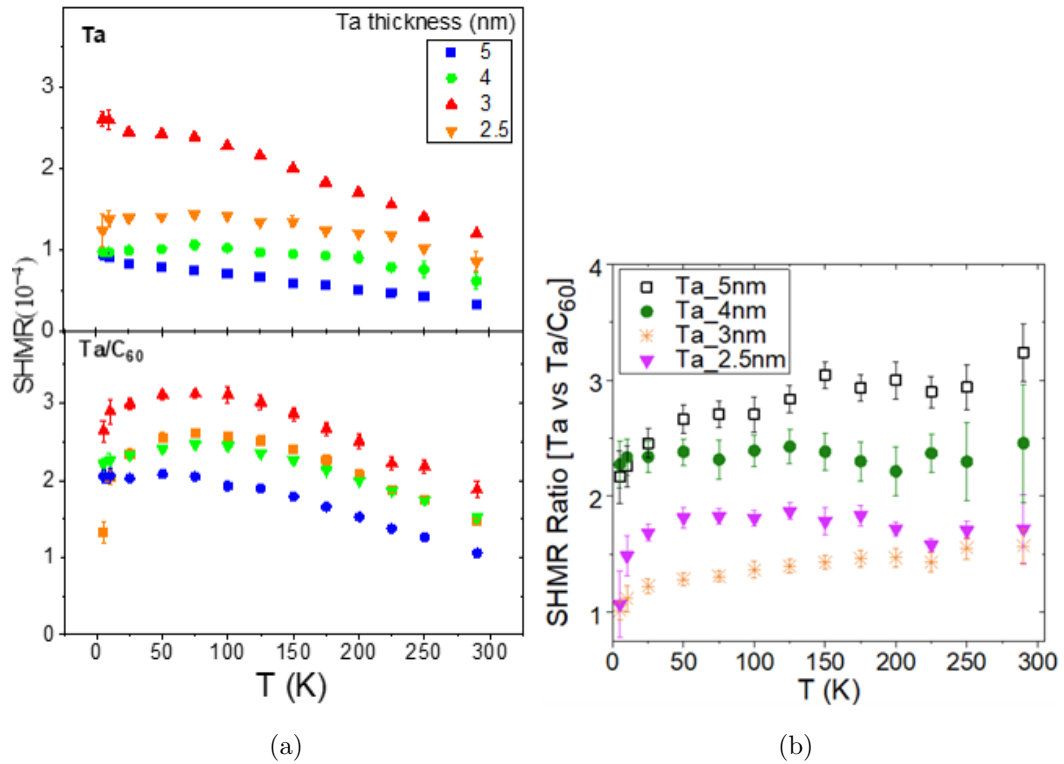
Figure 5.6: (a) SHMR for Ta and equivalent Ta/C$_{60}$ wires of different thicknesses on GGG/YIG(170 nm) films. The SHMR is higher in Ta/C$_{60}$ for all temperatures and thicknesses. (b) Ratio of the SHMR for different temperatures and Ta wire thicknesses.

The SHMR in tantalum is presented as in platinum with the same angular dependence. The data in figure 5.7 shows a similar SHMR and Θ_{SH} effects to the platinum, with the SHMR reaching a maximum for 3 nm thick Ta wires. The maximum at 3 nm thickness is higher than what we found in platinum which points out that the spin diffusion length is larger. Fitting the data extracts a higher spin Hall angle for Ta wires with C_{60}. The results are similar to Pt, albeit with smaller effects (both the SHMR and the change induced by C_{60}), which shows reproducibility and an effect consistent with changes to the effective SOC.
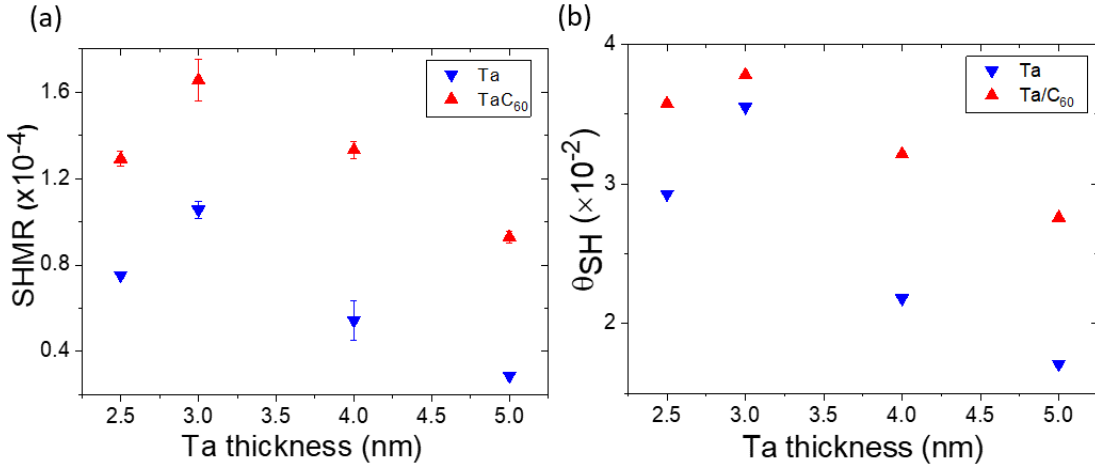
Figure 5.7: (a). SHMR measured at room temperature for Ta and Ta/C60 wires of varying Ta thickness. The SHMR follows a similar thickness dependence as platinum but with a maximum that occurs at a larger thickness. The molecular interface enhances the SHMR for all samples which results higher Θ_{SH} for Ta wire with the molecular overlayer in (b). The applied field for these measurements is 0.5 T.

The SHMR shows a modest increase with C_{60} at lower thickness, as seen in figure 5.7. This enhancement is about 60 % in thinner samples and it is about 140 % in thick samples. It is necessary to conduct MR up to 3 T at different thicknesses to explain the smaller C_{60} enhancement at lower thickness, as illustrated in figure 5.8. The measurements at higher applied magnetic fields

could be confirmed by other contributions to the MR. This could be an indicator of weak localisation, which is expected to be smaller in thick samples [181].
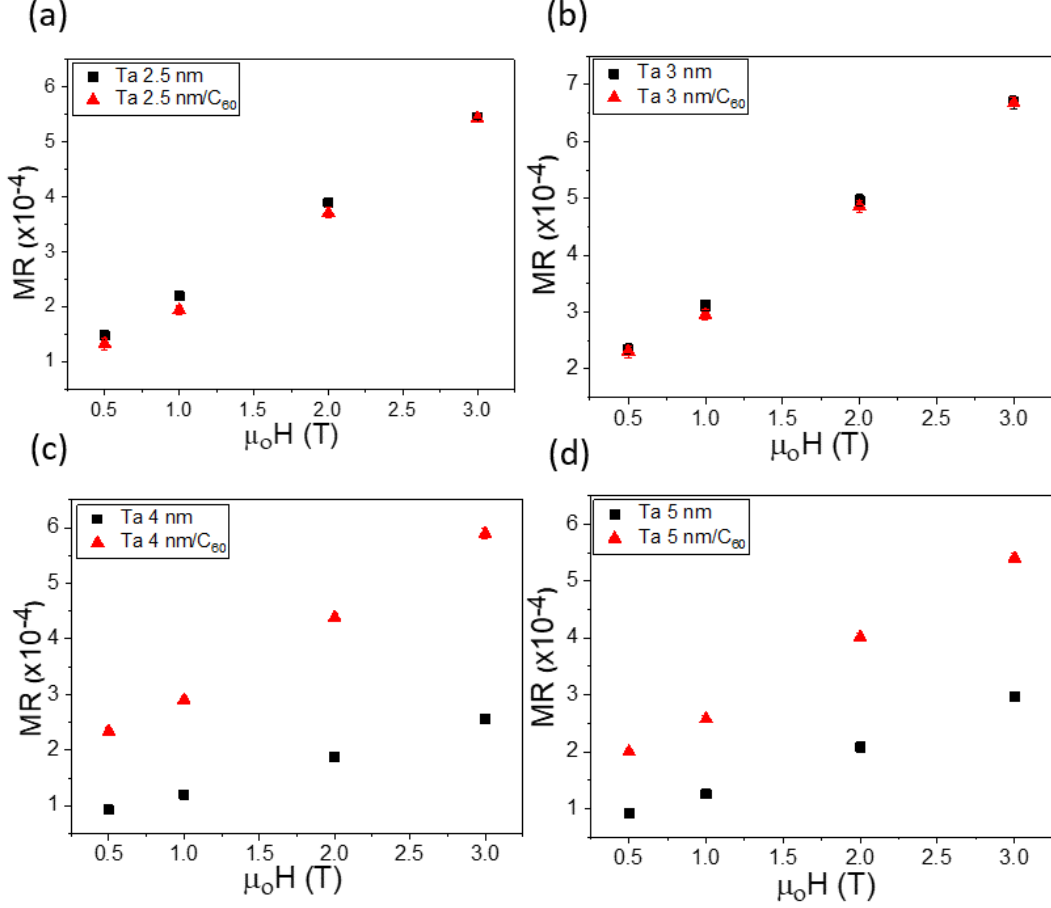
Figure 5.8:   MR in Ta and Ta/C_{60} measured at 5 K in fields up to 3 T in perpendicular to transverse (β) configuration. Note that values will include the SHMR and other contributions, in particular above 0.5 T. (a,b) The MR increases with increasing magnetic fields, but the C_{60} wire does not have a higher value. The higher C_{60} enhancement at thicker thickness is shown in (c and d).

To continue our investigation into the origin of the smaller SHMR enhancement for the thinner samples, the Ta (2.5 nm) wires were also measured at different fields and temperatures. At a temperature above 50 K, the C_{60} contribution is obvious. The temperature effect points as well to weak localisation in thin

Ta thickness [172]. Thus, the weak localization effect is much stronger at low temperatures as shown in figure 5.9.
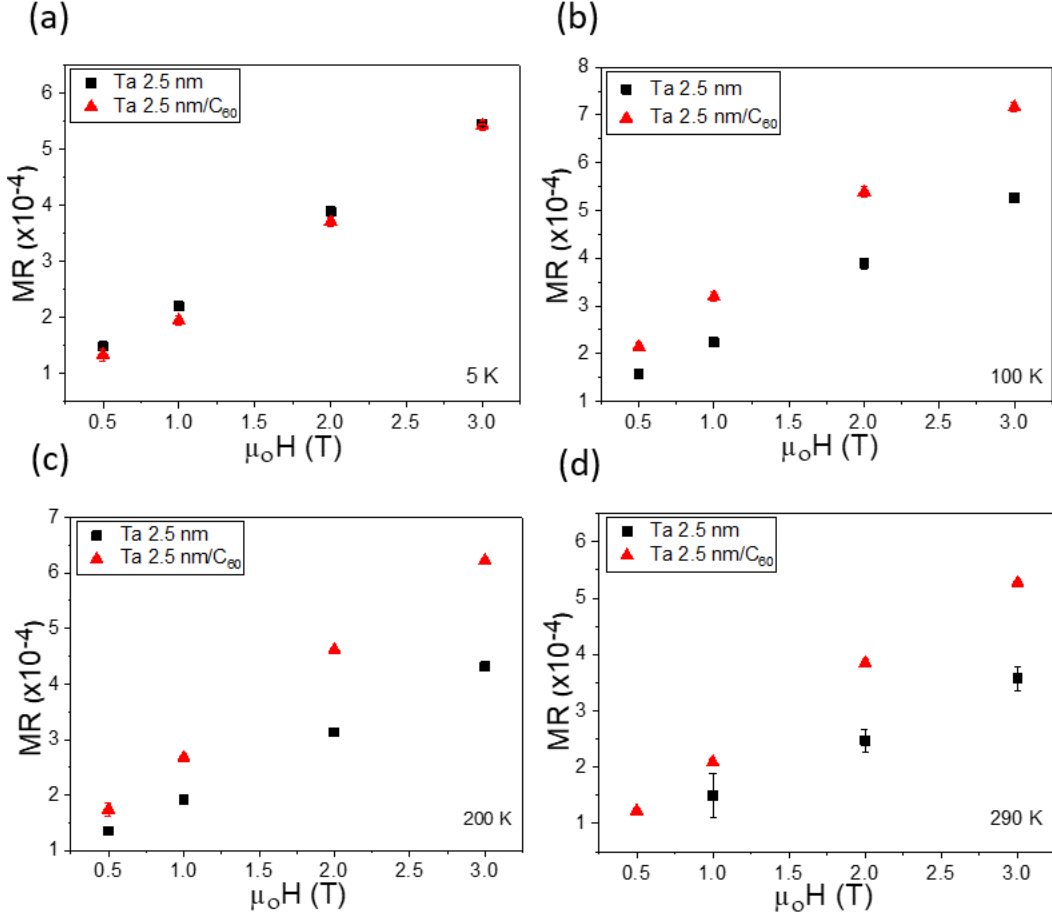
Figure 5.9: (a) MR in Ta 2.5 nm and Ta/C$_{60}$ measured at 5 K in fields up to 3 T in perpendicular to transverse (β) configuration. Measurement temperature included in the graph. (b-d) At 100 K, 200 K, and 290 K, the MR is enhanced by C$_{60}$, but not at 5 K, where we expect the strongest quantum dimensional effects, i.e. weak localisaiton.

5.2.5   Low Field AMR in Ta

For Ta grown on YIG, an additional change in resistance is observed at low magnetic fields when the direction of an applied magnetic field is changed with respect to the electrical current. Similar to Pt, a molecular enhancement of the low field AMR is observed for Ta wires. Magnetoresistance in the perpendicular configuration for Ta and Ta/C_{60} is shown in figure 5.10, with the low field AMR as an inset on right.
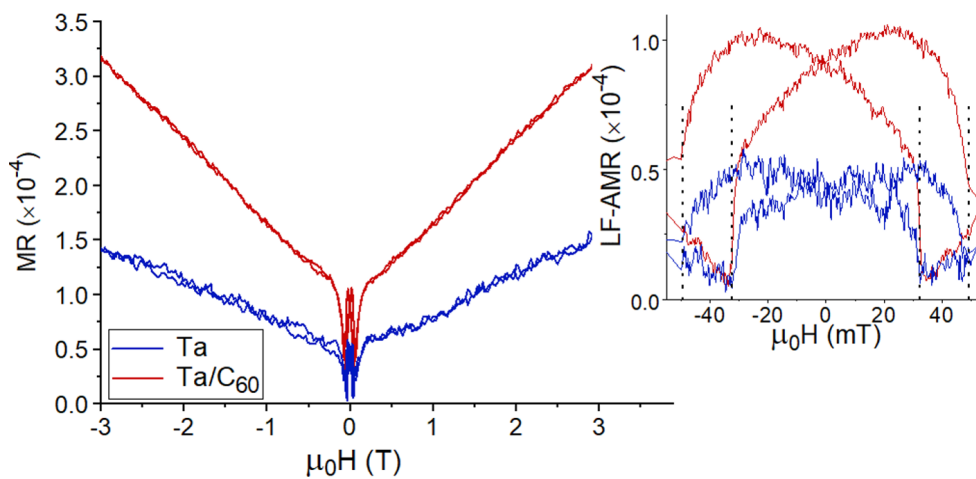
(a)

Figure 5.10:   When sweeping the magnetic field, the low field AMR is obtained. Ta wires show a molecular increase in the low field AMR, similar to Pt wires.

Figure 5.11 shows the LF-AMR, which is characterised by the existence of peaks of opposite sign for magnetic fields perpendicular or longitudinal to the current, respectively. The low field position of the out-of-plane LF-AMR peak could point again to a YIG surface layer with an out-of-plane easy axis or, at least, not a strong in-plane anisotropy. The LF-AMR has the same shape and peak position with or without a molecular overlayer, but the magnitude is larger when C_{60} is present.
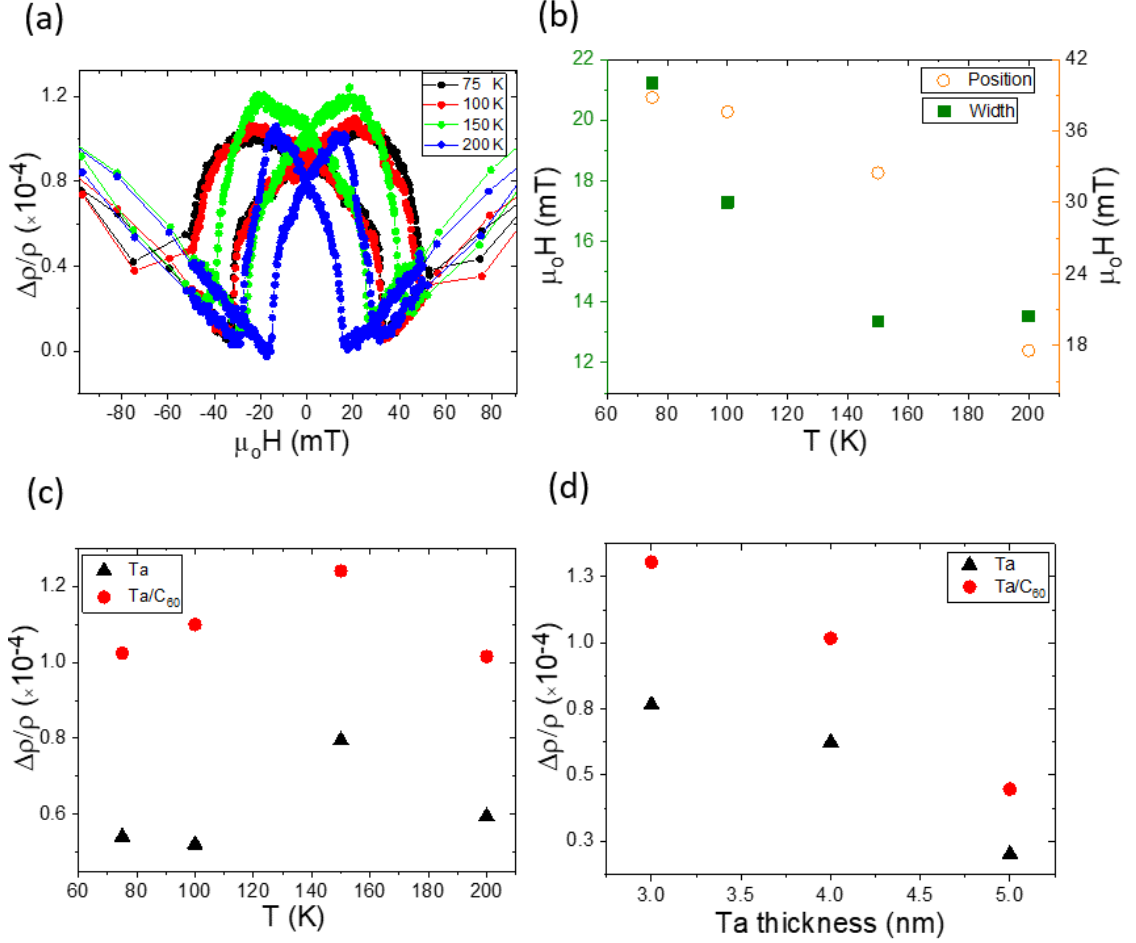
Figure 5.11: (a) Perpendicular LF-AMR for GGG/YIG(170)/Ta(4)/C$_{60}$(50), thicknesses in brackets in nm. (b) The perpendicular LF-AMR peak position and width are increased in steps as the temperature is reduced. (c) Different temperatures of LF-AMR comparison between YIG/Ta and YIG/Ta/C$_{60}$. (d) LF-AMR measured at an out of plane, perpendicular field for Ta and Ta/C$_{60}$ wires of varying Ta thickness. The molecular interface enhances the AMR for all samples.

5.3 Conclusion

In this chapter, the results show that molecular overlayers can enhance the effective spin orbit coupling scattering of Ta wires on YIG, as observed in SHMR and AMR measurements. We found that the Ta wires had a resistivity of (1-2 $\mu\Omega m$) and a negative temperature coefficient of (-500$\times 10^{-6} K^{-1}$), which is consistent with a sputtered $\beta - Ta$ phase [202]. Ta resistivity exhibits a polycrystalline, with significant departures from the weak scattering image, finally leading to a shift in the sign of the temperature coefficient of resistivity. One common explanation for this phenomena is Anderson localization, a mechanism for impurity-induced bound electronic state formation at polycrystalline. The metal-C_{60} hybridisation points act as scattering centres and add to the polycrystalline (more scattering centres at the hybridised interface where C_{60} couples with Ta). It is possible that the electron transfer is changing the DOS of Ta in such a way that the carrier density near the Fermi energy are significantly reduced. That why the linear MR in Ta was stronger for Ta/C_{60} than plain Ta. Furthermore, the molecular layers help in determining the origin of spin scattering processes such as YIG surface magnetisation coupling and an LF-AMR observable at high temperatures.

CHAPTER 6

Spin Hall magnetoresistance in YIG/PtMn and YIG/PtMn/C$_{60}$

6.1   Introduction

PtMn is an antiferromagnet (AFM) material that is used as a pinning material in exchange bias systems for practical applications because of its strong pinning field and high blocking temperature [206; 207; 208]. As-deposited PtMn/FM bilayers, on the other hand, displays no exchange bias because thin film PtMn is paramagnetic rather than antiferromagnetic [209]. Also, in this project, PtMn is more likely to be a range of stoichiometries and paramagnetic species.

Here, we have studied the spin Hall magnetoresistance for YIG/PtMn with and without C_{60}. PtMn has been shown to have a strong spin Hall effect [210]. We aim to: investigate the mechanisms that generate spin orbit scattering at the hybrid conducting interface and maximise the effect. We hope in the future to use the Mn L2,3 edge to do Near edge X-ray absorption fine structure (NEXAFS) and XMCD measurements of changes induced by C_{60}. However, due to covid and limited access to facilities, we have not had a chance to do the experiments. Also in this chapter, we investigate the SHMR and AMR before and after annealing. Cross-sectional high resolution TEM measurements in figure 6.6 were performed by Dr. Damien McGrouther and Dr. Tim Moorsom in University of Glasgow. However, we have done all of the design, sample fabrication and analysis of the images.

6.2   Spin Hall magnetoresistance in PtMn

6.2.1   Resistivity dependence on temperature

Sputtering was used to deposit PtMn wires using the masking technique described in Chapter 3. The method is the same as in the previous two chapters, with wire widths of 100 μm and lengths of 3.6 mm. The effects of PtMn resistivity are distinct from those of platinum resistivity. The resistivity behaviour of a polycrystalline metal can be anticipated. The resistivity of PtMn as a function of temperature is shown in figure 6.1. As the temperature is reduced, the resistivity rises instead of decreasing. The resistivity of the PtMn wires is (0.4 - 0.5 $\mu\Omega$m), of

the same order as the resistivity reported in other studies [211]. As shown in figure 6.1, the resistivity of PtMn/C_{60} is higher than for PtMn. This is the opposite to what happened with plain Pt vs Pt/C_{60} but the same as what happened with Ta wires, which showed as well a negative thermal coefficient for the resistivity.
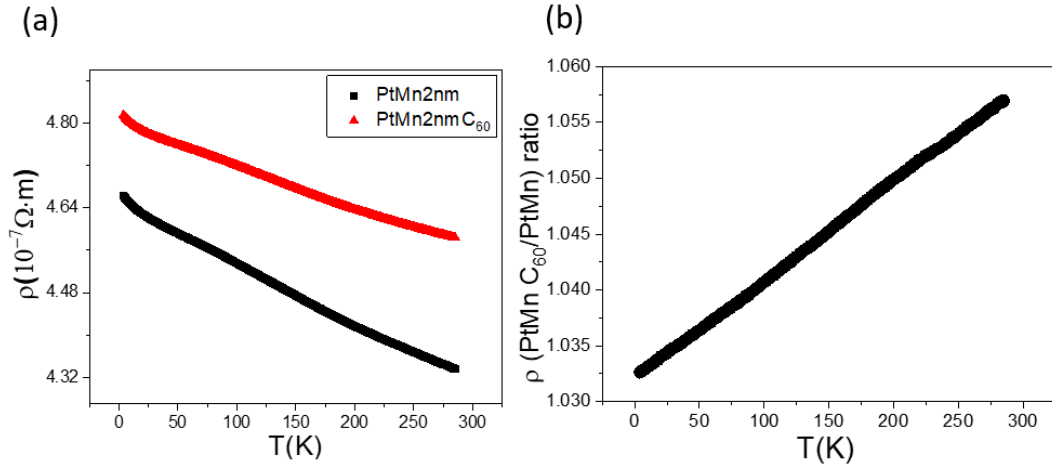
Figure 6.1: (a). The relation between the resistivity and the temperature for a plain PtMn wire is shown in black color and red color for PtMn with C_{60}. The resistivity ratio of PtMn vs. PtMn/C_{60} is presented in (b).

The resistivity does not follow the same pattern as that of a regular metal, as shown in figure 6.2 (a). As the thickness is increased, the resistivity does not decrease. The RRR factor for PtMn/C60 vs. PtMn (Fig. 6.2 (b)) is higher due to boundary scattering, but the RRR ratio for PtMn is more linear as the PtMn thickness increases. PtMn has a lower RRR ratio, which we attribute to the presence of less phonon contribution, as seen in figure 6.2 (b).
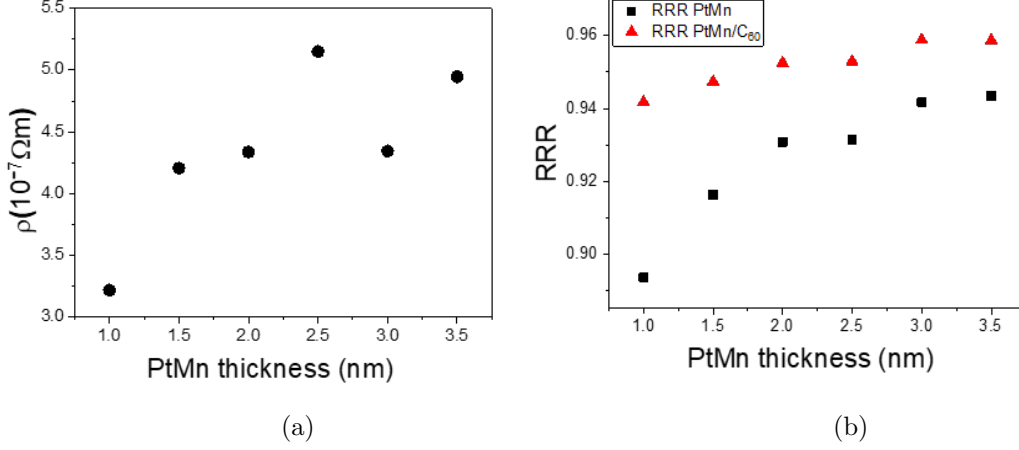
Figure 6.2: (a) The PtMn resistivity as function of sample thickness. The RRR of PtMn wire with PtMn/C_{60} are presented in (b). A higher RRR ratio is found for PtMn/C_{60}, which we attribute to less boundary scattering.

6.2.2 Out of plane magnetoresistance

We carried out measurements of the MR with fields along the YIG's hard axis, and in plane (easy axis) as shown in figure 6.3 (a). The same Pt magnetoresistance field dependency exists regardless of the magnitude of the applied field above the YIG saturation field, i.e. between $\sim$0.25 and 3 T. Both the SHMR is not fully saturated until 0.25 T, and the MR at higher fields are enhanced in PtMn/C_{60}, where the C_{60} raises resistance rather than decreases it as in Pt. In particular, with PtMn/C_{60} as shown in figure 6.3 (a), the curve is obviously not parabolic, but rather proportional to $B^{0.5}$. This additional MR in PtMn/C_{60} agrees with the emergence of weak antilocalization [91]. Figure 6.3 (b) shows the perpendicular MR for PtMn/C_{60} as a sample thickness. The thinner region of a sample is where finite size effects are observed most acutely [212]. The magnitude of MR for PtMn (1 nm) with an applied field of 3 T is 9×10^{-4}, which is much stronger than for thicker samples. The comparison of MR at room temperature and at 5 K is shown in figure 6.3 (c). Based on this, we can validate the existence of weak antilocalization in PtMn/C_{60} where higher MR is seen in thinner thicknesses and

at low temperature. Figure 6.3 (d) shows the magnetoresistance determined in the β plane at room temperature with a magnetic field of up to 3 T.
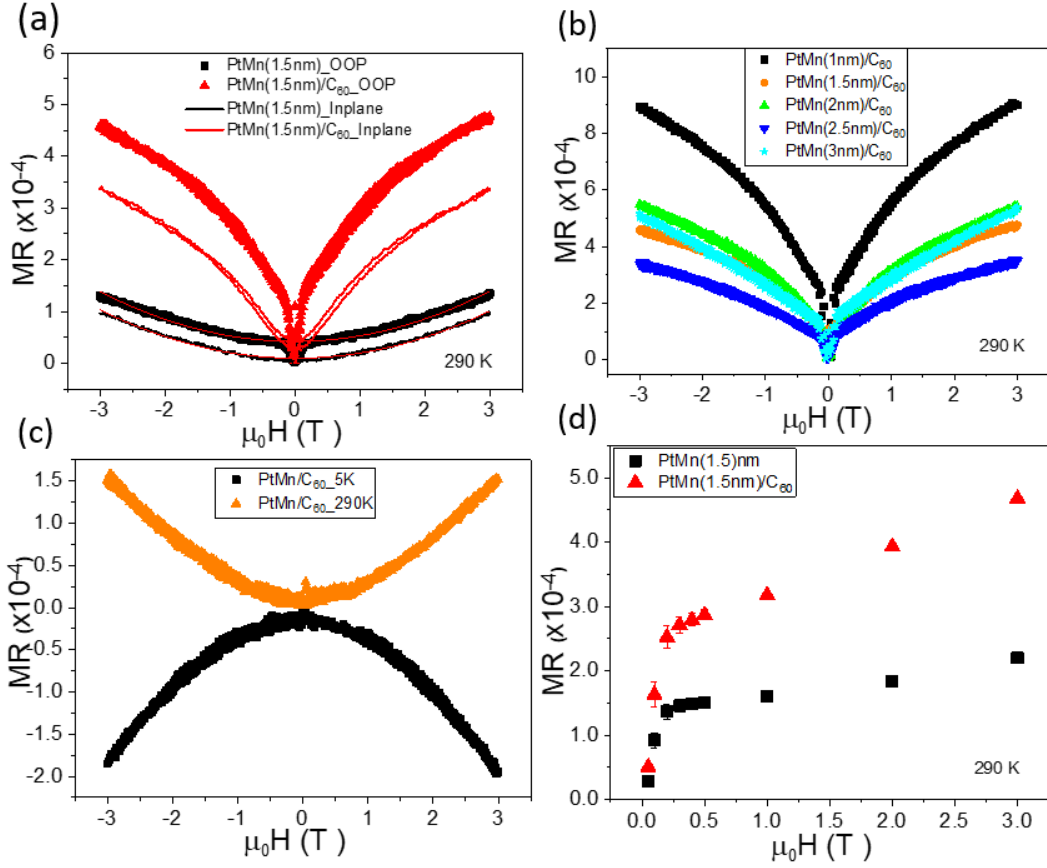
Figure 6.3: MR in PtMn and PtMn/C$_{60}$ wires with a perpendicular (a) and in-plane (b) magnetic field. Here for YIG/PtMn sample, the C$_{60}$ layer increases the MR due to spin accumulation, and also increases the polynomial contributions opposite to platinum. (c) A negative contribution from a different MR that becomes stronger at low temperature. (d) The SHMR increases with applied magnetic field strength in a pattern similar to the platinum, where PtMn/C$_{60}$ has higher SHMR.

6.2.3 SHMR PtMn thickness dependence

As shown in figure 6.4 (a), the full temperature dependence of the SHMR was measured for various PtMn thicknesses. The measurements were carried out at a magnetic field strength of 0.5 T in a transverse to perpendicular configuration (β plane). When the temperature is lowered to about 50 K, the SHMR pattern vanishes. The small rise in SHMR below 50 K differs from the SHMR in Pt. The primary difference is that at low temperatures, the PtMn SHMR drops to zero. The MR then increases because of the emergence of other MR effects at low temperatures. There is also a possibility of a dead layer at the interface that becomes magnetic at low temperatures. Thus, it could impede the transfer of angular momentum that the SHMR depends on. Also, the maximum in the PtMn SHMR occurs at a higher temperature than that in Pt. The SHMR peak for PtMn is around 250 K, while the peak for Pt is around 100 K. The peak of the SHMR is identified as corresponding to the temperature when the spin diffusion length equals to the thickness, as previously discussed in the Pt section 4.2.4 .For PtMn thicker than 2.5 nm, the SHMR is decreased due to spin flip scattering. The interfacial C_{60}/PtMn enhances the SHMR effect for all different PtMn thicknesses. The maximum effect of the molecular layer takes place for the thinnest layers (1 nm), as shown in figure 6.4 (b).
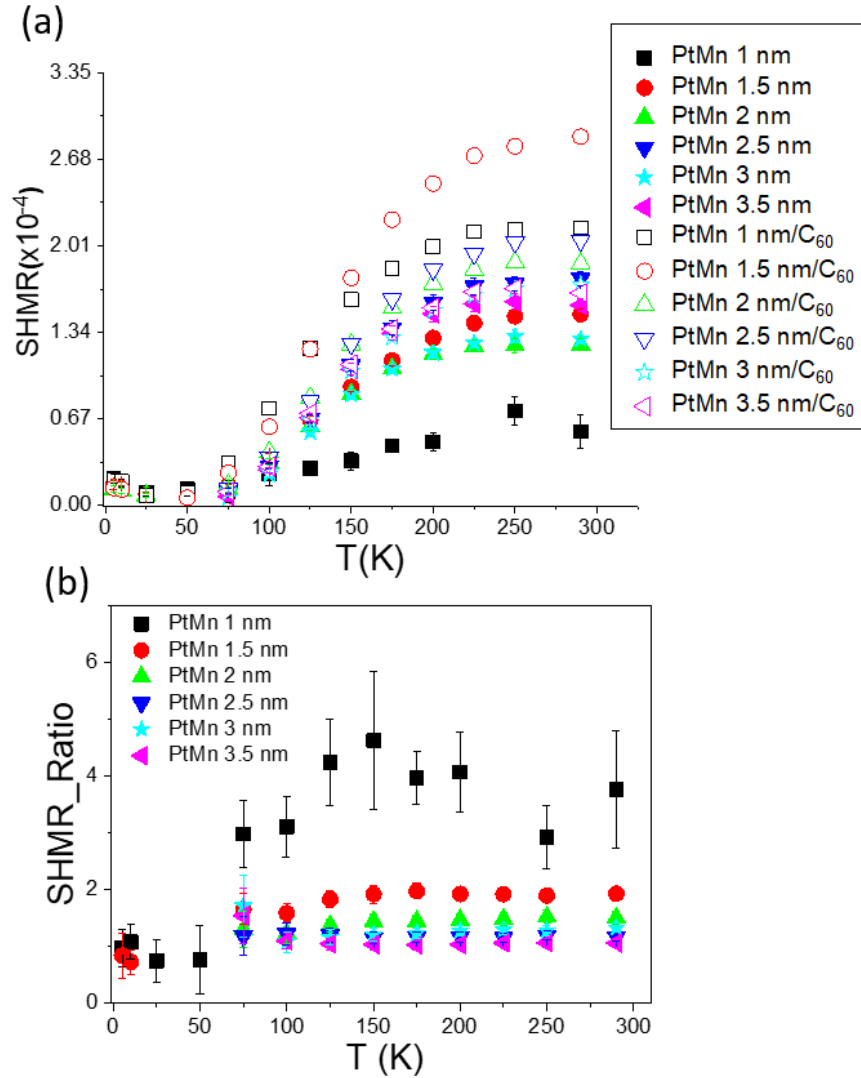
Figure 6.4: (a) SHMR in PtMn alloy wires with and without a C_{60} interface. The SHMR is higher in PtMn/C_{60} for all temperatures and thicknesses. (b) SHMR Ratios between PtMn/C_{60} and PtMn wires.

6.2.4 Low Field AMR in PtMn

Like YIG/Pt and YIG/Ta, YIG/PtMn also exhibits a low field AMR, where an additional shift in resistance is observed as the direction of the applied magnetic field is changed in relation to the electrical current. As shown in figure 6.5 (a),

LF-AMR is characterized by the presence of peaks, positive or negative depending on the field direction. When comparing longitudinal and perpendicular MR, it is worth noting that they exhibit the same coercivity (field dependence) for both orientations, which is different from plain Pt. This is really what makes PtMn very different from other MR, since it implies spontaneous magnetic ordering playing a role.

(a)   (b)
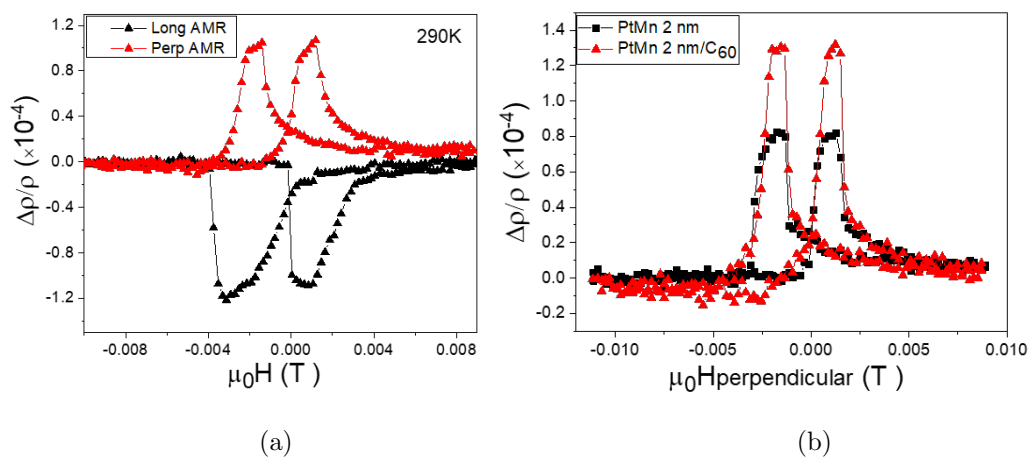
Figure 6.5: (a). Room temperature LF-AMR comparison between longitudinal and perpendicular. (b) LF-AMR comparison between YIG/PtMn and YIG/PtMn/C_{60}. The curves are qualitatively the same, but the magnitude of the effect is enhanced by the molecules.

Figure 6.5 (b) shows the LF-AMR in the perpendicular configuration for PtMn and PtMn/C_{60}. With or without a molecular overlayer, the LF-AMR has the same shape and peak position, but the magnitude is greater when C_{60} is present. This indicates that LF-AMR has the same coercivity with or without a molecular overlayer, implying that the domain walls have the same micromagnetic configurations. The molecular enhancement of the LF-AMR is similar to that of Pt and Ta.

6.2.5 Annealing effects on PtMn by TEM

YIG(40 nm)/PtMn(2nm)/C$_{60}$(50nm)/Al(2nm) samples annealed at 250 °C were imaged using TEM. This method is utilised to characterise the interfaces further and offer information on inter-diffusion, uniformity and crystallinity before and after annealing. A cross-sectional TEM image of the PtMn wire before and after being annealed is shown in figure 6.6. What can be seen different before and after annealing is that the crystallinity of PtMn looks better after annealing. The top of the PtMn layer appears to be a little rough, as if it had aggregated during annealing. Though there are two distinct crystalline zones visible at the bottom, it appears to have good crystallinity. The PtMn alloying is rather good, and there is clearly no full phase separation, although the elemental mapping appears to show a thicker Mn layer that extends above and below the Pt to the film surfaces.
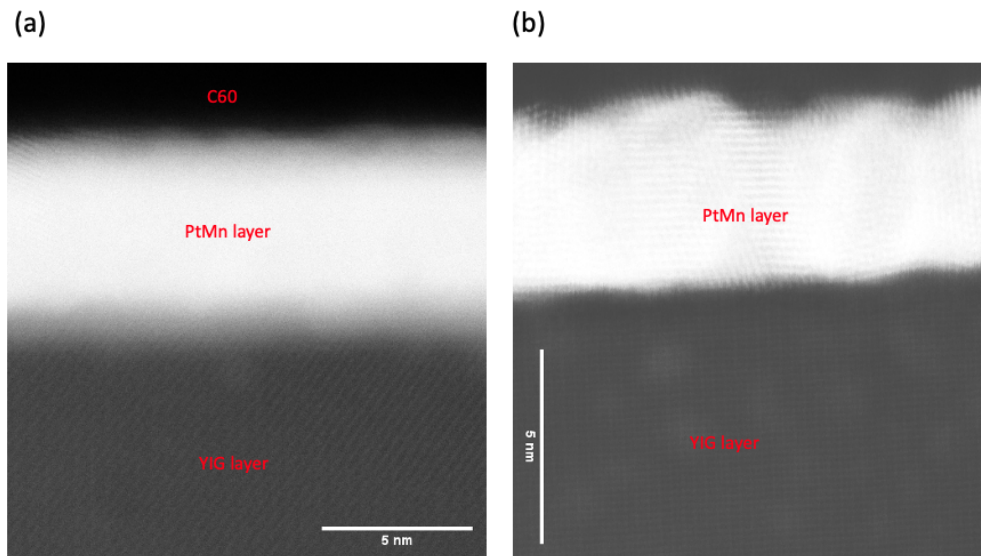
Figure 6.6: Cross-sectional high resolution of TEM images of the PtMn wire on a YIG substrate. The images show the sample (a) before and (b) after annealing using. The image in (b) after annealing shows good crystallinity and ion distribution, with uniform distribution of Mn.

6.2.6 Annealing effects on PtMn resistivity

The resistivity of PtMn as a function of annealing temperature is shown in figure 6.7 (a). After annealing, the resistivity is still characteristic of a polycrystalline metal. As the temperature is reduced, the resistivity increases. Furthermore, after annealing at 300 °C, the resistivity is increased by 10%. In contrast, the resistivity of PtMn/C_{60} decreases as the annealing temperature rises as shown in figure 6.7 (b). After annealing at 300 °C, the PtMn/C_{60} resistivity drops by almost a factor two and, significantly, shows now the characteristic temperature dependence of a conventional, ordered metal. Annealing improves the additional conducting hybrid interface and it is likely that the hybridised layer will increase during annealing temperature rises acting as a parallel conduction channel to the polycrystalline PtMn. However, this metallised C_{60} layer has a relatively small (compared to Pt) SOC, and therefore we expect it will not contribute to the SHMR.

(a)   (b)
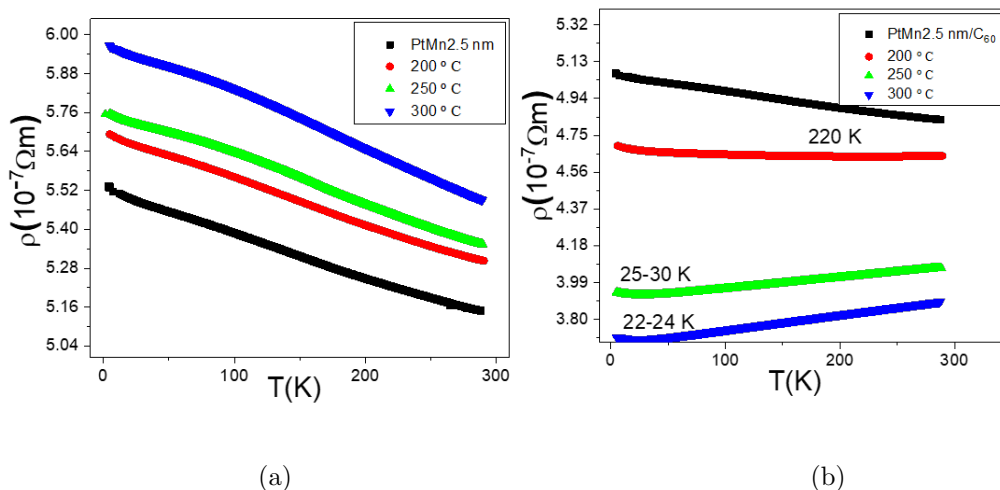
Figure 6.7: (a) The resistivity of PtMn increases after annealing. (b) With C_{60}, the PtMn resistivity shows metallic behaviour for annealing temperatures of 250 °C or above. We hypothesize this may be due to the additional conducting hybrid interface improvements.

6.2.7 Annealing effects on PtMn SHMR

The SHMR of PtMn wires annealed at 200 °C is shown in figure 6.8 (a). The SHMR effect is reduced by about 20% in annealed PtMn samples. It is possible that the decrease in annealed PtMn SHMR is due to PtMn wire degradation. Figure 6.8 (b) shows the SHMR of annealed PtMn wire at 200-300 °C at all temperatures and thicknesses. In comparison, as annealing temperatures rise, the SHMR for PtMn/C_{60} increases. The molecular layer has the greatest effect (factor 2 to 4 change) on thin films (1 nm) at room temperature, as shown in figure 6.8 (b). The explanation for the increased SHMR in PtMn/C_{60} is that this might be due to more non-spin dependent scattering, which in turn increases the rate of spin flip scattering events. It means the scattering with grain boundary and defects.
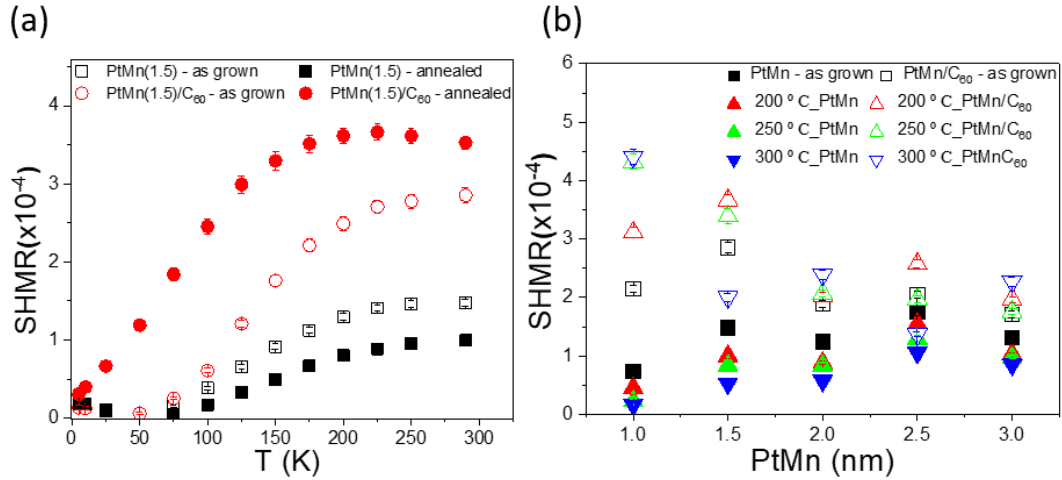
Figure 6.8: (a) SHMR comparison between PtMn alloy wires as sample grown and annealed at 200 °C with and without a C_{60} interface. (b) The effect of the molecular interface is further enhanced via annealing at 200-300 °C.

The spin Hall angle is extracted by fitting the SHMR data in figure 6.9 (a) which is higher with the molecular overlayer. The thinnest film (1.5 nm) has a high spin Hall angle, while the spin Hall angle for wires $\geqslant$ 2 nm is lower as shown in 6.9 (b). This could support the idea of using PtMn as a spin current detector in antiferromagnets through the spin Hall effect [211].
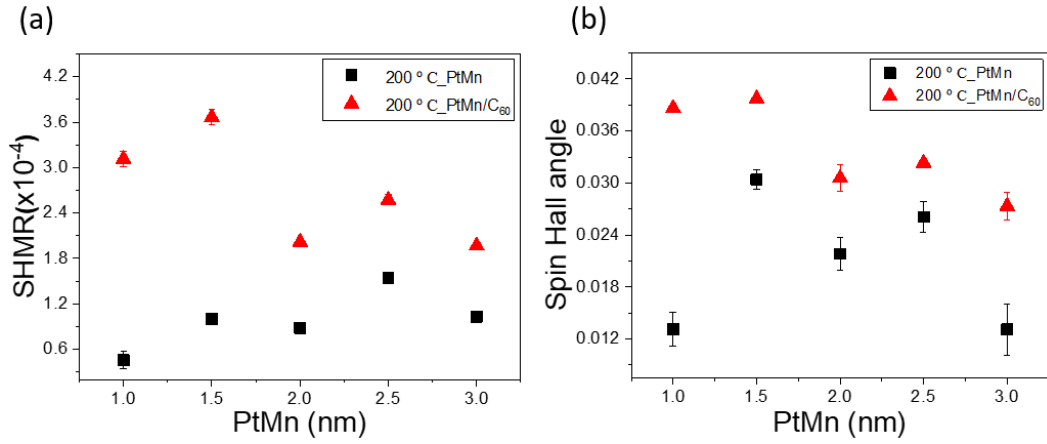
Figure 6.9: (a). SHMR measured at room temperature for annealed PtMn and PtMn/C_{60} wires of varying PtMn thickness. The molecular interface enhances the SHMR for all samples which results higher Θ_{SH} for PtMn wire with the molecular overlayer in (b).

6.2.8 Annealing effects on PtMn AMR

The longitudinal AMR for the same sample structure of YIG/PtMn (2 nm)/C_{60} was measured at a range of temperatures before and after annealing. Figure 6.10 shows the AMR was measured at different temperatures of 150 K. The field has a significant impact on the longitudinal AMR. There is also clearly a difference between positive and negative fields. In the positive magnetic field region between 0 mT and 4 mT, domain pinning may occur, resulting in incompletely aligned PtMn spins. This impact is diminished after annealing, while the magnitude of the longitudinal AMR is increased. The fact that the MR narrows after annealing points to a faster/smoother magnetisation reversal, i.e. less domain wall formation and pinning. This might be because of better crystallinity.
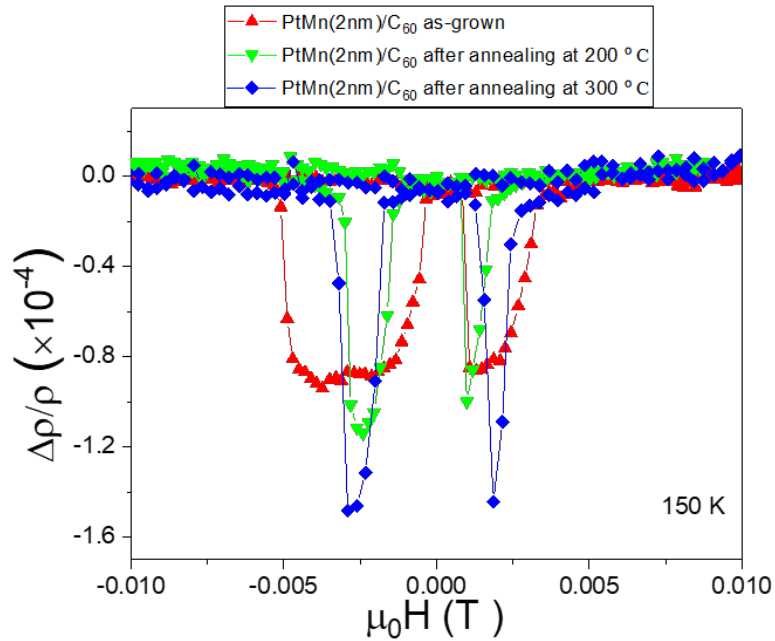
Figure 6.10: The longitudinal AMR for the same sample structure of YIG/PtMn (2 nm)/C_{60} measured before and after annealing at 150 K is shown. There is formation of domain pinning which leads to incompletely aligned PtMn spins in the positive magnetic field region between 0 mT and 4 mT.

The temperature dependence of the LF-AMR for as-grown and annealed samples is shown in figure 6.11. For two different PtMn thicknesses, the full temperature LF-AMR dependency was measured. Before annealing, the LF-AMR increases in both as the temperature rises to about 250 K. After annealing, the results show a significant improvement in the LF-AMR of up to 400 % at 100 K for PtMn (2 nm), see figure 6.11 (a). However, at high temperature this improvement drops to be even smaller than sample as grown. A thinner PtMn wire (1 nm) after annealing shows a large increase in the LF-AMR of up to one order of magnitude at 75 K, as shown in figure 6.11 (b). This MR enhancement with annealing in the thin sample (1 nm) is still present at room temperature, with a 35 % change. Therefore, we find that annealing has an effect on the thickness dependent LF-AMR. It is likely that annealing improves the $PtMn/C_{60}$ interface as the sample gets thinner. This is because the magnetised Pt region contributes more to the LF-AMR when the sample becomes thinner.
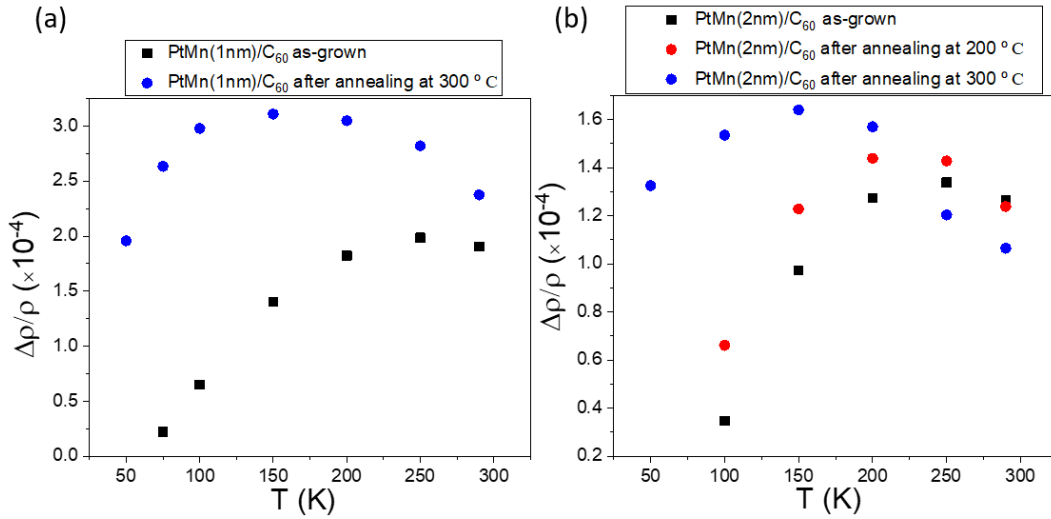
Figure 6.11: (a) and (b) display the annealing effects on $PtMn(1nm)/C_{60}$ and $PtMn(2nm)/C_{60}$ Low AMR respect to temperatures. The LF-AMR of PtMn (2nm) after annealing improved by up to 400 % at 100 K. As a result, the data suggest that annealing influences thickness dependence.

6.2.9 Conclusion

In this chapter, the results show that molecular overlayers can enhance the SHMR in the PtMn, a transition metal alloy with AFM order in bulk. The molecular layer has the greatest effect (factor 2 to 4 change) after annealing of 1 nm thick films and measuring at room temperature. This sample shows after annealing a large increase in the LF-AMR of up to one order of magnitude at 75 K. The resistivity for PtMn with C_{60} is lower than for bare PtMn wires possibly due to charge transfer and orbital re-hybridisation, contributing to the conductivity. Annealing improves the conducting hybrid interface and it reduces the contribution of polycrystalline scattering, so that PtMn/C_{60} wires may show a positive coefficient for the resistivity with temperature after annealing. TEM measurements are utilised to characterise the interfaces further and offer information on inter-diffusion and crystallinity after annealing. As we describe the influence of annealing on sample interface characteristics, the annealing process plays a significant role in our investigations.

CHAPTER 7

Conclusion and future work

7.1 Conclusion

The efficient production of pure spin currents is attracting a lot of interest because of its potential for spintronic devices. The spin Hall angle of a material is used to estimate the conversion efficiency between charge currents and pure spin currents [20; 21; 22]. Because it is associated with the torque exerted on ferromagnets, the spin Hall angle is significant in systems such as spin-transfer torque memories [23]. A larger SHMR and therefore larger spin Hall angle, can result in lower operation power and/or smaller switching currents for such devices. By tuning the SOC in conventional magnetic insulator/metal structures with a molecular layer, we can also differentiate spin transport effects based on their physical origins.

The impact of molecular overlayers on the spin Hall magnetoresistance and anisotropic magnetoresistance of heavy metals (Pt, Ta, and PtMn) has been investigated. The SHMR and AMR have been studied based on the angular dependence of the MR, considering the angles between spin vector, spin current and electrical current. A conducting layer with high SOC is formed at the interface between a heavy metal and molecules. The spin torque can be enhanced using this layer, in particular for very thin films.

As discussed in chapter 4, YIG/Pt has been widely studied. The spin Hall magnetoresistance for Pt/C_{60} at room temperature are up to a factor 6 higher than for the pristine metals, with the spin Hall angle increased by 20-60 %. At low fields of 1-30 mT, there is an anisotropic magnetoresistance, increased up to 700 % at room temperature by C_{60}. The DFT results are more closely related to the SHMR and spin-dependent scattering than the AMR, which is perhaps more linked with the induced magnetism. The Given the dielectric properties of molecules, this opens the possibility of gating the effective SOC of metals, with applications for spin transfer torque memories and pure spin current dynamic circuits. The annealing process plays a crucial part in our research as we discuss the effects of annealing on the transport properties of Pt and Pt/C_{60}. The fact that a uniaxial anisotropy is more evident or appears at higher fields in annealed samples provides some evidence for Pt-YIG magnetically active layer.

Some controversies remain, such as the origin of the AMR and the potential magnetic proximity effect, where our measurements have helped to clear out the connection between AMR (previously thought to disappear above ~150 K) and the magnetic structure of the YIG film surface.

In chapter 5, the resistance of YIG/Ta systems varies to that of YIG/Pt systems depending on magnetic field direction. We found that the Ta wires had a resistivity of (1-2 $\mu\Omega m$) and a negative temperature coefficient of (-500×$10^{-6}K^{-1}$), which is consistent with a sputtered $\beta - Ta$ phase [202]. The Ta-C$_{60}$ hybridisation points acting as scattering centres and adding to the polycrystalline. This layer contributes to the transport, but in exchange the rest of the Ta has a lower conductivity due to changes in the electronic structure. That why the linear MR in Ta was stronger for Ta/C$_{60}$ than plain Ta.

Finally, the findings of SHMR and AMR measurements of PtMn wires on YIG before and after annealing demonstrate that molecular overlayers can improve the spin orbit coupling of PtMn. The molecular layer has the greatest effect (factor 2 to 4 change) after annealing on thin films (1 nm) at room temperature. The explanation for the SHMR in PtMn/C$_{60}$ is that this might be because of increasing non-spin dependent scattering, which in turn increases the spin flip scattering event. Also, the thinner PtMn after annealing shows a large increase in the LF-AMR of up to one order of magnitude at 75 K. The annealing improves the PtMn/C$_{60}$ interface in thinner sample. This is more likely that the magnetised Pt region contributes more to the LF-AMR when the sample becomes thinner. The resistivity for PtMn with C$_{60}$ is lower than for bare PtMn wires due to charge transfer and orbital re-hybridisation, contributing to the conductivity. The TEM measurement is utilised to characterise the interfaces further and offer information on inter-diffusion after annealing.

7.2 Future Work

Uncovering how spin scattering works in molecular interfaces with high spin orbit coupling materials is still open to some interpretation and this will be topic of future work. By using synchrotron radiation techniques, the emergence of magnetic ordering [7; 213] and spin capacitance at molecular interfaces have been observed [214]. Therefore, we could use this technique to probe the spin physics in metallo-molecular interfaces on ferrimagnetic substrates via NEXAFS and XMCD (Figure 7.1). These measurements will improve our understanding of fundamental phenomena, such as spin orbit physics in hybrid interfaces, and it will open new paths in the use of molecules to tune spin transport.

The prospective measurements could include:

- Explore SOC enhancement on the PtMn layer induced by the presence of the molecular overlayers (C_{60}, MnPc) by comparing the branching ratio of Mn L3, L2 spectra in identical PtMn wires with and without the overlayers.

- Search of emergent spin and/or orbital moments in XMCD measurements at the Mn edge under magnetic fields of PtMn wires 1 mm wide and 1.5 - 5 nm thick with and without molecular overlayers. Scanning wires grown on the same YIG substrate will allow us to compare nominally identical structures, except for their top interface. Measuring the Mn edge at the PtMn/Mn-Pc interface will inform of the spilling of local spin polarisation to the molecular layer.

- XMLD measurements at the carbon K-edge will allow us to determine if the molecular orientation can play a role in the enhanced SOC.

As discussed in chapter 4, the out of plane uniaxial anisotropy observed in annealed samples needs further study. This Pt-YIG layer should be non magnetic above a certain temperature. The Néel temperature for this Pt-YIG layer has not been reported yet. At the moment, we do not knew how and when this antiferromagnetic layer forms. We have measued it on the cryostat, applying

3 T and cooling from room temperature to 5 K, but we could not invert the anisotropy. In future work, we will use SQUID with higher temperature (400 K) and magnetic field (7 T) and carry out OOP magnetometry measurements in YAG/YIG/Pt samples.
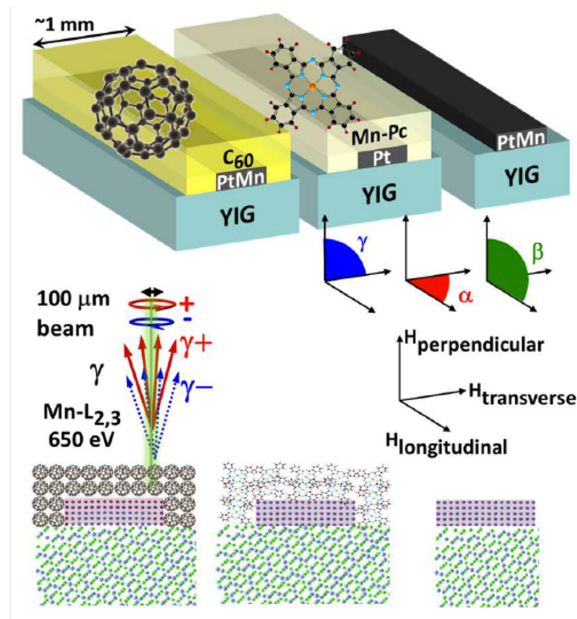
Figure 7.1: Planned XMCD mapping of samples YIG/PtMn/[C60, MnPc] vs. YIG/PtMn. Previous work shows that magnetic proximity in Pt-magnetic insulating interfaces is very weak or absent [214; 215]. In contrast with that work, we will study the spin orbit coupling of the metal with/without molecular overlayers and the spin accumulation generated during an applied current.

References

[1] V. Ivanov, T. Aminov, V. Novotortsev, and V. Kalinnikov, "Spintronics and spintronics materials," *Russian Chemical Bulletin*, vol. 53, no. 11, pp. 2357–2405, 2004. 2

[2] S. Marmion, *Comparison of Spin Hall Magnetoresistance Temperature Dependence in YIG/metal Systems.* University of Leeds (School of Physics and Astronomy), 2016. 2, 4, 20, 32, 35, 74

[3] M. Johnson and R. H. Silsbee, "Interfacial charge-spin coupling: Injection and detection of spin magnetization in metals," *Phys. Rev. Lett.*, vol. 55, pp. 1790–1793, Oct 1985. 2

[4] H. Nakayama, M. Althammer, Y.-T. Chen, K. Uchida, Y. Kajiwara, D. Kikuchi, T. Ohtani, S. Geprägs, M. Opel, S. Takahashi, R. Gross, G. E. W. Bauer, S. T. B. Goennenwein, and E. Saitoh, "Spin hall magnetoresistance induced by a nonequilibrium proximity effect," *Phys. Rev. Lett.*, vol. 110, p. 206601, May 2013. xi, 2, 4, 8, 14, 17, 57

[5] Y.-T. Chen, S. Takahashi, H. Nakayama, M. Althammer, S. T. Goennenwein, E. Saitoh, and G. E. Bauer, "Theory of spin hall magnetoresistance," *Physical Review B*, vol. 87, no. 14, p. 144411, 2013. 2, 15, 57, 76

[6] M. Althammer, S. Meyer, H. Nakayama, M. Schreier, S. Altmannshofer, M. Weiler, H. Huebl, S. Geprägs, M. Opel, R. Gross, *et al.*, "Quantitative study of the spin hall magnetoresistance in ferromagnetic insulator/normal metal hybrids," *Physical Review B*, vol. 87, no. 22, p. 224401, 2013. xviii, 2, 14, 16, 23, 58, 60, 78

[7] F. Al MaMari, T. Moorsom, G. Teobaldi, W. Deacon, T. Prokscha, H. Luetkens, S. Lee, G. E. Sterbinsky, D. A. Arena, D. A. MacLaren, *et al.*, "Beating the stoner criterion using molecular interfaces," *Nature*, vol. 524, no. 7563, pp. 69–73, 2015. 2, 124

[8] M. Cinchetti, V. A. Dediu, and L. E. Hueso, "Activating the molecular spinterface," *Nature materials*, vol. 16, no. 5, p. 507, 2017. 2, 25

[9] F. Hellman, A. Hoffmann, Y. Tserkovnyak, G. S. Beach, E. E. Fullerton, C. Leighton, A. H. MacDonald, D. C. Ralph, D. A. Arena, H. A. Dürr, *et al.*, "Interface-induced phenomena in magnetism," *Reviews of modern physics*, vol. 89, no. 2, p. 025006, 2017. 2

[10] L. E. Hueso, J. M. Pruneda, V. Ferrari, G. Burnell, J. P. Valdes-Herrera, B. D. Simons, P. B. Littlewood, E. Artacho, A. Fert, and N. D. Mathur, "Transformation of spin information into large electrical signals using carbon nanotubes," *Nature*, vol. 445, no. 7126, pp. 410–413, 2007. 2

[11] J. Liu, F.-C. Zhang, and K. Law, "Majorana fermion induced nonlocal current correlations in spin-orbit coupled superconducting wires," *Physical Review B*, vol. 88, no. 6, p. 064509, 2013. 2

[12] W.-J. Shi, J. Liu, Y. Xu, S.-J. Xiong, J. Wu, and W. Duan, "Converting normal insulators into topological insulators via tuning orbital levels," *Physical Review B*, vol. 92, no. 20, p. 205118, 2015. 2

[13] J. Sinova, S. O. Valenzuela, J. Wunderlich, C. Back, and T. Jungwirth, "Spin hall effects," *Reviews of Modern Physics*, vol. 87, no. 4, p. 1213, 2015. 2, 46

[14] G. Daalderop, P. Kelly, and M. Schuurmans, "First-principles calculation of the magnetocrystalline anisotropy energy of iron, cobalt, and nickel," *Physical Review B*, vol. 41, no. 17, p. 11919, 1990. 3

[15] T. B. Noack, H. Y. Musiienko-Shmarova, T. Langner, F. Heussner, V. Lauer, B. Heinz, D. A. Bozhko, V. I. Vasyuchka, A. Pomyalov, V. S. Lvov, *et al.*, "Spin seebeck effect and ballistic transport of quasi-acoustic magnons in room-temperature yttrium iron garnet films," *Journal of Physics D: Applied Physics*, vol. 51, no. 23, p. 234003, 2018. 3, 8

[16] K. Uchida, J. Xiao, H. Adachi, J.-i. Ohe, S. Takahashi, J. Ieda, T. Ota, Y. Kajiwara, H. Umezawa, H. Kawai, *et al.*, "Spin seebeck insulator," *Nature materials*, vol. 9, no. 11, p. 894, 2010. 3, 8

[17] R. Das, V. Kalappattil, R. Geng, H. Luong, M. Pham, T. Nguyen, T. Liu, M. Wu, M. Phan, and H. Srikanth, "Enhanced room-temperature spin seebeck effect in a yig/c60/pt layered heterostructure," *AIP Advances*, vol. 8, no. 5, p. 055906, 2018. 3, 8

[18] S. Alotibi, B. J. Hickey, G. Teobaldi, M. Ali, J. Barker, E. Poli, D. D. ORegan, Q. Ramasse, G. Burnell, J. Patchett, *et al.*, "Enhanced spin–orbit coupling in heavy metals via molecular coupling," *ACS Applied Materials & Interfaces*, vol. 13, no. 4, pp. 5228–5234, 2021. 3, 51, 70, 76, 78

[19] M.-G. Kang, J.-G. Choi, J. Jeong, J. Y. Park, H.-J. Park, J. M. Yuk, K.-J. Lee, and B.-G. Park, "Electric-field control of field-free spin-orbit torque switching via laterally modulated rashba effect in pt/co/alox structures," 2020. 3

[20] J. Wunderlich, B. Kaestner, J. Sinova, and T. Jungwirth, "Experimental observation of the spin-hall effect in a two-dimensional spin-orbit coupled semiconductor system," *Physical review letters*, vol. 94, no. 4, p. 047204, 2005. 3, 122

[21] M. Isasa, E. Villamor, L. E. Hueso, M. Gradhand, and F. Casanova, "Temperature dependence of spin diffusion length and spin hall angle in au and pt," *Physical Review B*, vol. 91, no. 2, p. 024402, 2015. 3, 122

[22] D. Qu, S. Huang, B. Miao, S. Huang, and C. Chien, "Self-consistent determination of spin hall angles in selected 5 d metals by thermal spin injection," *Physical Review B*, vol. 89, no. 14, p. 140407, 2014. 3, 122

[23] L. Liu, T. Moriyama, D. Ralph, and R. Buhrman, "Spin-torque ferromagnetic resonance induced by the spin hall effect," *Physical review letters*, vol. 106, no. 3, p. 036601, 2011. 3, 122

[24] Y. Lu, Y. Choi, C. Ortega, X. Cheng, J. Cai, S. Huang, L. Sun, and C. Chien, "Pt magnetic polarization on y 3 fe 5 o 12 and magnetotransport characteristics," *Physical review letters*, vol. 110, no. 14, p. 147207, 2013. 3, 20, 21, 22, 50, 65

[25] S. Geprägs, S. Meyer, S. Altmannshofer, M. Opel, F. Wilhelm, A. Rogalev, R. Gross, and S. T. Goennenwein, "Investigation of induced pt magnetic polarization in pt/y3fe5o12 bilayers," *Applied Physics Letters*, vol. 101, no. 26, p. 262407, 2012. 3, 20, 22, 65

[26] T. D. Nguyen, G. Hukic-Markosian, F. Wang, L. Wojcik, X.-G. Li, E. Ehrenfreund, and Z. V. Vardeny, "Isotope effect in spin response of π-conjugated polymer films and devices," *Nature materials*, vol. 9, no. 4, p. 345, 2010. 3

[27] X. Zhang, S. Mizukami, T. Kubota, Q. Ma, M. Oogane, H. Naganuma, Y. Ando, and T. Miyazaki, "Observation of a large spin-dependent transport length in organic spin valves at room temperature," *Nature Communications*, vol. 4, p. 1392, 2013. 3, 10

[28] T.-H. Chuang, K.-T. Lu, C.-I. Lu, Y.-J. Hsu, and D.-H. Wei, "Hybridization regulated metal penetration at transition metal-organic semiconductor contacts," *Applied Physics Letters*, vol. 112, no. 8, p. 081601, 2018. 3

[29] L. Guo, X. Gu, X. Zhu, and X. Sun, "Recent advances in molecular spintronics: Multifunctional spintronic devices," *Advanced Materials*, vol. 31, no. 45, p. 1805355, 2019. 3

[30] Y. Zhang, L. Guo, X. Zhu, and X. Sun, "The application of organic semiconductor materials in spintronics," *Frontiers in Chemistry*, vol. 8, p. 965, 2020. 3

[31] B. Heinrich, C. Burrowes, E. Montoya, B. Kardasz, E. Girt, Y.-Y. Song, Y. Sun, and M. Wu, "Spin pumping at the magnetic insulator (yig)/normal metal (au) interfaces," *Phys. Rev. Lett.*, vol. 107, p. 066604, Aug 2011. 4, 8

[32] F. Yang and P. C. Hammel, "Fmr-driven spin pumping in y3fe5o12-based structures," *Journal of Physics D: Applied Physics*, vol. 51, no. 25, p. 253001, 2018. 4, 8

[33] S. Emori, A. Matyushov, H.-M. Jeon, C. J. Babroski, T. Nan, A. M. Belkessam, J. G. Jones, M. E. McConney, G. J. Brown, B. M. Howe, *et al.*, "Spin-orbit torque and spin pumping in yig/pt with interfacial insertion layers," *Applied Physics Letters*, vol. 112, no. 18, p. 182406, 2018. 4, 8

[34] Y. Tserkovnyak, A. Brataas, and G. E. Bauer, "Enhanced gilbert damping in thin ferromagnetic films," *Physical review letters*, vol. 88, no. 11, p. 117601, 2002. 4

[35] J. Sinova, S. O. Valenzuela, J. Wunderlich, C. H. Back, and T. Jungwirth, "Spin hall effects," *Rev. Mod. Phys.*, vol. 87, pp. 1213–1260, Oct 2015. 4

[36] J. Hirsch, "Spin hall effect," *Physical Review Letters*, vol. 83, no. 9, p. 1834, 1999. 4, 11

[37] P. Anderson, "Theory of superexchange interaction," *Physical Review*, vol. 79, no. 2, p. 350, 1950. 8

[38] X. Jia, K. Liu, K. Xia, and G. E. Bauer, "Spin transfer torque on magnetic insulators," *EPL (Europhysics Letters)*, vol. 96, no. 1, p. 17005, 2011. 8

[39] A. G. Gurevich and G. A. Melkov, *Magnetization oscillations and waves.* CRC press, 1996. 8

[40] S. O. Demokritov, V. E. Demidov, O. Dzyapko, G. A. Melkov, A. A. Serga, B. Hillebrands, and A. N. Slavin, "Bose–einstein condensation of quasi-equilibrium magnons at room temperature under pumping," *Nature*, vol. 443, no. 7110, pp. 430–433, 2006. 8

[41] R. Behrisch and W. Eckstein, *Sputtering by particle bombardment: experiments and computer calculations from threshold to MeV energies*, vol. 110. Springer Science & Business Media, 2007. 8

[42] J. A. Thornton, "Magnetron sputtering: basic physics and application to cylindrical magnetrons," *Journal of Vacuum Science and Technology*, vol. 15, no. 2, pp. 171–177, 1978. 8

[43] B. F. Miao, S. Y. Huang, D. Qu, and C. L. Chien, "Physical origins of the new magnetoresistance in Pt/YIG," *Phys. Rev. Lett.*, vol. 112, p. 236601, Jun 2014. 8

[44] S. R. Marmion, M. Ali, M. McLaren, D. A. Williams, and B. J. Hickey, "Temperature dependence of spin hall magnetoresistance in thin yig/pt films," *Phys. Rev. B*, vol. 89, p. 220404, Jun 2014. 8, 18, 35, 85

[45] S. Geprägs, C. Klewe, S. Meyer, D. Graulich, F. Schade, M. Schneider, S. Francoual, S. P. Collins, K. Ollefs, F. Wilhelm, *et al.*, "Static magnetic proximity effects and spin hall magnetoresistance in pt/y 3 fe 5 o 12 and inverted y 3 fe 5 o 12/pt bilayers," *Physical Review B*, vol. 102, no. 21, p. 214438, 2020. 8, 16, 22

[46] R. Yadav, M. Shepit, X. Li, K.-W. Lin, J. van Lierop, and A. Ruotolo, "Photo-spin-voltaic effect in ptmn/y3fe5o12 thin films," *Journal of Physics: Condensed Matter*, vol. 33, no. 9, p. 095802, 2020. 8

[47] G. Ogsen, *Magneto-optical thin films for magnetic fields visualization.* PhD thesis, Yerevan State University, 2015. xi, 9

[48] H. W. Kroto, J. R. Heath, S. C. OBrien, R. F. Curl, and R. E. Smalley, "C 60: buckminsterfullerene," *nature*, vol. 318, no. 6042, pp. 162–163, 1985. 9

[49] W. Krätschmer, "Fullerenes and fullerites: new forms of carbon," *Nanostructured Materials*, vol. 6, no. 1-4, pp. 65–72, 1995. 9

[50] H. Kroto, J. Heath, S. Obrien, R. Curl, and R. Smalley, "Long carbon chain molecules in circumstellar shells," *The Astrophysical Journal*, vol. 314, pp. 352–355, 1987. 9

[51] J. Robertson, "Diamond-like amorphous carbon," *Materials Science and Engineering: R: Reports*, vol. 37, no. 4-6, pp. 129–281, 2002. xi, 9, 11

[52] D. Sun, K. J. Van Schooten, M. Kavand, H. Malissa, C. Zhang, M. Groes-beck, C. Boehme, and Z. V. Vardeny, "Inverse spin hall effect from pulsed spin current in organic semiconductors with tunable spin–orbit coupling," *Nature materials*, vol. 15, no. 8, p. 863, 2016. 9, 10

[53] S. Liang, R. Geng, B. Yang, W. Zhao, R. C. Subedi, X. Li, X. Han, and T. D. Nguyen, "Curvature-enhanced spin-orbit coupling and spinterface effect in fullerene-based spin valves," *Scientific reports*, vol. 6, p. 19461, 2016. 9

[54] S. Leach, M. Vervloet, A. Després, E. Bréheret, J. P. Hare, T. J. Dennis, H. W. Kroto, R. Taylor, and D. R. Walton, "Electronic spectra and transitions of the fullerene c60," *Chemical Physics*, vol. 160, no. 3, pp. 451–466, 1992. xi, 10

[55] B. Mishori, E. Katz, D. Faiman, A. Belu-Marian, and Y. Shapira, "Electronic properties of c60 thin films," *Fullerene science and technology*, vol. 6, no. 1, pp. 113–124, 1998. 10

[56] T. Ohno, Y. Chen, S. Harvey, G. Kroll, J. Weaver, R. Haufler, and R. Smalley, "C 60 bonding and energy-level alignment on metal and semiconductor surfaces," *Physical Review B*, vol. 44, no. 24, p. 13747, 1991. 10, 28

[57] S. Braun, W. R. Salaneck, and M. Fahlman, "Energy-level alignment at organic/metal and organic/organic interfaces," *Advanced materials*, vol. 21, no. 14-15, pp. 1450–1472, 2009. 10

[58] M. Gobbi, F. Golmar, R. Llopis, F. Casanova, and L. E. Hueso, "Room-temperature spin transport in c60-based spin valves," *Advanced Materials*, vol. 23, no. 14, pp. 1609–1613, 2011. 10

[59] X. Zhang, S. Mizukami, Q. Ma, T. Kubota, M. Oogane, H. Naganuma, Y. Ando, and T. Miyazaki, "Spin-dependent transport behavior in c60 and alq3 based spin valves with a magnetite electrode," *Journal of Applied Physics*, vol. 115, no. 17, p. 172608, 2014. 10

[60] R. Lin, F. Wang, M. Wohlgenannt, C. He, X. Zhai, and Y. Suzuki, "Organic spin-valves based on fullerene c60," *Synthetic Metals*, vol. 161, no. 7-8, pp. 553–557, 2011. 10

[61] T. Tran, T. Q. Le, J. G. Sanderink, W. G. van der Wiel, and M. P. de Jong, "The multistep tunneling analogue of conductivity mismatch in organic spin valves," *Advanced functional materials*, vol. 22, no. 6, pp. 1180–1189, 2012. 10

[62] Ï. J. Christenson *et al.*, "Possibility of orienting electron spins with current," *Phys. Rev. Lett*, vol. 25, p. 3l6, 1970. 11

[63] M. I. Dyakonov and V. Perel, "Current-induced spin orientation of electrons in semiconductors," *Physics Letters A*, vol. 35, no. 6, pp. 459–460, 1971. 11

[64] S. Zhang, "Spin hall effect in the presence of spin diffusion," *Physical review letters*, vol. 85, no. 2, p. 393, 2000. 11

[65] F. D. Czeschka, *Spin currents in metallic nanostructures*. PhD thesis, Technische Universität München, 2011. 11

[66] S. Takahashi and S. Maekawa, "Spin current, spin accumulation and spin hall effect," *Science and Technology of Advanced Materials*, vol. 9, no. 1, p. 014105, 2008. 12

[67] N. F. Mott, "The scattering of fast electrons by atomic nuclei," *Proceedings of the Royal Society of London. Series A, Containing Papers of a Mathematical and Physical Character*, vol. 124, no. 794, pp. 425–442, 1929. 12

[68] L. Berger, "Side-jump mechanism for the hall effect of ferromagnets," *Physical Review B*, vol. 2, no. 11, p. 4559, 1970. 12

[69] O.-O. INYANG *et al.*, *Magnetic proximity effect and interfacial spin dependent transport in ferromagnet/heavy metal thin films*. PhD thesis, Durham University, 2018. xi, xii, 13, 21

[70] J. Smit, "The spontaneous hall effect in ferromagnetics ii," *Physica*, vol. 24, no. 1-5, pp. 39–51, 1958. 13

[71] G. Vignale, "Ten years of spin hall effect," *Journal of superconductivity and novel magnetism*, vol. 23, no. 1, p. 3, 2010. 13

[72] A. Fert and P. M. Levy, "Spin hall effect induced by resonant scattering on impurities in metals," *Physical review letters*, vol. 106, no. 15, p. 157208, 2011. 14

[73] A. Azevedo, L. Vilela Leão, R. Rodriguez-Suarez, A. Oliveira, and S. Rezende, "dc effect in ferromagnetic resonance: Evidence of the spin-pumping effect?," *Journal of applied physics*, vol. 97, no. 10, p. 10C715, 2005. 14

[74] L. Liu, C.-F. Pai, Y. Li, H. Tseng, D. Ralph, and R. Buhrman, "Spin-torque switching with the giant spin hall effect of tantalum," *Science*, vol. 336, no. 6081, pp. 555–558, 2012. 14, 91

[75] C.-F. Pai, L. Liu, Y. Li, H. Tseng, D. Ralph, and R. Buhrman, "Spin transfer torque devices utilizing the giant spin hall effect of tungsten," *Applied Physics Letters*, vol. 101, no. 12, p. 122404, 2012. 14

[76] H. Wang, C. Du, Y. Pu, R. Adur, P. C. Hammel, and F. Yang, "Scaling of spin hall angle in 3d, 4d, and 5d metals from y 3 fe 5 o 12/metal spin pumping," *Physical review letters*, vol. 112, no. 19, p. 197201, 2014. 14

[77] A. Ganguly, R. Rowan-Robinson, A. Haldar, S. Jaiswal, J. Sinha, A. Hindmarch, D. Atkinson, and A. Barman, "Time-domain detection of current controlled magnetization damping in pt/ni81fe19 bilayer and determination of pt spin hall angle," *Applied Physics Letters*, vol. 105, no. 11, p. 112409, 2014. 14

[78] C. Hahn, G. De Loubens, O. Klein, M. Viret, V. V. Naletov, and J. B. Youssef, "Comparative measurements of inverse spin hall effects and magnetoresistance in yig/pt and yig/ta," *Physical Review B*, vol. 87, no. 17, p. 174417, 2013. 14, 61, 91

[79] V. Vlaminck, J. E. Pearson, S. D. Bader, and A. Hoffmann, "Dependence of spin-pumping spin hall effect measurements on layer thicknesses and stacking order," *Physical Review B*, vol. 88, no. 6, p. 064414, 2013. 14

[80] W. Zhang, V. Vlaminck, J. E. Pearson, R. Divan, S. D. Bader, and A. Hoffmann, "Determination of the pt spin diffusion length by spin-pumping and spin hall effect," *Applied physics letters*, vol. 103, no. 24, p. 242414, 2013. 14

[81] W. Zhang, W. Han, X. Jiang, S.-H. Yang, and S. S. Parkin, "Role of transparency of platinum–ferromagnet interfaces in determining the intrinsic magnitude of the spin hall effect," *Nature Physics*, vol. 11, no. 6, pp. 496–502, 2015. 14, 23

[82] J. Gómez, B. Z. Tedlla, N. Álvarez, G. Alejandro, E. Goovaerts, and A. Butera, "Spin transport parameters in ni 80 fe 20/ru and ni 80 fe 20/ta bilayers," *Physical Review B*, vol. 90, no. 18, p. 184401, 2014. 14

[83] Y. Kajiwara, K. Harii, S. Takahashi, J. Ohe, K. Uchida, M. Mizuguchi, H. Umezawa, H. Kawai, K. Ando, K. Takanashi, S. Maekawa, and E. Saitoh, "Transmission of electrical signals by spin-wave interconversion in a magnetic insulator.nature, 464:262?266, 2010," *Journal*, 2010. 15

[84] V. E. Demidov, S. Urazhdin, H. Ulrichs, V. Tiberkevich, A. Slavin, D. Baither, G. Schmitz, and S. O. Demokritov, "Magnetic nano-oscillator driven by pure spin current," *Nature materials*, vol. 11, no. 12, p. 1028, 2012. 16

[85] A. Awad, P. Dürrenfeld, A. Houshang, M. Dvornik, E. Iacocca, R. Dumas, and J. Åkerman, "Long-range mutual synchronization of spin hall nano-oscillators," *Nature Physics*, vol. 13, no. 3, p. 292, 2017. 16

[86] I. Borisenko, V. Demidov, S. Urazhdin, A. Rinkevich, and S. Demokritov, "Relation between unidirectional spin hall magnetoresistance and spin current-driven magnon generation," *arXiv preprint arXiv:1806.06581*, 2018. 16

[87] B. Miao, S. Huang, D. Qu, and C. Chien, "Physical origins of the new magnetoresistance in pt/yig," *Physical review letters*, vol. 112, no. 23, p. 236601, 2014. 16

[88] Y. Shiomi, T. Ohtani, S. Iguchi, T. Sasaki, Z. Qiu, H. Nakayama, K. Uchida, and E. Saitoh, "Interface-dependent magnetotransport properties for thin pt films on ferrimagnetic y3fe5o12," *Applied Physics Letters*, vol. 104, no. 24, p. 242406, 2014. 16, 54

[89] J.-G. Choi, J. W. Lee, and B.-G. Park, "Spin hall magnetoresistance in heavy-metal/metallic-ferromagnet multilayer structures," *Physical Review B*, vol. 96, no. 17, p. 174412, 2017. 16

[90] S.-Y. Huang, H.-L. Li, C.-W. Chong, Y.-Y. Chang, M.-K. Lee, *et al.*, "Interface-induced spin hall magnetoresistance enhancement in pt-based tri-layer structure," *Scientific reports*, vol. 8, no. 1, p. 108, 2018. 17

[91] S. Vélez, V. N. Golovach, A. Bedoya-Pinto, M. Isasa, E. Sagasta, M. Abadia, C. Rogero, L. E. Hueso, F. S. Bergeret, and F. Casanova, "Hanle magnetoresistance in thin metal films with strong spin-orbit coupling," *Phys. Rev. Lett.*, vol. 116, p. 016603, Jan 2016. 18, 54, 55, 61, 109

[92] S. Meyer, M. Althammer, S. Geprägs, M. Opel, R. Gross, and S. T. Goennenwein, "Temperature dependent spin transport properties of platinum inferred from spin hall magnetoresistance measurements," *Applied Physics Letters*, vol. 104, no. 24, p. 242411, 2014. xi, 18, 19, 50, 58, 84

[93] H. Wu, X. Zhang, C. Wan, B. Tao, L. Huang, W. Kong, and X. Han, "Hanle magnetoresistance: The role of edge spin accumulation and interfacial spin current," *Physical Review B*, vol. 94, no. 17, p. 174407, 2016. xi, 18, 19, 58, 61

[94] Y.-T. Chen, S. Takahashi, H. Nakayama, M. Althammer, S. T. Goennenwein, E. Saitoh, and G. E. Bauer, "Theory of spin hall magnetoresistance (smr) and related phenomena," *Journal of Physics: Condensed Matter*, vol. 28, no. 10, p. 103004, 2016. 18, 60

[95] Y. Yafet and V. Jaccarino, "Nuclear spin relaxation in transition metals; core polarization," *Physical Review*, vol. 133, no. 6A, p. A1630, 1964. 18

[96] J. Smit, "Magnetoresistance of ferromagnetic metals and alloys at low temperatures," *Physica*, vol. 17, no. 6, pp. 612–627, 1951. 19

[97] T. McGuire and R. Potter, "Anisotropic magnetoresistance in ferromagnetic 3d alloys," *IEEE Transactions on Magnetics*, vol. 11, no. 4, pp. 1018–1038, 1975. 19, 20

[98] S. Blundell, "Magnetism in condensed matter," *American Association of Physics Teachers*, 2003. 19, 20

[99] Y. Lu, J. Cai, S. Huang, D. Qu, B. Miao, and C. Chien, "Hybrid magnetoresistance in the proximity of a ferromagnet," *Physical Review B*, vol. 87, no. 22, p. 220409, 2013. 20

[100] F. Hoare and J. Matthews, "The magnetic susceptibilities of platinum, rhodium and palladium from 20 to 290 k," *Proceedings of the Royal Society of London. Series A. Mathematical and Physical Sciences*, vol. 212, no. 1108, pp. 137–148, 1952. 21

[101] S.-Y. Huang, X. Fan, D. Qu, Y. Chen, W. Wang, J. Wu, T. Chen, J. Xiao, and C. Chien, "Transport magnetic proximity effects in platinum," *Physical review letters*, vol. 109, no. 10, p. 107204, 2012. 21, 22

[102] T. Kikkawa, M. Suzuki, J. Okabayashi, K.-i. Uchida, D. Kikuchi, Z. Qiu, and E. Saitoh, "Detection of induced paramagnetic moments in pt on y 3 fe 5 o 12 via x-ray magnetic circular dichroism," *Physical Review B*, vol. 95, no. 21, p. 214416, 2017. 21

[103] T. Lin, C. Tang, H. M. Alyahayaei, and J. Shi, "Experimental investigation of the nature of the magnetoresistance effects in pd-yig hybrid structures," *Phys. Rev. Lett.*, vol. 113, p. 037203, Jul 2014. 22, 72

[104] S. Vélez, A. Bedoya-Pinto, W. Yan, L. E. Hueso, and F. Casanova, "Competing effects at pt/yig interfaces: Spin hall magnetoresistance, magnon excitations, and magnetic frustration," *Phys. Rev. B*, vol. 94, p. 174405, Nov 2016. 22

[105] J. J. Hauser, "Magnetic proximity effect," *Phys. Rev.*, vol. 187, pp. 580–583, Nov 1969. 22

[106] W. J. Antel, M. M. Schwickert, T. Lin, W. L. O'Brien, and G. R. Harp, "Induced ferromagnetism and anisotropy of pt layers in fe/pt(001) multilayers," *Phys. Rev. B*, vol. 60, pp. 12933–12940, Nov 1999. 22

[107] M. Weiler, M. Althammer, F. D. Czeschka, H. Huebl, M. S. Wagner, M. Opel, I.-M. Imort, G. Reiss, A. Thomas, R. Gross, and S. T. B. Goennenwein, "Local charge and spin currents in magnetothermal landscapes," *Phys. Rev. Lett.*, vol. 108, p. 106602, Mar 2012. 22

[108] A. Manchon, H. C. Koo, J. Nitta, S. Frolov, and R. Duine, "New perspectives for rashba spin–orbit coupling," *Nature materials*, vol. 14, no. 9, pp. 871–882, 2015. 22

[109] R. ROWAN-ROBINSON, *Spin-orbit phenomena and interfacial proximity effects in magnetic multilayers.* PhD thesis, Durham University, 2016. xii, 23, 24

[110] V. L. Grigoryan, W. Guo, G. E. Bauer, J. Xiao, *et al.*, "Intrinsic magnetoresistance in metal films on ferromagnetic insulators," *Physical Review B*, vol. 90, no. 16, p. 161412, 2014. 23

[111] M. Isasa, A. Bedoya-Pinto, S. Vélez, F. Golmar, F. Sánchez, L. E. Hueso, J. Fontcuberta, and F. Casanova, "Spin hall magnetoresistance at pt/cofe2o4 interfaces and texture effects," *Applied Physics Letters*, vol. 105, no. 14, p. 142402, 2014. 23

[112] J. Kim, J. Sinha, M. Hayashi, M. Yamanouchi, S. Fukami, T. Suzuki, S. Mitani, and H. Ohno, "Layer thickness dependence of the current-induced effective field vector in ta— cofeb— mgo," *Nature materials*, vol. 12, no. 3, pp. 240–245, 2013. 23

[113] M. Isasa, M. C. Martínez-Velarte, E. Villamor, C. Magén, L. Morellón, J. M. De Teresa, M. R. Ibarra, G. Vignale, E. V. Chulkov, E. E. Krasovskii, *et al.*, "Origin of inverse rashba-edelstein effect detected at the cu/bi interface using lateral spin valves," *Physical Review B*, vol. 93, no. 1, p. 014420, 2016. 23

[114] R. Friedrich, V. Caciuc, G. Bihlmayer, N. Atodiresei, and S. Blügel, "Designing the rashba spin texture by adsorption of inorganic molecules," *New Journal of Physics*, vol. 19, no. 4, p. 043017, 2017. 23

[115] S. Jakobs, A. Narayan, B. Stadtmller, A. Droghetti, I. Rungger, Y. S. Hor, S. Klyatskaya, D. Jungkenn, J. Stckl, M. Laux, *et al.*, "Controlling the spin texture of topological insulators by rational design of organic molecules," *Nano letters*, vol. 15, no. 9, pp. 6022–6029, 2015. 23

[116] J. R. Sánchez, L. Vila, G. Desfonds, S. Gambarelli, J. Attané, J. De Teresa, C. Magén, and A. Fert, "Spin-to-charge conversion using rashba coupling at the interface between non-magnetic materials," *Nature communications*, vol. 4, no. 1, pp. 1–7, 2013. 23

[117] S. Sanvito, "Molecular spintronics: The rise of spinterface science," *Nature Physics*, vol. 6, no. 8, p. 562, 2010. xii, 25, 26, 27

[118] V. A. Dediu, "Organic spintronics: Inside the interface," *Nature Physics*, vol. 9, no. 4, p. 210, 2013. 25

[119] M. S. Ferreira and S. Sanvito, "Contact-induced spin polarization in carbon nanotubes," *Physical Review B*, vol. 69, no. 3, p. 035407, 2004. 25

[120] O. Céspedes, M. Ferreira, S. Sanvito, M. Kociak, and J. Coey, "Contact induced magnetism in carbon nanotubes," *Journal of Physics: Condensed Matter*, vol. 16, no. 10, p. L155, 2004. 25

[121] C. Barraud, P. Seneor, R. Mattana, S. Fusil, K. Bouzehouane, C. Deranlot, P. Graziosi, L. Hueso, I. Bergenti, V. Dediu, *et al.*, "Unravelling the role of the interface for spin injection into organic semiconductors," *Nature Physics*, vol. 6, no. 8, p. 615, 2010. 25

[122] M. Galbiati, S. Tatay, C. Barraud, A. V. Dediu, F. Petroff, R. Mattana, and P. Seneor, "Spinterface: Crafting spintronics at the molecular scale," *Mrs Bulletin*, vol. 39, no. 7, pp. 602–607, 2014. 25

[123] S. Steil, N. Großmann, M. Laux, A. Ruffing, D. Steil, M. Wiesenmayer, S. Mathias, O. L. Monti, M. Cinchetti, and M. Aeschlimann, "Spin-dependent trapping of electrons at spinterfaces," *Nature Physics*, vol. 9, no. 4, p. 242, 2013. 25

[124] N. Baadji and S. Sanvito, "Giant resistance change across the phase transition in spin-crossover molecules," *Physical review letters*, vol. 108, no. 21, p. 217201, 2012. 25

[125] D. Cakır, D. M. Otálvaro, and G. Brocks, "From spin-polarized interfaces to giant magnetoresistance in organic spin valves," *Physical Review B*, vol. 89, no. 11, p. 115407, 2014. 25

[126] P. Amsalem, J. Niederhausen, A. Wilke, G. Heimel, R. Schlesinger, S. Winkler, A. Vollmer, J. Rabe, and N. Koch, "Role of charge transfer, dipole-dipole interactions, and electrostatics in fermi-level pinning at a molecular heterojunction on a metal surface," *Physical Review B*, vol. 87, no. 3, p. 035440, 2013. 26

[127] R. T. Tung, "Chemical bonding and fermi level pinning at metal-semiconductor interfaces," *Physical review letters*, vol. 84, no. 26, p. 6078, 2000. 28

[128] A. Maxwell, P. Brühwiler, D. Arvanitis, J. Hasselström, and N. Mårtensson, "C 1s ionisation potential and energy referencing for solid c60 films on metal surfaces," *Chemical physics letters*, vol. 260, no. 1-2, pp. 71–77, 1996. 28

[129] R. Lof, M. Van Veenendaal, B. Koopmans, H. Jonkman, and G. Sawatzky, "Band gap, excitons, and coulomb interaction in solid c 60," *Physical review letters*, vol. 68, no. 26, p. 3924, 1992. 28

[130] A. Maxwell, P. Brühwiler, A. Nilsson, N. Mårtensson, and P. Rudolf, "Photoemission, autoionization, and x-ray-absorption spectroscopy of ultrathin-film c 60 on au (110)," *Physical Review B*, vol. 49, no. 15, p. 10717, 1994. 28

[131] T. Moorsom, *Electron transfer and spin injection in C60-ferromagnetic composites*. PhD thesis, University of Leeds, 2016. xii, 29

[132] M. Grundmann, "Kramers–kronig relations," in *The Physics of Semiconductors*, pp. 775–776, Springer, 2010. 30

[133] S. Sze and K. K. Ng, "Photodetectors and solar cells," *Physics of semiconductor devices*, pp. 663–742, 2007. 30

[134] M. Salkola, "Intermolecular polaron and bipolaron tunneling in c 60," *Physical Review B*, vol. 49, no. 14, p. 9533, 1994. 30

[135] N. Mott, "On metal-insulator transitions," *Journal of Solid State Chemistry*, vol. 88, no. 1, pp. 5–7, 1990. 30

[136] S. Sanvito, "Molecular spintronics," *Chemical Society Reviews*, vol. 40, no. 6, pp. 3336–3355, 2011. 30

[137] K. V. Raman, A. M. Kamerbeek, A. Mukherjee, N. Atodiresei, T. K. Sen, P. Lazić, V. Caciuc, R. Michel, D. Stalke, S. K. Mandal, *et al.*, "Interface-engineered templates for molecular spin memory devices," *Nature*, vol. 493, no. 7433, p. 509, 2013. 30

[138] K. Bairagi, A. Bellec, V. Repain, C. Chacon, Y. Girard, Y. Garreau, J. Lagoute, S. Rousset, R. Breitwieser, Y.-C. Hu, *et al.*, "Tuning the magnetic anisotropy at a molecule-metal interface," *Physical review letters*, vol. 114, no. 24, p. 247203, 2015. 30, 67

[139] T. L. A. Tran, P. K. J. Wong, M. P. de Jong, W. G. van der Wiel, Y. Zhan, and M. Fahlman, "Hybridization-induced oscillatory magnetic polarization of c 60 orbitals at the c 60/fe (001) interface," *Applied physics letters*, vol. 98, no. 22, p. 222505, 2011. 30

[140] T. Moorsom, M. Wheeler, T. M. Khan, F. Al MaMari, C. Kinane, S. Langridge, A. Bedoya-Pinto, L. Hueso, G. Teobaldi, V. K. Lazarov, *et al.*, "Spin-polarized electron transfer in ferromagnet/c 60 interfaces," *Physical Review B*, vol. 90, no. 12, p. 125311, 2014. 30

[141] T. L. A. Tran, "Spintronics using c60 fullerenes: Interface and devices," 2013. 30

[142] H. Vázquez, R. Oszwaldowski, P. Pou, J. Ortega, R. Pérez, F. Flores, and A. Kahn, "Dipole formation at metal/ptcda interfaces: role of the charge neutrality level," *EPL (Europhysics Letters)*, vol. 65, no. 6, p. 802, 2004. 30

[143] M. L. Perrin, C. J. Verzijl, C. A. Martin, A. J. Shaikh, R. Eelkema, J. H. Van Esch, J. M. Van Ruitenbeek, J. M. Thijssen, H. S. Van Der Zant, and D. Dulić, "Large tunable image-charge effects in single-molecule junctions," *Nature nanotechnology*, vol. 8, no. 4, p. 282, 2013. 30

[144] K. Wasa, M. Kitabatake, and H. Adachi, *Thin film materials technology: sputtering of control compound materials.* Springer Science & Business Media, 2004. 32

[145] K. Ellmer, "Magnetron sputtering of transparent conductive zinc oxide: relation between the sputtering parameters and the electronic properties," *Journal of Physics D: Applied Physics*, vol. 33, no. 4, p. R17, 2000. 32

[146] A. MaMari and F. A. Salim, *Emergent Spin Ordering at C60 interfaces.* PhD thesis, University of Leeds, 2016. 34

[147] M. C. Wheeler, *Manipulation of fullerene C60 spintronic devices via ferromagnetic resonance.* PhD thesis, University of Leeds, 2014. xiii, 34, 38

[148] R. Gupta, A. Tayal, S. Amir, M. Gupta, A. Gupta, M. Horisberger, and J. Stahn, "Formation of iron nitride thin films with al and ti additives," *Journal of Applied Physics*, vol. 111, no. 10, p. 103520, 2012. 34

[149] P. J. Kelly and R. D. Arnell, "Magnetron sputtering: a review of recent developments and applications," *Vacuum*, vol. 56, no. 3, pp. 159–172, 2000. 35

[150] J. D. Lamb and J. A. Woollam, "Dielectric properties of diamondlikecarbon prepared by rf plasma deposition," *Journal of applied physics*, vol. 57, no. 12, pp. 5420–5423, 1985. 35

[151] A. Mitra, O. Cespedes, Q. Ramasse, M. Ali, S. Marmion, M. Ward, R. Brydson, C. Kinane, J. Cooper, S. Langridge, *et al.*, "Interfacial origin of the magnetisation suppression of thin film yttrium iron garnet," *Scientific reports*, vol. 7, no. 1, p. 11774, 2017. xvii, 35, 61, 70, 71, 74, 85, 86

[152] M. Meng, S. Wu, L. Ren, W. Zhou, Y. Wang, G. Wang, and S. Li, "Extrinsic anomalous hall effect in epitaxial mn4n films," *Applied Physics Letters*, vol. 106, no. 3, p. 032407, 2015. 35

[153] H. Arend and J. Hulliger, *Crystal growth in science and technology*, vol. 210. Springer Science & Business Media, 2012. 35, 44

[154] H. Werner, M. Wohlers, D. Bublak, J. Blöcker, and R. Schlögl, "Interaction of molecular oxygen with solid c60," *Fullerenes, Nanotubes, and Carbon Nanostructures*, vol. 1, no. 4, pp. 457–474, 1993. 37

[155] Y.-H. Kim, I.-H. Lee, K.-J. Chang, and S. Lee, "Dynamics of fullerene coalescence," *Physical review letters*, vol. 90, no. 6, p. 065501, 2003. 37

[156] B. Bhushan, J. V. Coe Jr, and B. Gupta, "Method for coating fullerene materials for tribology," Sept. 24 1996. 37

[157] V. Piacente, G. Gigli, P. Scardala, A. Giustini, and D. Ferro, "Vapor pressure of c60 buckminsterfullerene," *The Journal of Physical Chemistry*, vol. 99, no. 38, pp. 14052–14057, 1995. 37

[158] G. Kroll, P. Benning, Y. Chen, T. Ohno, J. Weaver, L. Chibante, and R. Smalley, "Interaction of o2 with c60: photon-induced oxidation," *Chemical physics letters*, vol. 181, no. 2-3, pp. 112–116, 1991. 37

[159] M. M. Woolfson, *An introduction to X-ray crystallography.* Cambridge University Press, 1997. 39

[160] J. Als-Nielsen and D. McMorrow, *Elements of modern X-ray physics.* John Wiley & Sons, 2011. 39

[161] B. D. G. Steele, *Vortex Induced Magnetoresistance Oscillations in Superconducting Nanowires.* PhD thesis, University of Leeds, 2019. xiii, 41

[162] H. Wang, C. Du, P. C. Hammel, and F. Yang, "Strain-tunable magnetocrystalline anisotropy in epitaxial y 3 fe 5 o 12 thin films," *Physical Review B*, vol. 89, no. 13, p. 134404, 2014. 44

[163] M. Althammer, "Pure spin currents in magnetically ordered insulator/normal metal heterostructures," *Journal of Physics D: Applied Physics*, vol. 51, no. 31, p. 313001, 2018. 46

[164] J. Fontcuberta, H. B. Vasili, J. Gàzquez, and F. Casanova, "On the role of interfaces on spin transport in magnetic insulator/normal metal heterostructures," *Advanced Materials Interfaces*, vol. 6, no. 15, p. 1900475, 2019. 46

[165] A. Chtchelkanova, S. A. Wolf, and Y. Idzerda, *Magnetic interactions and spin transport.* Springer Science & Business Media, 2013. 47

[166] M. Tinkham, "Introduction to superconductivity ch. 3 mcgraw-hill," *Inc., New York*, 1996. 47

[167] C. Graham, "High-sensitivity magnetization measurements," *Journal of Materialsm Sciences and Technology*, no. 2, pp. 97–101, 2000. 47

[168] J. Clarke, "und ai braginski (ed.), the squid handbook: Vol. i fundamentals and technology of squids and squid systems," 2004. 47

[169] *Magnetic property measurement system SQUID VSM everCool option users manual. Quantum Design.* 2007. xiv, 48

[170] J. Kondo, "Resistance minimum in dilute magnetic alloys," *Progress of theoretical physics*, vol. 32, no. 1, pp. 37–49, 1964. 50

[171] J. Kondo, "Effect of ordinary scattering on exchange scattering from magnetic impurity in metals," *Physical Review*, vol. 169, no. 2, p. 437, 1968. 50

[172] D. Beutler and N. Giordano, "Localization and electron-electron interaction effects in thin bi wires and films," *Physical Review B*, vol. 38, no. 1, p. 8, 1988. 50, 102

[173] H. Hoffmann and J. Vancea, "Critical assessment of thickness-dependent conductivity of thin metal films," *Thin Solid Films*, vol. 85, no. 2, pp. 147–167, 1981. 51

[174] C. Tellier, A. Tosser, and C. Boutrit, "The mayadas-shatzkes conduction model treated as a fuchs-sondheimer model," *Thin Solid Films*, vol. 44, no. 2, pp. 201–208. 51

[175] P. Wissmann and H.-U. Finzel, *Electrical resistivity of thin metal films*, vol. 223. Springer Science & Business Media, 2007. 51

[176] A. B. Pippard, *Magnetoresistance in metals*, vol. 2. Cambridge university press, 1989. 54, 57

[177] E. Fawcett, "Magnetoresistance of transition metals in the high-field limit," *Physical Review Letters*, vol. 7, no. 10, p. 370, 1961. 54

[178] S. S.-L. Zhang and S. Zhang, "Magnon mediated electric current drag across a ferromagnetic insulator layer," *Physical review letters*, vol. 109, no. 9, p. 096603, 2012. 54

[179] S. S.-L. Zhang and S. Zhang, "Spin convertance at magnetic interfaces," *Physical Review B*, vol. 86, no. 21, p. 214424, 2012. 54

[180] H. Wu, C. Wan, X. Zhang, Z. Yuan, Q. Zhang, J. Qin, H. Wei, X. Han, and S. Zhang, "Observation of magnon-mediated electric current drag at room temperature," *Physical Review B*, vol. 93, no. 6, p. 060403, 2016. 54

[181] H. Hoffmann, F. Hofmann, and W. Schoepe, "Magnetoresistance and non-ohmic conductivity of thin platinum films at low temperatures," *Physical Review B*, vol. 25, no. 8, p. 5563, 1982. 54, 101

[182] Y. Niimi, D. Wei, H. Idzuchi, T. Wakamura, T. Kato, and Y. Otani, "Experimental verification of comparability between spin-orbit and spin-diffusion lengths," *Physical review letters*, vol. 110, no. 1, p. 016805, 2013. 54

[183] J. Ryu, M. Kohda, and J. Nitta, "Observation of the dyakonov-perelspin relaxation in single-crystalline pt thin films," *Physical review letters*, vol. 116, no. 25, p. 256802, 2016. 54

[184] L. Baldrati, A. Ross, T. Niizeki, C. Schneider, R. Ramos, J. Cramer, O. Gomonay, M. Filianina, T. Savchenko, D. Heinze, *et al.*, "Full angular dependence of the spin hall and ordinary magnetoresistance in epitaxial antiferromagnetic nio (001)/pt thin films," *Physical Review B*, vol. 98, no. 2, p. 024422, 2018. 58

[185] M. Isasa, S. Vélez, E. Sagasta, A. Bedoya-Pinto, N. Dix, F. Sánchez, L. E. Hueso, J. Fontcuberta, and F. Casanova, "Spin hall magnetoresistance as a probe for surface magnetization in pt/co fe 2 o 4 bilayers," *Physical Review Applied*, vol. 6, no. 3, p. 034007, 2016. 58

[186] J. Bass and W. P. Pratt, "Spin-diffusion lengths in metals and alloys, and spin-flipping at metal/metal interfaces: an experimentalists critical review," *Journal of Physics: Condensed Matter*, vol. 19, no. 18, p. 183201, 2007. 60

[187] L. Liu, R. Buhrman, and D. Ralph, "Review and analysis of measurements of the spin hall effect in platinum," *arXiv preprint arXiv:1111.3702*, 2012. 60

[188] X. Tao, Q. Liu, B. Miao, R. Yu, Z. Feng, L. Sun, B. You, J. Du, K. Chen, S. Zhang, *et al.*, "Self-consistent determination of spin hall angle and spin diffusion length in pt and pd: The role of the interface spin loss," *Science advances*, vol. 4, no. 6, p. eaat1670, 2018. 60

[189] H. Corte-León, V. Nabaei, A. Manzin, J. Fletcher, P. Krzysteczko, H. W. Schumacher, and O. Kazakova, "Anisotropic magnetoresistance state space of permalloy nanowires with domain wall pinning geometry," *Scientific Reports*, vol. 4, no. 1, pp. 1–10, 2014. 66

[190] W. Gil, D. Görlitz, M. Horisberger, and J. Kötzler, "Magnetoresistance anisotropy of polycrystalline cobalt films: Geometrical-size and domain effects," *Physical Review B*, vol. 72, no. 13, p. 134401, 2005. 66

[191] P. Wang, H. Zhao, S. Liu, Y. Chin, H. Lin, B. Zhang, Z. Yuan, S. Jiang, H. Ding, J. Du, *et al.*, "Reduced interfacial magnetic moment of y3fe5o12 by capping pt," *Applied Physics Letters*, vol. 113, no. 18, p. 182402, 2018. 74

[192] X.-P. Zhang, F. S. Bergeret, and V. N. Golovach, "Theory of spin hall magnetoresistance from a microscopic perspective," *Nano letters*, vol. 19, no. 9, pp. 6330–6337, 2019. 76

[193] Y. Tserkovnyak, A. Brataas, and G. E. Bauer, "Spin pumping and magnetization dynamics in metallic multilayers," *Physical Review B*, vol. 66, no. 22, p. 224403, 2002. 78

[194] K. Meng, J. Xiao, Y. Wu, J. Miao, X. Xu, J. Zhao, and Y. Jiang, "Hybrid magnetoresistance in pt-based multilayers: Effect originated from strong interfacial spin-orbit coupling," *Scientific reports*, vol. 6, no. 1, pp. 1–9, 2016. 79

[195] T. Kim, I. H. Cha, Y. J. Kim, G. W. Kim, A. Stashkevich, Y. Roussigné, M. Belmeguenai, S. M. Chérif, A. S. Samardak, and Y. K. Kim, "Ruderman–kittel–kasuya–yosida-type interfacial dzyaloshinskii–moriya interaction in heavy metal/ferromagnet heterostructures," *Nature communications*, vol. 12, no. 1, pp. 1–10, 2021. 88

[196] N. O. Nnolim, T. A. Tyson, and L. Axe, "Theory of the structural phases of group 5b–6b metals and their transport properties," *Journal of applied physics*, vol. 93, no. 8, pp. 4543–4560, 2003. 91

[197] J. Zhang, Y. Huai, L. Chen, and J. Zhang, "Formation of low resistivity alpha ta by ion beam sputtering," *Journal of Vacuum Science & Technology B: Microelectronics and Nanometer Structures Processing, Measurement, and Phenomena*, vol. 21, no. 1, pp. 237–240, 2003. 91

[198] K. Valleti, A. Subrahmanyam, and S. V. Joshi, "Growth of nano crystalline near α phase tantalum thin films at room temperature using cylindrical magnetron cathode," *Surface and Coatings Technology*, vol. 202, no. 14, pp. 3325–3331, 2008. 91

[199] L. Feinstein and D. Gerstenberg, "Structure and electrical properties of ta films sputtered in ar o2," *Thin Solid Films*, vol. 10, no. 1, pp. 79–89, 1972. 91

[200] F. Sajovec, P. Meuffels, and T. Schober, "Structural and electrical properties of ion beam sputter deposited tantalum films," *Thin Solid Films*, vol. 219, no. 1-2, pp. 206–209, 1992. 91

[201] J. Narayan, V. Bhosle, A. Tiwari, A. Gupta, P. Kumar, and R. Wu, "Methods for processing tantalum films of controlled microstructures and properties," *Journal of Vacuum Science & Technology A: Vacuum, Surfaces, and Films*, vol. 24, no. 5, pp. 1948–1954, 2006. 91

[202] M. Grosser and U. Schmid, "The impact of sputter conditions on the microstructure and on the resistivity of tantalum thin films," *Thin Solid Films*, vol. 517, no. 16, pp. 4493–4496, 2009. 92, 105, 123

[203] M. Sanquer, R. Tourbot, and B. Boucher, "Correlation between high-and low-temperature conductivities in high resistive disordered metals," *EPL (Europhysics Letters)*, vol. 7, no. 7, p. 635, 1988. 92

[204] P. W. Anderson, "Absence of diffusion in certain random lattices," *Physical review*, vol. 109, no. 5, p. 1492, 1958. 92

[205] S. Ciuchi, D. Di Sante, V. Dobrosavljević, and S. Fratini, "The origin of mooij correlations in disordered metals," *npj Quantum Materials*, vol. 3, no. 1, pp. 1–6, 2018. 92

[206] G. W. Anderson, Y. Huai, and M. Pakala, "Spin-valve thermal stability: The effect of different antiferromagnets," *Journal of applied physics*, vol. 87, no. 9, pp. 5726–5728, 2000. 107

[207] J. Nozieres, S. Jaren, Y. Zhang, K. Pentek, A. Zeltser, P. Wills, and V. Speriosu, "Correlation between lifetime and blocking temperature distribution in spin-valve structures," *Journal of Applied Physics*, vol. 87, no. 9, pp. 6609–6611, 2000. 107

[208] J. Nozières, S. Jaren, Y. Zhang, A. Zeltser, K. Pentek, and V. Speriosu, "Blocking temperature distribution and long-term stability of spin-valve structures with mn-based antiferromagnets," *Journal of applied physics*, vol. 87, no. 8, pp. 3920–3925, 2000. 107

[209] C.-X. Ji, P. F. Ladwig, R. D. Ott, Y. Yang, J. J. Yang, Y. A. Chang, E. S. Linville, J. Gao, and B. B. Pant, "An investigation of phase transformation behavior in sputter-deposited ptmn thin films," *JOM*, vol. 58, no. 6, pp. 50–54, 2006. 107

[210] Y. Ou, S. Shi, D. Ralph, and R. Buhrman, "Strong spin hall effect in the antiferromagnet ptmn," *Physical Review B*, vol. 93, no. 22, p. 220405, 2016. 107

[211] W. Zhang, M. B. Jungfleisch, W. Jiang, J. E. Pearson, A. Hoffmann, F. Freimuth, and Y. Mokrousov, "Spin hall effects in metallic antiferromagnets," *Physical review letters*, vol. 113, no. 19, p. 196602, 2014. 108, 117

[212] G. Bergmann, "Consistent temperature and field dependence in weak localization," *Physical Review B*, vol. 28, no. 2, p. 515, 1983. 109

[213] F. Al MaMari, M. Rogers, S. Alghamdi, T. Moorsom, S. Lee, T. Prokscha, H. Luetkens, M. Valvidares, G. Teobaldi, M. Flokstra, *et al.*, "Emergent magnetism at transition-metal–nanocarbon interfaces," *Proceedings of the National Academy of Sciences*, vol. 114, no. 22, pp. 5583–5588, 2017. 124

[214] T. Moorsom, M. Rogers, I. Scivetti, S. Bandaru, G. Teobaldi, M. Valvidares, M. Flokstra, S. Lee, R. Stewart, T. Prokscha, *et al.*, "Reversible spin storage in metal oxidefullerene heterojunctions," *Science advances*, vol. 6, no. 12, p. eaax1085, 2020. xxiii, 124, 125

[215] M. A. Laguna-Marco, D. Haskel, N. Souza-Neto, J. Lang, V. Krishna-murthy, S. Chikara, G. Cao, and M. van Veenendaal, "Orbital magnetism and spin-orbit effects in the electronic structure of bairo 3," *Physical review letters*, vol. 105, no. 21, p. 216407, 2010. xxiii, 125

[numbers]natbib